Uncovering new thermal and elastic properties of nanostructured materials using coherent EUV light

by

Jorge Nicolás Hernández Charpak

B.S., Universidad de los Andes, 2010

B.E., Universidad de los Andes, 2011

M.S., University of Colorado Boulder, 2014

A thesis submitted to the

Faculty of the Graduate School of the

University of Colorado in partial fulfillment

of the requirements for the degree of

Doctor of Philosophy

Department of Physics

2017

This thesis entitled:
Uncovering new thermal and elastic properties of nanostructured materials using coherent EUV light
written by Jorge Nicolás Hernández Charpak
has been approved for the Department of Physics

Prof. Margaret M. Murnane

Prof. Henry C. Kapteyn

Date

The final copy of this thesis has been examined by the signatories, and we find that both the content and the form meet acceptable presentation standards of scholarly work in the above mentioned discipline.

Hernández Charpak, Jorge Nicolás (Ph.D., Physics)

Uncovering new thermal and elastic properties of nanostructured materials using coherent EUV light

Thesis directed by Prof. Margaret M. Murnane and Prof. Henry C. Kapteyn

Advances in nanofabrication have pushed the characteristic dimensions of nanosystems well below $100nm$, where physical properties are often significantly different from their bulk counterparts, and accurate models are lacking. Critical technologies such as thermoelectrics for energy harvesting, nanoparticle-mediated thermal therapy, nano-enhanced photovoltaics, and efficient thermal management in integrated circuits depend on our increased understanding of the nanoscale. However, traditional microscopic characterization tools face fundamental limits at the nanoscale. Theoretical efforts to build a fundamental picture of nanoscale thermal dynamics lack experimental validation and still struggle to account for newly reported behaviors. Moreover, precise characterization of the elastic behavior of nanostructured systems is needed for understanding the unique physics that become apparent in small-scale systems, such as thickness-dependent or fabrication-dependent elastic properties. In essence, our ability to fabricate nanosystems has outstripped our ability to understand and characterize them.

In my PhD thesis, I present the development and refinement of coherent extreme ultraviolet (EUV) nanometrology, a novel tool used to probe material properties at the intrinsic time- and length-scales of nanoscale dynamics. By extending ultrafast photoacoustic and thermal metrology techniques to very short probing wavelengths using tabletop coherent EUV beams from high-harmonic upconversion (HHG) of femtosecond lasers, coherent EUV nanometrology allows for a new window into nanoscale physics, previously unavailable with traditional techniques. Using this technique, I was able to probe both thermal and acoustic dynamics in nanostructured systems with characteristic dimensions below $50nm$ with high temporal (sub-ps) and spatial ($< 10pm$ vertical)

resolution, including the smallest heat sources probed ($20nm$) and thinnest film ($10.9nm$) fully mechanically characterized to date.

By probing nanoscale thermal transport (i.e. cooling) of periodic hot nanostructures down to $20nm$ in characteristic dimension in both 1D (nanolines) and 2D (nanocubes) geometries, I uncovered a new surprising regime of nanoscale thermal transport called the "collectively-diffusive regime. In this regime, nanoscale hot spots cool faster when placed closer together than when farther apart. This is a consequence of the interplay between both the size and spacing of the nanoscale heat sources with the phonon spectrum of a material. This makes our technique one of the only experimental routes to directly probe the dynamics of phonons in complex materials, which is critical to both technological applications and fundamental condensed matter physics. I developed a proof of concept model and used it to extract the first experimental differential conductivity phonon mean free path (MFP) spectra for silicon and sapphire, which compare well with first-principles calculations. However, a complete picture of the physics is still elusive. Thus, I developed a computational solver for the phonon Boltzmann transport equation in realistic experimental geometries. Using this approach, I successfully found confirmation of the influence of the period in thermal transport from periodic heat sources: a smaller periodicity can enhance the heat dissipation efficiency. This result is qualitatively consistent with the results of the "collectively-diffusive regime", but more work is needed for a full theoretical quantitative picture of the experimental results.

In other work, I used coherent EUV nanometrology to simultaneously measure, in a non-contact and non-destructive way, Young's modulus and, for the first time, Poisson's ratio of ultra-thin films. I successfully extracted the full elastic tensor of the thinnest films to date ($10.9nm$). Moreover, by using our technique on a series of low-k dielectric sub-$100nm$ SiC:H films, I uncovered an unexpected transition from compressible to non-compressible behavior. This new behavior is observed for materials whose network connectivity had been modified through hydrogenation (that breaks bonds in order to decrease the dielectric constant of these materials). This finding demonstrates that coherent EUV nanometrology provides a valuable, quantitative new tool for

measuring nanomaterial properties with dimensions an order of magnitude smaller than what was possible with traditional techniques.

I also present here some of my written work on science and technology policy studies. I present my thoughts on the Kuhnian model of scientific revolutions and how it relates to my own experience. I also discuss two case studies to illustrate the critical importance of defining appropriate metrics to measure science policies by looking at the design of metrics for the American Reinvestment and Recovery Act, and the results of exploring a novel modality of funding for large complex scientific and technological challenges: the US Department of Energy Innovation HUBs.

Coherent EUV nanometrology presents an exciting new window into nanoscale phonon dynamics, making measurements of the phonon MFP spectrum of materials and the full elastic tensor of ultra-thin films possible. It is now a robust technique that is already having impact in many areas of materials science and condensed matter physics, and it will continue to do so in the future.

Dedication

To my grandparents, innovators and adventurers in all fields.

To my parents, for inspiring us to build a better world.

To Dani, for everything.

A mis abuelos y abuelas, innovadores y aventureros en todos los campos.

A mis padres, por inspiranos a construir un mundo mejor.

A Dani, por todo.

A mes granparents, innovateurs and aventuriers dans tout les champs.

A mes parents, qui nous inspirent á construir un meilleur monde.

A Dani, pour tout.

Acknowledgements

During the past 6 years, many people have supported me through the adventure of the PhD. I have many to thank for their support, kindness, work, trust, love and friendship, and this small paragraph can't hold them all. I want to mention a few people to whom I am extremelly grateful. Thank you to Margaret and Henry for their support and brilliant guidance. To the KM group in general for being an incredible familly of bright, happy, and creative people. Thank you to my committee members and collaborators for providing with invaluable ideas, samples and discussions. No good science is done alone. Kathy and Damiano, thank you for teaching me everything I know with incredible patience. I will always remember our time working together fondly. Josh, Travis, and Begoña, thank you for your help crossing the finishing line. You are an incredible team to work with. I know that the project is in the best of hands, and you will take it to the level it deserves. Thank you to the JILA and Physics Department staff for making this an incredible place to work. To My parents, thank you for your never ending support, and for making sure I never ran out of chocolate. Thanks to Sergio and Yvan for always being there even when we are in three different continents. Dani, thank you for your support, patience, soups, runs and hikes. And to my friends Pablo, Duque, Tigre, Amanda, Natalia, Jack, Andrew, Oscar, Tyler, Sandy, Devin, Julian, Shino, Andrea, Francesca, thank you for being part of my work one way or another and for always being there in the highs and the lows of this adventure.

Contents

Chapter

Tables

Table

Figures

Figure

Chapter 1

Introduction

Every year witnesses the release of a new piece of technology that is not only faster, but also smaller, lighter, and stronger. Computers revolutionized our word, going from rare pieces of equipment that fill an entire building in the 1960s to more than three billion units worldwide only 50 years later. Smartphones achieved the same number of units in less than 20 years. These technological advances were largely possible due to the development of nanoscale fabrication techniques. From novel medical drugs and hard drives, to the Internet and smartphones, our increased understanding and harvesting of the micro- and nano-scale has had an enormous impact on technology and society. This drive for faster and smaller technology has also created new opportunities to increase our fundamental understanding of the "very small". However, both technology and our fundamental understanding suffer from a lack of measurement techniques and comprehensive theories. As an example of this combination of impact and challenge in nanotechnology, consider microelectronics.

Microelectronics has been at the center of the technological revolution of the last 50 years. There are today roughly only ten times fewer transistors (the building blocks of modern electronics) in the world as there are stars in our observable universe (which are estimated at $\approx 10^{23}$) [1]. Since the 1970s, the microelectronics industry has been following a tight roadmap to shrink the size of transistors by 30% every two years, following the self-imposed "Moore's law". This has reduced the size of transistors from mm to $\approx 10nm$ today. As the size of transistors has gotten smaller, their density on a chip has increased exponentially, as illustrated in Fig. 1.1. This increase in

density has increased the power of computers, and decreased the price of electronics in general, but it has also made the issue of heat management ever more problematic. Not only is more heat generated per unit area, but the models used to describe heat dissipation at the macroscale break down at these extremely small scales, making design more difficult. This caused the "thermal load" plateau in clock speeds that we have seen since the early 2000s, as shown in Fig. 1.1 [2]. Although that did not stop the pursuit of Moore's law for transitor size, it was telling of a greater limitation that we are facing today: the miniaturization of transistors is reaching its limit. It is no longer physically possible to fabricate reliable transistors below the $5nm$ node without running into quantum mechanical tunneling of electrons, which makes the transistors useless. It is still possible to improve microelectronics through innovations in architecture, but this requires a better understanding of nanometer scale phenomena.

With the miniaturization of electronics came an impressive development of nanoscale fabrication technology. Today, films can be made with atomic thickness precision, and structures can be fabricated with sub-ten nanometer characteristic dimensions with high repeatability and reliability [3]. However, with too many atoms for quantum mechanics tools to be effective, and too few for statistical mechanics' tools to succeed, nanoscale dynamics have proven to be a challenge both to characterization tools and macroscopic models. This presents an opportunity to increase our understanding of few- and many-body condensed matter physics. Studies in nanoscale dynamics have already revealed unexpected and rich phenomena and novel materials, such as transport in low-dimensional materials, photonic and phononic meta-materials, enhanced solar cells, near-field enhancement of electric fields for ultra-high resolution microscopy, and many others. The field also still offers many open questions and challenges, from topological insulators, to high temperature superconductors, to non-diffusive thermal dynamics and non-bulk properties of nanostructured systems. In addition, the very small is also the very fast, as illustrated in Fig. 1.2. This is both a challenge and an opportunity, as studying nanoscale dynamics is an opportunity to study ultrafast phenomena.

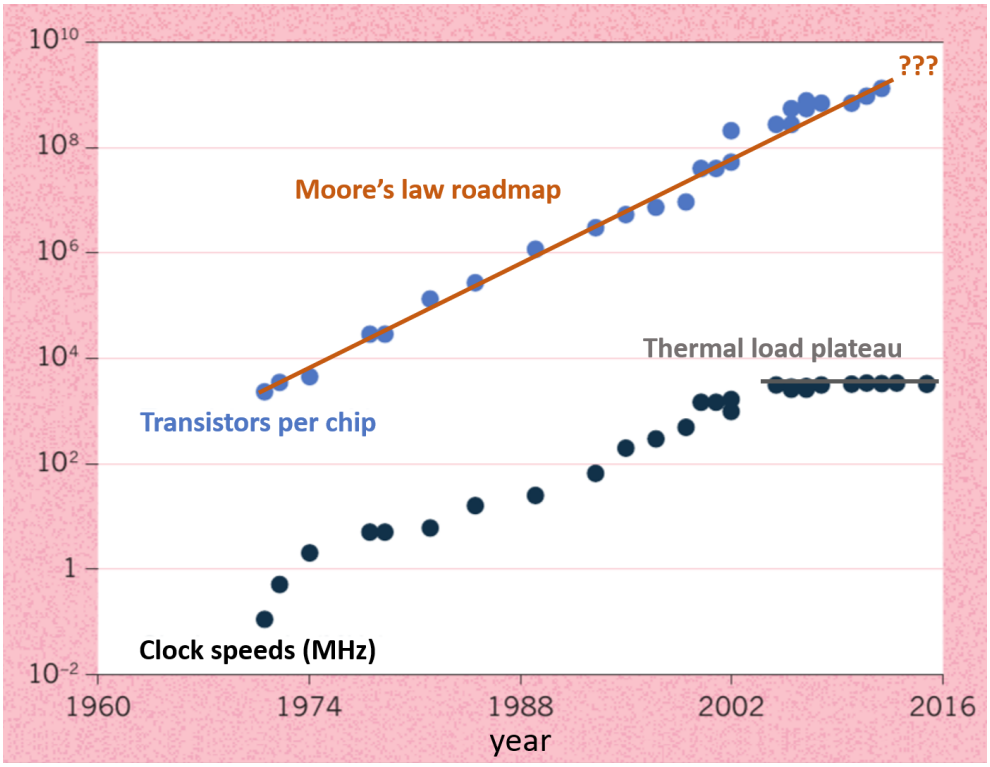

Figure 1.1: **Number of transistors on a chip and clock speeds in CPUs since the 1970s** The number of transistors per chip (blue data points) have follow the Moore's law roadmap (orange line) since the 1970s. However, the roadmap is unclear as we approach the 5nm node close to 2020. The clock speed of chips (black data points) have seen an exponential increase in the 1970s that stopped in the early 2000s, where the thermal load of the chips became a significant issue, creating a thermal load plateau in the clock speeds (dark line) | Figure adapted from [2]

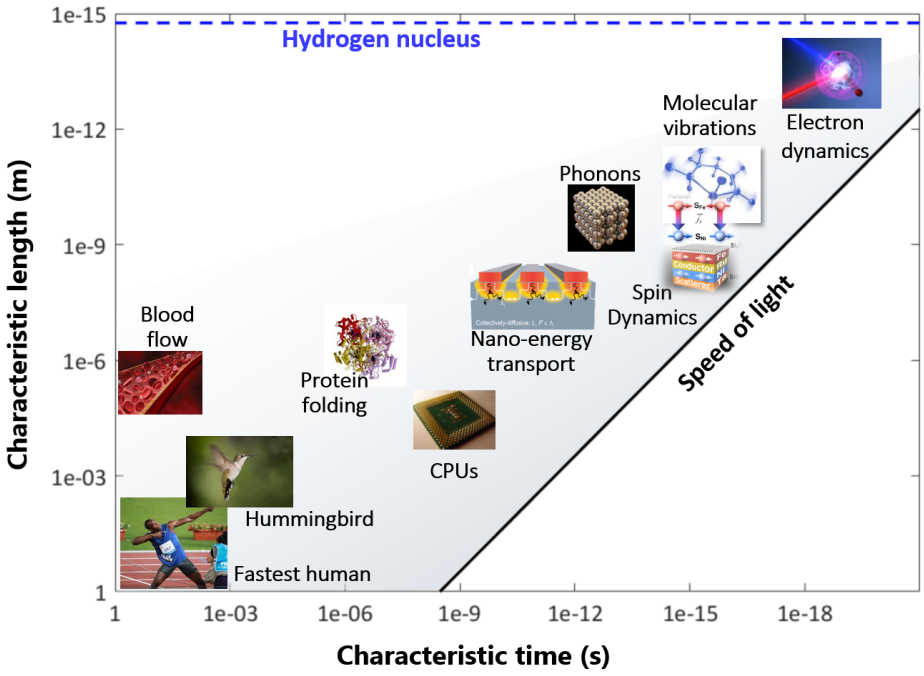

Figure 1.2: **Relationship between characteristic time- and length-scales of physical phenomena** Illustration of the relationship between physical phenomena length- and time-scales. Some examples are shown here to show how small scale phenomena have decreasing characteristic time-scales. Experimental tools that aim to study the nanoscale have then to be capable of at least picosecond temporal resolution. This parameter space is bounded by the speed of light (solid black line).The size of a hydrogen nucleus (dashed blue line) is shown as a frame of reference. | images from [4, 5]

Traditional models and metrology technologies that can be used for macro- and micro-scale systems face many challenges and sometimes fundamental limits when trying to describe nanoscale systems [3]. A more comprehensive and fundamental understanding of the nanoscale is critically needed today, as it promises many key technological applications besides nanoelectronics, such as enhanced thermoelectric materials that could help humanity be more efficient with energy generation, develop nano-mediated medical therapies that can precisely target treatment areas, or engineer entirely new material properties that could revolutionize our society. Moreover, even as today's nano-fabrication capabilities have reached incredible levels of precision and robustness, our measurement capabilities have not. This creates an urgent need for new metrology tools that are able to resolve the dynamics of often complex nanostructured systems.

This is the motivation behind a large portion of the work done by the Kapteyn-Murnane research group, as well as my own. My doctoral work focused on the development and refinement of a novel metrology technique that allows the direct measurement of nanoscale lattice dynamics at their intrinsic length- and time-scales. Lattice dynamics cover many fields of interest, in particular thermal transport at the nanoscale, and elastic properties of nanostructured systems. We developed coherent EUV nanometrology as one of the few experimental techniques that is able to directly probe lattice dynamics at the intrinsic time- and length-scales of nanoscale dynamics. At the nanoscale, the length scale of nanostructured systems is comparable to the length scale of phonons (quantas of lattice displacement), bringing forth a new set of physical phenomena that are still not fully described by current theoretical models. My work hopes to provide valuable experimental results to guide theory and further our fundamental understanding of the microscopic components of lattice dynamics.

In my thesis, I developed new ways to probe and model material properties at the nanoscale by extending photoacoustic and thermal metrology to very short wavelengths using tabletop coherent extreme ultraviolet (EUV) beams from high-harmonic up conversion (HHG) of femtosecond lasers [1-3]. Using this technique, I was able to probe both thermal and acoustic dynamics in

nanostructured systems with characteristic dimensions below $50nm$ with high temporal (sub-ps) and spatial ($< 10pm$ vertical) resolution.

Chapter 2 presents the main experimental and computational principles and tools in this measurement technique. It starts by discussing the use of high harmonic generation to generate coherent short pulses of extreme ultraviolet light (EUV). It then describes how these light sources' short wavelengths, coherence and short pulse durations enabled me to probe surface dynamics with sub-atomic spatial resolution and sub-picosecond temporal resolution. Finally, it shows how I use advanced computational modeling to further the precision of the experimental results by providing clear frameworks of interpretation and a pathway to comparison with theoretical calculations.

Chapter 3 focuses on using coherent EUV nanometrology to probe nanoscale thermal transport and how it deviates from macroscopic models in surprising ways. It presents the results of probing nanoscale thermal transport (i.e. cooling) of hot nanostructures down to $20nm$ in characteristic dimension in both 1D (nanolines) and 2D (nanodots) geometries. It further reports the uncovering of a new and surprising regime of nanoscale thermal transport: the "collectively-diffusive" regime. In this regime, nanoscale hot spots cool faster when placed closer together than the average phonon mean free path (MFP) in the substrate [5]. The chapter also presents the theoretical framework I developed to describe the observed dynamics as well as its predictions. These predictions were further confirmed by more measurements on 1D confined heat sources where the distance between nanolines was changed, without changing their characteristic dimension [6]. The model and technique I used successfully measures and describes dynamics from the smallest heat sources to date, as well as enables the first distance-dependent study of nanoscale thermal transport. This promises to be one of the only experimental routes to directly probe the dynamics of phonon dynamics in complex materials, critical to new applications [5]. The chapter ends by presenting the first experimentally extracted differential MFP spectrum of silicon and sapphire, paving the way to phonon lifetime spectroscopy.

However, a complete picture of the physics is still elusive. Chapter 4 focuses on nanoscale thermal transport from a computational and theoretical perspective. This chapter also presents

models that compare our experimental results to the phonon Boltzmann transport equation, solved in our experimental geometries.

Chapter 5 presents the results of using coherent EUV nanometrology to extract the complete elastic properties of ultra-thin films, including the characterization of the thinnest film to date [7, 8]. Using this technique, I also uncovered an unexpected transition from compressible to non-compressible behavior for low-k dielectric sub-100nm SiC:H films. This new behavior is observed for materials whose molecular structure had been modified through hydrogenation [7]. This finding demonstrates that my approach provides a new quantitative window into nanomaterials, and is relevant for informing current and future work in the semiconductor industry.

Chapter 6 presents work that I have done regarding the science and technology policy implications of my work as a researcher at the KM group and as an active member of the wider national scientific community. I present a simple but powerful model for scientific "progress" that captures the non-linearity and the social aspects of scientific activity. I also present two case studies to demonstrate the importance of defining appropriate metrics when measuring policy outcome, and to argue that novel funding mechanisms might be needed when addressing research problems.

Chapter 7 presents the plans for future work on several projects, as well as the conclusions of this dissertation.

Chapter 2

Coherent EUV nanometrology: background and setup

My doctoral work as part of Kapteyn-Murnane research group has been dedicated to build an effective, robust and precise tool to measure ultrafast dynamics of nanostructured systems, in particular nanoscale lattice dynamics. In doing so, a lot of my work, which builds on the work of previous graduate students in the group, has been dedicated to build and refine what we now call coherent EUV nanometrology, which is today a fully functional and powerful new method to gain access to deep nanoscale phonon dynamics in nanostructured systems.

In this chapter, I present the characteristics of coherent EUV nanometrology. This technique allows great flexibility in studying both elastic and thermal nanoscale dynamics in a wide variety of nanostructured systems, which I will discuss in later chapters. The chapter starts with a general introduction to pump-probe spectroscopy measurements. It then describes the experimental setup, starting with an introduction to high harmonic generation (HHG) of coherent extreme ultraviolet (EUV) light and continuing with excitation schemes, sample geometries and data acquisition. It then describes the consolidation of data collected and the data flow in general, and finishes with a description of the principles behind the modeling tools that are used to interpret the extracted data, including our finite element modeling procedures that are used for both thermal and acoustic studies.

2.1 Ultrafast pump-probe spectroscopy

The universe is inherently dynamic, i.e., it changes with time. Therefore, a unit of reference is needed in order to be able to perceive these dynamic changes. Humans probably started measuring time with natural occurring periodic phenomena using the sun, the moon and the stars as time-keepers. Day, night, months and years became the first units of time, common to cultures all around the world. Further along the way, a smaller unit of time was needed to describe daily life, and so humans began to divide day and night into segments, that became hours and minutes using a solar clocks, and water and sand clocks. The usage of seconds and a more reliable time-keeping techniques came with the invention of mechanical clocks. But time-keeping also is a tool to describe the natural world that surrounds us, such as describing the wing-flapping of a hummingbird or the speed of sound in materials. However, precise time keeping devices are not the only element needed for this. How useful is a stopwatch that can measure down to a microsecond if it is operated by a human that can only perceive dynamics down to tens of milliseconds?

There are two main components required to capturing a transient phenomena: the frame capture time (also known as the detector's temporal integration time) τ_f and the frames per second fps. τ_f corresponds to the detector resolution, how short of an event it can perceive, similar to the exposure time for modern cameras. fps is only relevant when a time-dependent picture can be taken, and corresponds to how sparse frames are in a given second. A transient phenomena will have a characteristic time-frame τ_p, such as attoseconds for electron dynamics, milliseconds for a hummingbird's wings, or months for me writing this thesis. If $\tau_f > \tau_p$ the detection will fail and the result will be a "blurry" measurement, such as taking the picture of a hummingbird's moving wings with a slow camera, the detector resolution is insufficient to distinguish the wings at two points in space, because it is too slow. Before the invention of photography, all the detection of transient phenomena was done with the human eye, which has (for an untrained average eye) $\tau_f \approx 25ms$ and $fps \approx 50fps$ [9]. With the advent of photography, this would change.

First photographic techniques in the 19th century had very long exposure times, and so long τ_f, and it allowed for the recording of still images: sceneries, cadavers and very still people. Although an amazing technology, it didn't allow for time measurements that could beat the human eye. One of the first breakthroughs in that respect happened in 1878, which resulted in the invention of fast photographic technology: the mechanical shutter. In 1878 many people were (still) debating whether or not all four hooves of a horse, when at full speed, would at some point be fully off the ground, or if there was always contact with the ground. This was a particularly difficult question to answer with the human eye. That is why Leland Stanford (at that point the former governor of California) charged the photographer Edweard Muybridge with resolving this question. Muybridge figured out that if he only exposed a very sensitive camera for a very short amount of time, it would only capture movement happening at that time scale. He built several mechanical shutters that would open and close at fast speed and aligned 12 cameras on a track to capture what is known today as "the horse in motion" series of pictures, illustrated in Fig. 2.1. This work represents the first, to my knowledge, ultrafast dynamic measurement as it has a τ_f shorter than the one of the human eye.

The mechanical shutter allowed for τ_f to be much smaller than before. Nowadays shutter exposure times can be as small as a microsecond or even a few hundred picoseconds! The main limitation is, however, the fps, limited by how many times can the shutter repeat its opening and closing operation per second, this is why Muybridge had to use 12 different cameras. There can also be a limitation in the amount of light that gets to the detector, as it might not be sufficient if the opening time is very short in low-light conditions. Finally, mechanical shutters τ_f can't seem to be decreased below a few hundred picoseconds, even today. In order to get a really high temporal resolution in a dynamic measurement and high fps another technique needed to be perfected: the stroboscopic measurement.

Perhaps the most famous examples of stroboscopic measurement development come from Doctor Harold Edgerton's work at MIT in the 1930s. The usage of flash photography to provide light in low-light level conditions became a common practice since around the mid 1800s. A

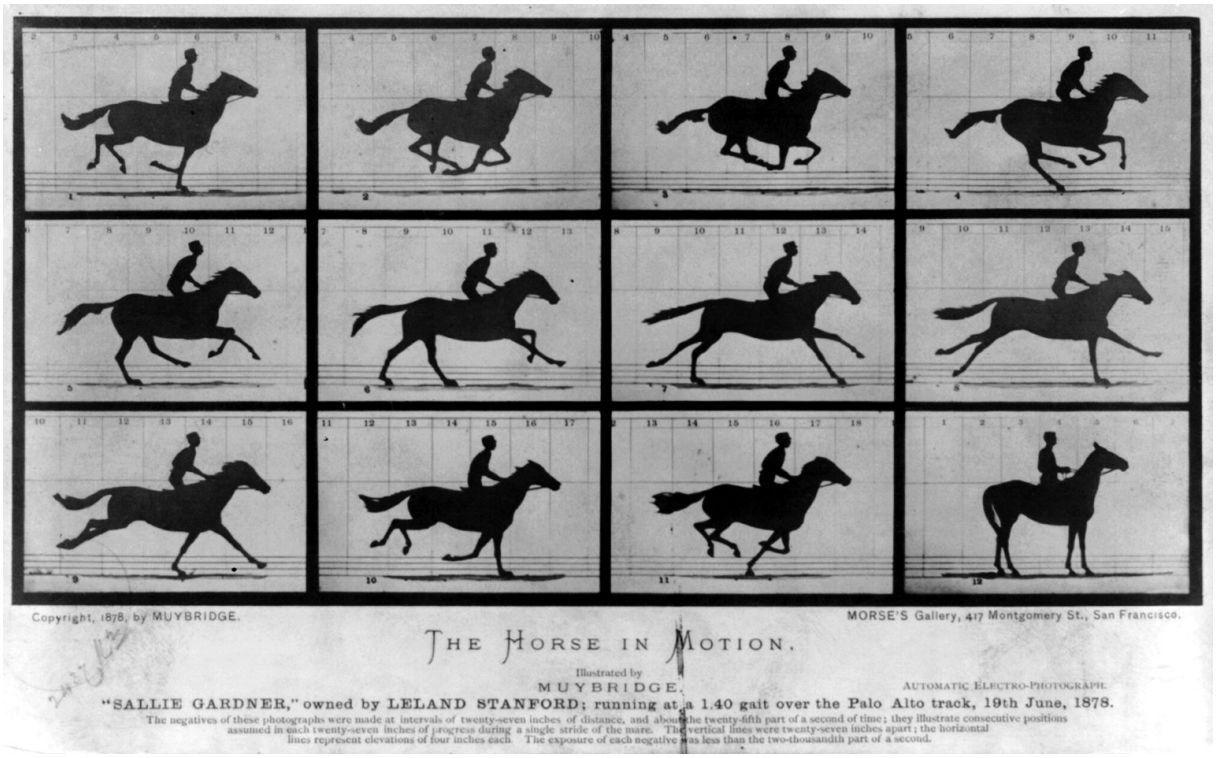

Figure 2.1: **The Horse in Motion, by Edweard Muybridge 1878**. With this series of pictures, Edweard Muybrigde provided the proof of a long lasting debate: all four hooves of a horse do loose contact with the ground when at gallop. This represents the start of ultrafast measurements that capture physical phenomena that happen faster than the human eye can resolve, started the development of mechanical shutter and is a precursor to films.| Photography from the Library of Congress Prints and Photographs Division.

good flash would be synchronized with the opening period of a shutter in order to work well. As technology evolved from chemical flash to electronic flash, the duration of flash's light pulses became shorter. Doctor Edgerton realized that pulses of light can be made shorter than shutter opening times, and had repetition rates often faster than mechanical shutters. Even though stroboscopes already existed (lamps that would flash short pulses of light at a constant frequency), he was the first to use the technology to capture on film very short snapshots of continuous movements. The main principle behind his work is that the short integration time τ_f is no longer provided by a mechanical shutter, but by a light pulse. The detector can expose in a dark room for a long time, but won't capture anything since there is no light. Therefore, by confining the light duration to a very short time, a detector in a dark room will only capture the light that came from that pulse, effectively reducing τ_f to the light pulse duration, and fps to set by the repetition rates of electronic flashes. This technology allowed him to capture, among many interesting things, the first "will it blend?" video, as shown in Fig. 2.2b and a series of tantalizing pictures of bullets going through various fruits, like the banana shown in Fig. 2.2a. The concept of using light as the shutter is key for ultrafast science, as pulses of light today can be generated to be as short as a few attoseconds ($10^{-18}s$) [10], allowing for τ_f to reach times smaller than the time it takes for an electron to go around an atomic nucleus ($\approx 150 \times 10^{-18}s$) [11].

Using light as the shutter to capture short dynamics in an instant is a key step, but being able to capture many of those frames at high fps is paramount to capture ultrafast dynamics. Sadly, the repetition rates for producing short pulses of light does not usually exceed hundreds of GHz, which means that even if τ_f is on the order of attoseconds, it would only be possible to capture frames every $10ps$ apart, a four orders of magnitude difference.

The problem of "low" fps presents an insurmountable wall when studying a phenomena that only happen once, but it can definitely be solved to study dynamics of repeatable phenomena. By manipulating the arrival time of the measuring flash of light to the repeatable phenomena, one can capture different snapshots of that phenomena. The effective fps of the reconstructed movie (resulting from stitching the captured frames together in order) is only limited by the precision of

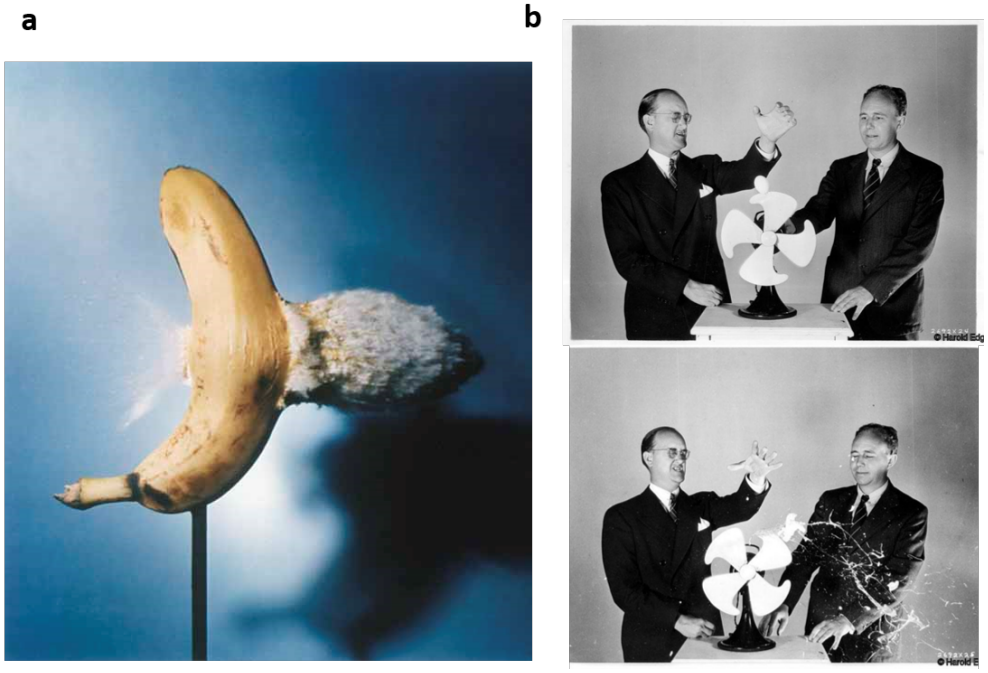

Figure 2.2: **Harold Edgerton's ultrafast snapshots** Using short pulses of light to capture ultrashort snapshots of physical phenomena was a breakthrough that revolutionized ultrafast science in the 1930-1940s. A few of the examples from Doctor Harold Edgerton's work are shown, such as a bullet going through a ripe banana in **a** and the moving blades of a fan blending an egg in **b**. | Figure adapted from [12]

the manipulation of the delay of the measuring flash of light and by the flash of light's duration τ_f. Pump-probe spectroscopy takes advantage of this.

Following the same principle as a Michelson interferometer, a flash of light is divided into two arms. The light pulse of one of the arms excites the dynamics in a sample (called the pump pulse) while the second arm can then probe those dynamics (the probe pulse) at different delay times with respect to the pump pulse arrival time (time 0). This delay is achieved with a delay stage placed either in the pump or the probe arms that changes the path length a pulse travels before arriving at the samples surface. By repeating the measurement many times at each time delay, statistics that enhance signal to noise ratio can be gathered, and the resulting stroboscopic measurement will have really high τ_f and fps.

Of course pump-probe spectroscopy couldn't be implement without laser technology. The impact of the invention of the laser in fundamental research and technology cannot be overstated. Since its discovery in 1960 [13], the coherence of laser light has changed how we measure time (it is a key component of the development of atomic clocks), how we define distance (the meter is now defined as the length light travel in 1/299792458 of a second) and how we perform ultrafast and ultra sensitive measurements. Using the laser as a source for flashes of light happened fast in the years following its invention, and technology to produce shorter and shorter pulses was quick to advance with the development of Q-switching (producing nanosecond-long pulses of light), active modelocking ($<$ 1 picosecond-long pulses), and passive modelocking (femtosecond-long pulses). These incredibly short flashes of light improved minimum observation durations by nine orders of magnitude since the introduction of the laser [14].

Pump-probe spectroscopy gives the ability to have ultrashort τ_f (on the order of the light pulse's duration) for single frames and high effective fps in the reconstruction of time dynamics for repeatable phenomena. Repetition rates improvements have also progressed, allowing for repetition rates on the order of GHz for pulses of visible light, and above kHz for high harmonic sources used in my work, which means that we can get high amounts of statistics for averaging and high signal-to-noise ratios while taking data.

2.2 Experimental apparatus

Our experimental setup is illustrated in Fig. 2.3. It is a pump-probe setup where the pump and probe pulses are derived from the same amplified Ti:sapphire laser, yielding $< 30fs$ long ultrashort pulses at $4kHz$ repetition rate. The fact that both pump and probe pulses come from the same seed laser means that there is a stable synchrony between both pulses (therefore no time-jitter in the relative arrival time of the pulses to the sample). The pump arm includes two translation stages with retro-reflecting mirrors that allow to modify the path length that the pump pulses go through, without changing the pointing of the beam. We have a high resolution delay state ($< 1um$ time step resolution, which translates to a $< 2 \times 33fs = 66fs$ time delay resolution) with a $20cm$ travel range and a second delay stage ($\approx 5ps$ time delay resolution) $1m$ travel range used for long time delays. Multiple passes on each out setup allow for an $8ns$ time window with high effective fps only limited by our short stage resolution (equivalent to $\approx 1.5 \times 10^{13} fps$).

The pump arm beam is collimated before the delay stages to allow for a stable time delay operation, and is focused onto the sample using two lenses in the beam path, so that the size of the beam spot on the sample can be modified easily. Fig. 2.3 shows one particular configuration of our pump arm, the last stage of the arm can be modified to allow for second harmonic generation with a BBO crystal (upconverting the $790nm$ wavelength light to $380nm$ wavelength) and for the implementation of a transient grating with a $4f$ optical imaging system, as shown in the inset of Fig. 2.3.

The probe arm beam is focused onto an argon filled $5cm$ long hollow waveguide with inner diameter of $150\mu m$ for high harmonic generation (HHG) to take place and up-convert the near infrared pulses into EUV ones. The resulting $< 10fs$ EUV pulses allow for high sensitivity to ultrafast surface dynamics, as it is detailed in the next section 2.2.1. The EUV beam propagates in a high vacuum chamber and is focused onto our samples with a toroidal mirror about $50cm$ away from the sample to a focal size diameter of $\approx 100\mu m$. The reflection (an often times, diffraction) of the EUV pulses from the sample are captured with an Andor X-ray CCD camera (256×1024

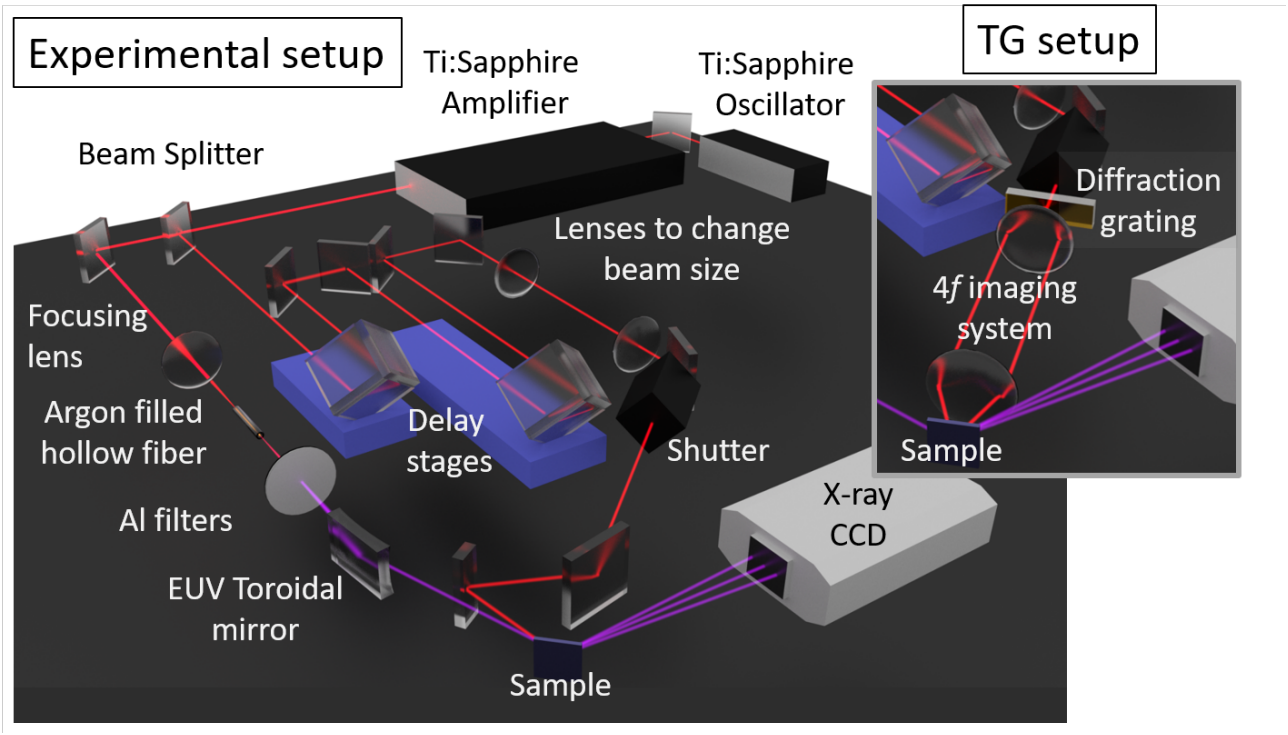

Figure 2.3: **Experimental setup** | A Ti:sapphire amplifier produces ultrashort pulses of typical energies around of $2.0mJ$, $4kHz$ repetition rate, $25fs$ pulse length and spectrum centered around 780 nm in wavelength. The pulses are split into a pump and probe beam. The pump beam path includes two computer-controlled mechanical delay stages with retro-reflectors, one with high step resolution ($\approx 66fs$) and a ps time resolution one. The maximum delay of the line is about $8ns$ with multiple passes on the longer stage (not shown in the graphic). The pump arm final intensity can be adjusted using a waveplate and polarized, and its spot shape and size can be modified as well. A shutter is used to block the pump arm for measurements without any excitation of the sample and 200nm thick aluminum filters are used to reject the remaining pump light onto the CCD camera that gathers the signal coming from the probe arm. The large majority of the energy is used for the probe arm. The probe arm is focused onto an argon filled $5cm$ long hollow waveguide with inner diameter $150\mu m$ for HHG to take place and up-convert the near infrared pulses into EUV ones. The resulting $< 10fs$ EUV pulses are focused by a glancing incidence toroidal mirror onto the samples, where it reflects and diffracts of the dynamically changing surfaces onto an x-ray sensitive Andor CCD. For transient grating (TG) excitation scheme the pump line is modified with a $4f$ optical system after a diffraction grating.

pixels). The Andor CCD is capable of reading at MHz rates the information and have exposures on the ms scale when using vertical binning (adding the contributions of all vertical pixels together, effectively turning the camera into a 1×1024 pixels camera).

Over the time of taking a full scan of many time delays (typically around one-half to one hour), shifts in beam alignment due to thermal load of the system's mirrors or room temperature chances can shift the pump beam location relative to the probe on the sample and it can significantly change the probe beam intensity since the coupling of the beam into the fiber for HHG is strongly dependent on the beam pointing at its entrance.

To mitigate the effects of the beam pointing changing during the length of a scan, we implement an active-feedback beam stabilization system. This system picks off a small portion of the input laser beam before it splits into pump and probe arms and monitor is position and pointing shifts real time with two visible light CCDs. The information gathered by the cameras is processed and fed into two motorized mirrors to compensate for the beam drifts. This system greatly reduces fluctuations in the HHG counts and virtually eliminates long-term drift, typically maintaining the EUV intensity over 5 to 10 hours.

2.2.1 High harmonic generation as a unique ultrafast X-ray probe

High harmonic generation (HHG) is an extreme nonlinear optical phenomena where photons from a driving light pulse are frequency up-converted to a higher energy photon (a higher harmonic). It was first observed by McPherson et al. [15] in 1987. HHG is usually obtained by exciting a medium (a solid or a gas) with an intense electromagnetic field (usually in the form of an ultra short pulse of light). The electrons in the medium are excited past the tunnel ionization potential U_P, tunnel out and gain energy in the driving fields and when recombining with parent ions, will emit the gain energy in the form of photons at a higher energy than the incoming ones. A full quantum model of HHG was presented by Krause et al. in 1992 [16], shortly followed by semi-classical picture of the HHG process, known as the three-step model, was developed by Corkum

et al. in 1993 [17, 18, 19] and captures the essential steps of this highly non linear upconversion process, as illustrated in Fig. 2.4.

In our approach, a high intensity laser pulse is used to drive the process of HHG [20]. The medium consists of a noble gas that is flowing through the hollow glass waveguide. The gas flow is controlled so that the pressure inside the fiber is roughly constant. The high energy ($2mJ$) short pulse ($< 30fs$) is coupled to the waveguide and propagates through the gas. The high intensity of the electric field of the pulse ($> 10^{14}$ W/cm^2) is high enough to significantly modify the Coulomb potential of the atoms in the medium. This enhances the tunneling of electrons out of parent atoms, creating a plasma in the waveguide. These free electrons are accelerated in the field of the driving pulse with charge e and mass m_e and pick up a significant amount of kinetic energy. As the process is driven by a short light pulse, the field gradient will reverse direction as the pulse propagates through the waveguide, making electrons change direction and head back towards their parent ions. Most electrons will just scatter with the ions, but some of them (about 1 in every 10^5) will recombine with parent ions, releasing the gained kinetic energy in the form of a high energy photon. For a given driving laser wavelength, λ, intensity, I, and atomic species with ionization potential, U_I, the highest photon energy that can be generated is [10]:

$$E_{cutoff} \approx U_P + 3.2E_P \approx U_I + I\lambda^2 \ . \tag{2.1}$$

where E_P is the maximum amount of energy an electron can gain during the acceleration, also known as the ponderomotive energy

However, this single atom picture is not enough to generate a bright coherent beam of high harmonic photons. In order to ensure the flux needed for this experiment, generated photons must add constructively. This is where the hollow waveguide geometry makes a huge difference. In the hollow waveguide, the intensity of the driving laser pulse is high enough for HHG to happen in an extended region along the waveguide, which allows for many harmonic photons to be generated. In order to achieve constructive addition, the HHG photons phase velocity needs to match the driving laser one, a condition known as “phase-matching”. This is illustrated in Fig. 2.5.

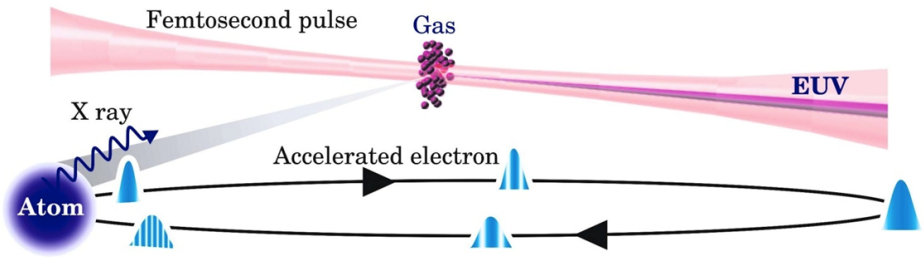

Figure 2.4: **Three-step model for HHG** In HHG, an utlrashort pulse ($< 30fs$) pulse of a light is focused onto a waveguide or gas jet containing a noble gas. The high intensity of the driving pulse fields deforms the Coulomb potential of the atoms, allowing electrons to tunnel out and be accelerated in the laser field. As the pulse propagates and the fields are inverted, some of the electrons are driven to recombine with their parent atoms, releasing an x-ray photon of a high harmonic of the driving frequency. | Image adapted from [19].

The phase velocity of extreme ultraviolet photons in a media is roughly the speed of light and is unchanged by the plasma formed in the waveguide. The infrared driving laser pulse (center at $780nm$ in our experimental setup) phase velocity is strongly affected by both the gas, the waveguide and the plasma that is formed. Phase-matching condition are then achieved by tuning the pressure P in order to balance the these effects [20] such that the following phase-matching condition is satisfied:

$$\begin{aligned} 0 = \Delta k &= q\left\{\left(\frac{u_{11}^2\lambda_0}{4\pi a^2}\right) - P\left((1-\eta)N_{atm}\frac{2\pi}{\lambda_0}\delta - \eta(N_{atm}r_e\lambda_0)\right)\right\} \\ &= \text{waveguide} - (\text{neutral atoms} - \text{ionized atoms}) \end{aligned} \tag{2.2}$$

where q is the harmonic order, u_{11} is a constant related to the lowest-order electromagnetic propagation mode of the waveguide, λ_0 is the driving laser wavelength, a gives the inner diameter of the waveguide, η is the ionization fraction of the gas with number density N_{atm}, δ is a constant (for a given laser wavelength) related to the index of refraction for the atomic gas species and r_e is the classical electron radius.

Phase-matching conditions are only possible until the point where the ionization fraction of the gas cannot be increased to satisfy Eq. 2.2. Understanding the interplay between the phase-matching cutoff and the photon energy cutoff found in Eq. 2.1 gives a guide for the choices of

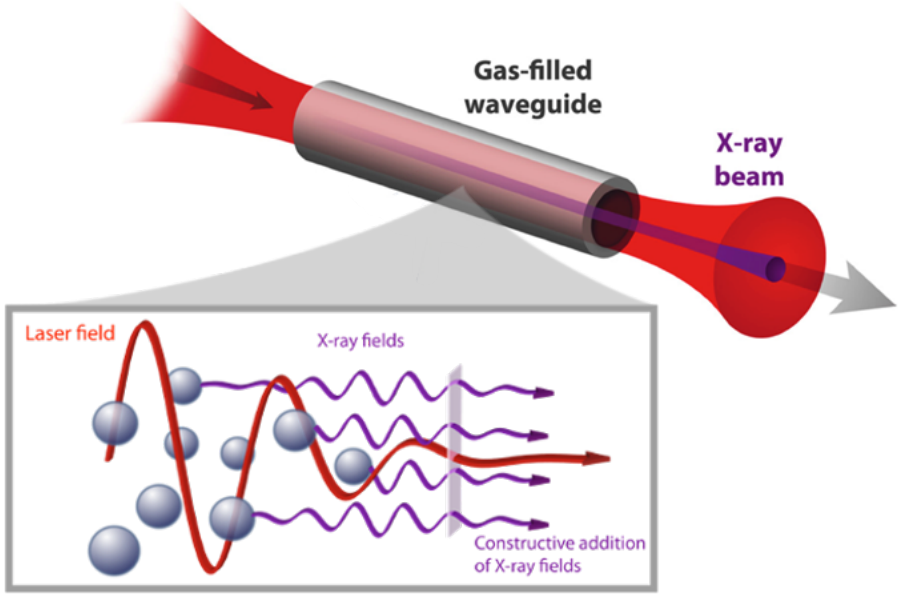

Figure 2.5: **Phase-matching for bright HHG sources**. Phase matching conditions for the emitted high harmonic photons is achieved by tuning the pressure of the gas inside the waveguide. This allows for the high harmonic photons to have the same phase velocity as the driving pulse, therefore ensuring a constructive addition of those photons at the exist of the waveguide and therefore a bright HHG beam | Figure adapted from [21]

gas species, driving laser wavelengths and intensities to optimize the generation of high-harmonic beams. Experimental demonstration of the flexibility of this approach has generated light spanning from vacuum ultraviolet (VUV) to $> keV$ x-rays [10]. In all cases, proof of high coherence of the HHG beams was demonstrated. In the case of this work, the choice of performing HHG with argon gas was to maximize the brightness of the 25^{th} and 27^{th} harmonic of our driving laser wavelength. This allows us to probe systems with a 30nm wavelength light pulses that are not near any electron absorption edges of the materials we study. This particular characteristic allows us to probe the lattice directly, this will be expanded in the section 2.2.4.

HHG beams have many advantages: being a tabletop setup as opposed to large scale facilities allows for more complex and time consuming experiments. The coherence and short wavelength of the generated light allows for a high spatial resolution. Short pulse duration ($< 10fs$) allows for high temporal resolution to probe ultrafast dynamics, and the wavelength and pulse duration are tunable. However, as EUV and soft X-rays are strongly absorbed in media, all setups need to be in high, or ultra high vacuum. Standard optics and mirrors will also not work and diffractive optics of lens-less techniques need to be used in order to manipulate the beams. A lot of effort has been put in finding solutions to these challenges, and they can be overcome. The next section presents our developed experimental technique for probing thermal and acoustic dynamics in nanostructured systems harvesting all the qualities of HHG beams.

2.2.2 Excitation schemes and sample geometries

We implemented two main experimental approaches to generate nanoscale dynamics, both illustrated in Fig. 2.7. The first approach, illustrated in Fig. 2.7a is based on a nano-patterned transducer coated on the surface of the sample of interest that is excited by a Gaussian pump beam. This will generate nanoscale dynamics at length-scales set by the transducer geometry. In this approach, periodic gratings of nanolines or nanocubes of specific height, linewidth and periodicity are coated on the surface of samples using electron beam (e-beam) lithography and lift-off technique by our collaborators at LBNL. In this process, the sample is coated with a thin layer

of a polymer (PMMA in this case). The polymer layer is then exposed to an electron beam with the spatial pattern that is wanted, those exposed areas of the polymer are evaporated. The metal is then deposited onto the sample, but will only successfully grow on the areas of the sample without the polymer layer. Finally, the remaining polymer is removed with a chemical cleaning procedure, leaving the original sample with the patterned metallic structures on top. The nanostructures are usually made of nickel [5, 6, 7], but can also be made of other metals [8]. Nickel and other metals strongly absorb the ultrashort pulse of near infrared pump light. The energy absorbed is transferred to the lattice in a few picoseconds and the lattice expands impulsively. This expansion creates a multitude of surface dynamics and acoustic waves that modulate the diffraction efficiency of the probe beam, and by studying these dynamics we can extract information about the properties of these nanostructures systems. The two temperature model, a particular model to describe the impulsive expansion of the nickel structures upon excitation by an ultrafast light pulse, is discussed in section 2.3.2.1.

In order for this approach to work, all the nanostructures need to be nearly uniformly excited. This is why we use a pump beam diameter of $\approx 400-600\mu m$, larger than the gratings $150\times150\mu m$ and the probe diameter $\approx 100\mu m$. This way the pump intensity does not vary significantly on the probed area of the gratings. We measure the pump size onto a visible CCD camera placed at the same propagation length than the sample and the size can be adjusted (this camera is also used as a pinhole in the alignment of the delay stages to make sure the beam pointing does not vary on the sample face as the data acquisition is taking place).

The height of the nanostructures is of particular importance. Our measurement relies heavily on the phase change introduced in our probe light by a change in height at the sample's surface. In the case of a periodic array of nanostructures, the un-excited sample will already diffract light with a particular efficiency. If the derivative of the diffraction efficiency with respect to change in height of the structures is close to zero, it will reduce the amplitude of the signal generated by this change of height. But, since we can control the initial height of the grating, we can choose a value that maximizes the derivate of diffraction efficiency with respect to change in height and therefore

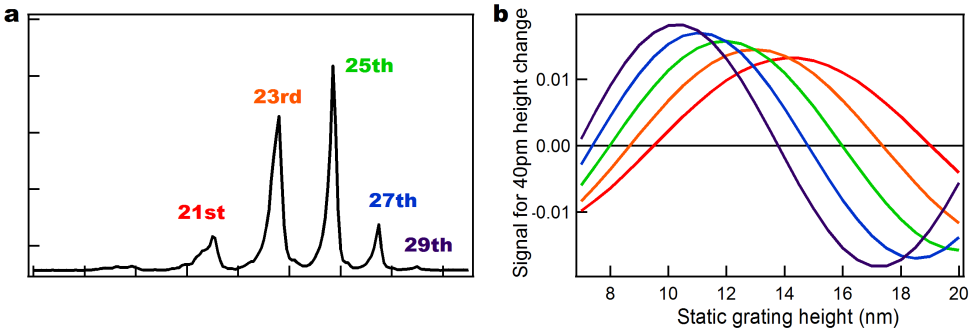

Figure 2.6: **Diffraction efficiency of different harmonic orders as a function of grating height.a**. A typical frequency spectrum of an HHG process using 780nm driving light and Argon gas. **b**. The different diffraction efficiency of the different wavelengths of light to the same displacement (40pm) as a function of the initial height of the diffraction grating | Figure adapted from [22]

our signal. Fig. 2.6 shows that the highest change is diffraction efficiency for a typical vertical displacement of $40pm$ is found in the $9-14nm$ region. Therefore, samples with those heights were fabricated for our experiments.

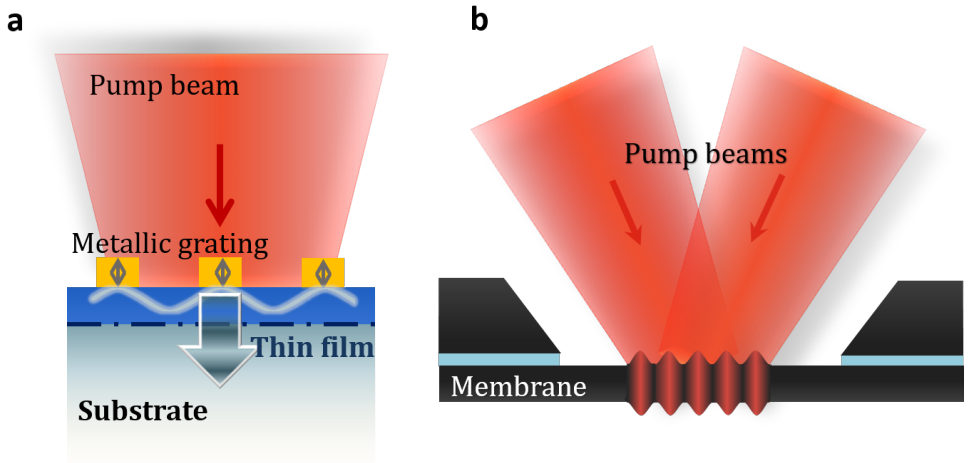

Figure 2.7: **Excitation schemes for EUV nanometrology**. **a** Round beam excitation scheme is used on periodic gratings of nanostructures such that all the structures absorb approximately the same amount of energy. The excited nanostructures heat up and expand, exciting acoustic and thermal dynamics into the substrate. The situation illustrated here refers to an array of nanolines, but the same principle can be applied to nanocubes as well as to embedded nanoparticles **b** Transient grating excitation scheme makes use of two near infrared crossing beams at the surface of the sample which create a sin^2 intensity profile and in turn generate thermal and acoustic dynamics. |

The second excitation approach consists of using the interference pattern created by the overlap of two identical beams of light onto the surface of an absorbing sample, this approach is called optical transient grating (TG). The interference of the beams creates a spatial modulation of the intensity of the light field, which will follow a sin^2 pattern with a spatial periodicity $P_{TG} = \frac{\lambda_{light}}{2\sin\theta/2}$, where λ_{light} is the wavelength of light used and θ is the crossing angle of the two beams of light, as illustrated in Fig. 2.7b. This approach has the advantage of not requiring nanofabrication on the sample. It is widely used using visible wavelengths to study acoustic and thermal dynamics in thin membranes of materials where the transport is mostly one dimensional and easier to interpret [23], but can also be used in bulk materials [24] with the coating of a transducer layer on top of the sample. The main drawback of this technique is the utilization of optical wavelengths of light

limits P_{TG} to hundreds of nanometers. Moreover, different materials will absorb differently the same wavelength of light, making it extremely difficult to study samples with more than one material present. Current work that I am involved in is trying to go beyond this limitation by extending the transient grating concept to shorter wavelengths of light discussed in section 7.2.3, where all materials strongly absorb light and the periodicities could reach the single digits nanometers. As part of those efforts, I implemented a optical wavelength transient grating excitation scheme in our experimental setup and used it to study thermal transport of thin engineered nanomaterials, as discussed in section 7.2.2.

For both excitation schemes, round beam and transient grating, the samples are probed in the same way using our coherent EUV beam focused at the center of the excited area and with a diameter of $\approx 100\mu m$. These experiments generally require a very smooth surface, as a diffuse reflection due to a rough surface can ruin the signal of our probe light. The power of the pump can be changed using a waveplate, being able to vary it from about 10 to $100\mu J$ per pulse, depending on the need (and below the damage threshold of the samples). The wavelength of our pump can also be changed to the second harmonic of the $780nm$ Ti:Sapphire pulse by adding a BBO crystal to the pump line, this can be necessary when exciting materials that might not absorb IR light very well, such as silicon.

2.2.3 Extracting thermal and acoustic experimental signals

The coherence and short wavelength our the EUV probe light allows for diffraction from very small periodicity gratings, such as periodic nanostructures on a substrate, or periodic deformation of a substrate upon transient grating excitation. Since we recover the reflected diffracted light onto a CCD camera, the light gathered is sensitive exclusively to the first few atomic layers in the materials probed. Furthermore, as the index of refraction of EUV light does not change much material to material and with temperature, we can state that our signal is sensitive almost exclusively to the geometry of the surface of the material and therefore to the lattice dynamics. As the surface geometry changes, the diffraction efficiency (the ratio between the zero-order reflected peak and

the diffracted order peaks) changes as well, as shown in Fig. 2.6. This allows us to study the surface dynamics induced by thermal and acoustic excitations by studying the modulation of the diffraction efficiency. Examples of diffraction patterns that are collected onto our CCD camera is shown in Fig. 2.8a and the result after vertical binning is shown in Fig. 2.8b.

Since we are interested in the dynamics of the surface we have to establish a pump-probe approach to the measurement, as described in section 2.1. The ultrashort probe pulses of light from HHG table top sources provide the short pulses of light to capture dynamics with sub-picosecond resolution, and the delay between excitation pulses described in section 2.2.2 and our probe pulse allows us to collect these frames at sub-picosecond time delays. However, the change induced in the diffraction pattern by typical thermal and acoustic dynamics at the nanoscale is very small, about $\approx 10^{-3}$ to 10^{-4} relative change. This tiny difference would be very hard to detect directly as our typical noise in the HHG pulse intensity is in the order of $\approx 10^{-2}$. There are two main strategies we implement to address this challenge. The first one is to compare the diffraction pattern of the probe light from an excited surface $Pump\_on$ to the one from an unexcited one $Pump\_off$ and study the difference between the patterns. This is somewhat similar to homodyning, where a probe pulse is interfere with itself before being analyzed. That way the core part of our signal at a particular delay Δt and pixel i is given by:

$$signal_i(\Delta t) = \frac{Pump\_on_i(\Delta t) - Pump\_off_i(\Delta t)}{\sum Pump\_off_i(\Delta t) - whiteNoise} \tag{2.3}$$

where $whiteNoise$ corresponds to the electronic noise of the CCD camera, given by the average counts of unexposed pixels. This approach alone allows us to detect relative changes in the diffraction pattern down to 10^{-4}.

The pulse intensities resulting from table top HHG sources is high enough to perform many experiments, and low enough to not damage samples (which can be a problem in large scale facilities). However, when performing experiments in reflection mode, where reflectivity to EUV is usually around 10^{-3} for most materials, the amount of photons captured by the X-ray CCD are not enough to perform single pulse measurements (like Edgerton's pictures described in section 2.1).

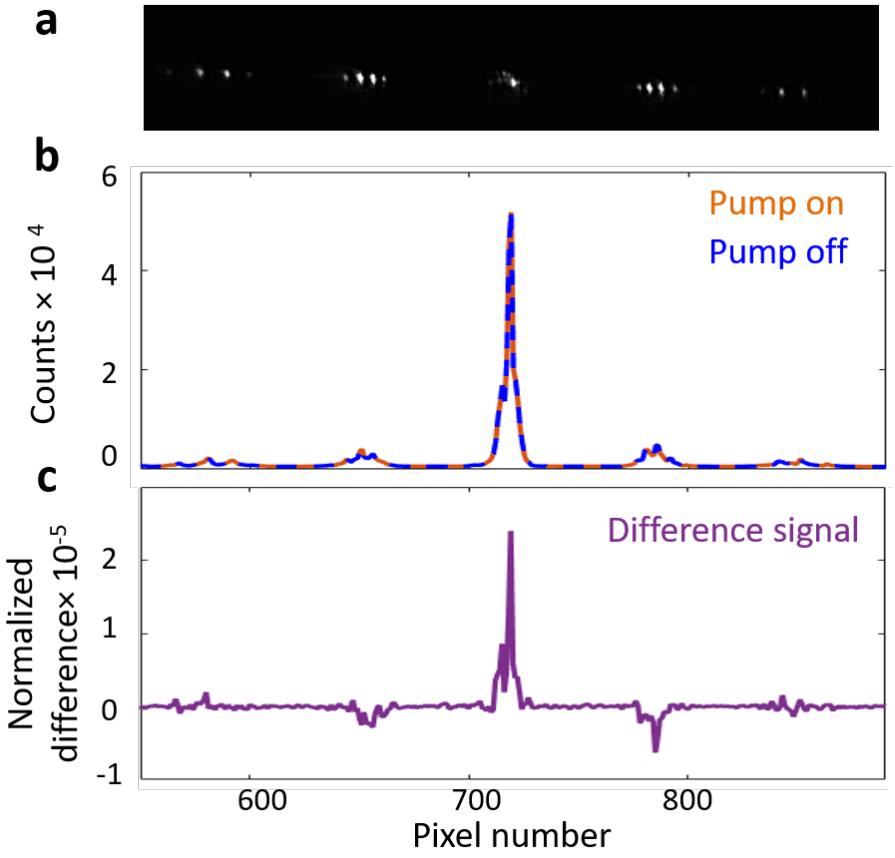

Figure 2.8: **EUV diffraction onto a CCD camera**. **a** shows the camera CCD capture of the diffraction from a periodic grating of nickel nanolines of linewidth $350nm$ and period $1400nm$ on a silicon substrate.**b** shows the result after vertical binning of the pattern for both $Pump\_on$ and $Pump\_off$ acquisitions , where all counts on a column are added together to obtain the plotted 1D diffraction pattern. **c** shows the result of building the normalized difference signal using Eq. 2.3.

Instead, the integrated diffraction from several pulses N_{pulses} is needed to have a solid diffraction pattern on the detector. The value of N_{pulses} will depend on the camera quantum efficiency, the pulse intensity, the reflectivity of the surface of the sample, as well as the diffraction efficiency of the sample itself (some of the scattered light might not hit the camera).

Since we cannot do single pulse measurements, the pulse to pulse variations of the HHG beam intensity can add noise to our measurement. That is why the value for N_{pulses} we use is quite high, reducing the contribution to our noise of the random fluctuations in intensity of the probe beam. we acquire the cumulative diffraction made by N_{pulses}, then read out the counts captured by the CCD camera and divide by N_{pulses} to recover the average single shot diffraction. We perform this operation for a pumped sample ($Pump\_on$) and unpumped one ($Pump\_off$) back to back to make sure the probe beam has as little variation as possible. Finally, we repeat this operation several times (usually 50 to 75 times) to increase our averaging and the decrease the noise that comes from fluctuations in the HHG beam.

This is why the experimental setup includes a shutter shown in Fig. 2.3. For the experiments that I performed during my doctoral work, I used a mechanical shutter that had opening and closing times of $\approx 5ms$. This long opening and closing time introduces an uncertainty in the number of pulses that go through (are stopped) while the shutter is open (or closed), and it didn't allow us to lock the shutter to the train of pulses that came from the laser. This uncertainty in the number of pulses makes it difficult to know how to average the cumulative signals acquired and introduces a new type of noise. In order to minimize this noise we opened the shutter for fairly long times ($30ms$) so that more than 120 pulses when operating at $4kHz$ would go through (or would get stopped) the shutter with an uncertainty of about 1-2 pulses. The shutter is locked-in to the camera, so that the camera only acquires when the shutter is fully open or fully closed. This whole timing setup is illustrated in Fig. 2.9. More recently, we are designing a modification of our experimental setup to use a chopper locked-in with the laser pulses instead of a mechanical shutter, allowing to know exactly how many pulses go trough at each exposure. This upgrade has the potential of increasing the experimental sensitivity even further.

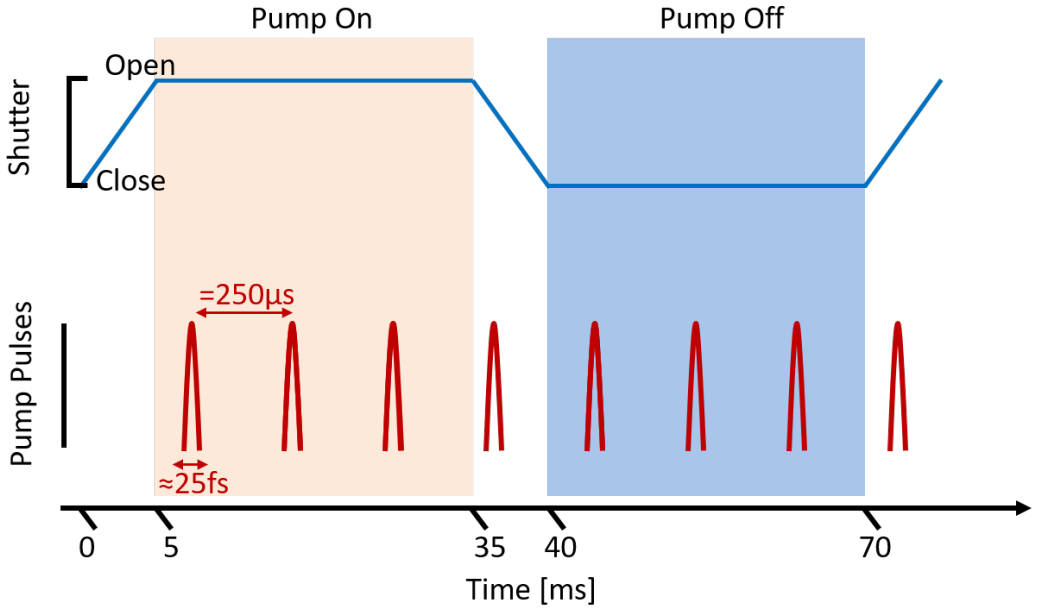

Figure 2.9: **Shutter, camera and laser pulse train timings**. This figure illustrates the timing involved in synchronizing the mechanical shutter, the pulse train and the camera acquisition in our experimental setup. At the top the shutter state as a function of time is shown, at the bottom the laser pulse train is illustrated. Only when the shutter is fully open the camera acquires the $Pump\_on$ signal in orange, integrating over $30ms$ (or approximately 120pulses), and only when the shutter is fully closed the camera acquire the $Pump\_off$ signal in blue, again integrating over $30ms$ (or approximately 120 pulses).

With this strategy to acquire time resolved diffraction patterns we go ahead an extract the important information in it. The diffraction of the coherent EUV light onto a CCD camera is a three dimensional process, and the camera is a two dimensional detector. This is particularly important for the study of 2D gratings (arrays of nano-dots) coated onto a surface. However, for 1D gratings (arrays of nanolines) and TG excitation schemes the diffraction is mostly 1D as shown in Fig. 2.8. We therefore acquire using a vertical binning scheme that has a fast read out speed out of the CCD camera and builds the 1D diffraction patterns that we work with. This is also possible to do for 2D gratings, as the diagonal diffraction orders are naturally separated in the vertical binning from the horizontal ones.

When the diffraction efficiency changes due to surface dynamics, the height of the all the detected peaks changes slightly. Due to conservation of energy, the change in the zero-order peak is equal to the sum of the changes in the diffracted peaks (as the same amount of light is reflected of the surface). This fact has some interesting consequences: First, the zero-order changes contains information about all the surface dynamics present in the sample. Second, adding with opposite signs the changes in the zero-order and the sum of the changes of the diffracted orders enhances your signal. This is why I programmed a data consolidation software (screen-shot shown in Fig. 2.13) that allows the scientist to visualize our data and interactively choose the zero-order peak and the diffracted peaks needed for consolidation of the data. The software adds pixel-by pixel their changes as a function of pump-probe delay time with opposite sign, and normalize by the total intensity of the peaks used to build the signal, as illustrated in Fig. 2.8 and described by Eq. 2.3. A typical resulting time dependent trace is shown in Fig. 2.10.

2.2.4 Intuitive understanding of the experimental signal

An intuitive understanding of the dynamics present in our signal can be gained by thinking about a similar system: the far-field diffraction of a grating where the reflectivity varies as our height does. In our system, the reflectivity varies a little between materials, but most of our signal comes from the phase terms of the diffraction. Although our camera is usually $z \approx 6cm$ from

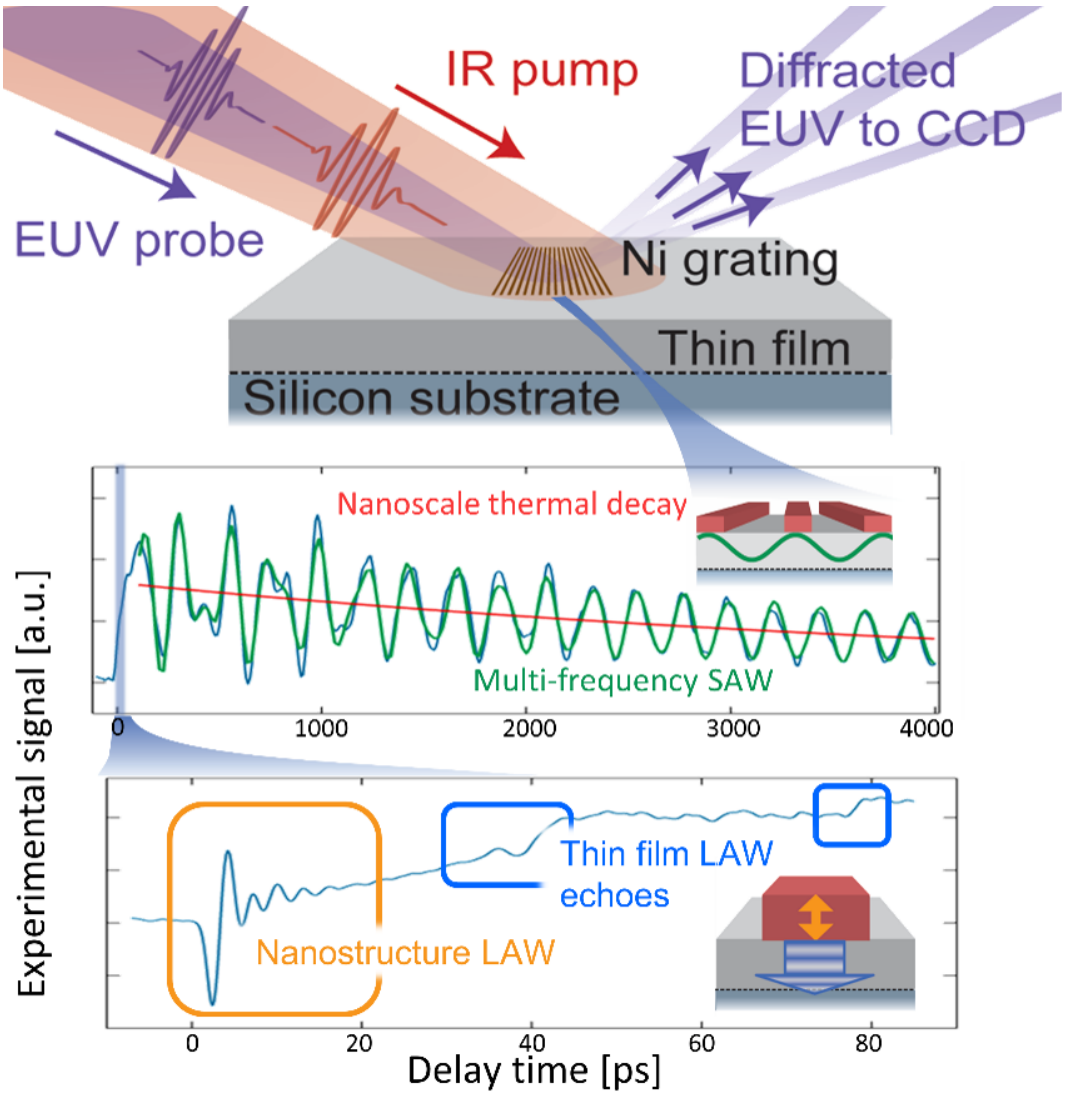

Figure 2.10: **Typical data trace**. An array of Ni nanolines is excited using a near-IR ultrashort pump pulse. The surface dynamics are probed at a later time by diffracting a coherent EUV beam from the laser-heated sample (top). Multiple physical phenomena are tracked through the change in diffraction signal (bottom). First, on picosecond time scales, the resonant vertical breathing mode of the nanolines is visible (yellow), as well as the echoes from longitudinal acoustic waves launched into the film that reflect from the film-substrate interface (blue). On nanosecond time scales, the SAWs dynamics (green) are superimposed on the thermal decay of the Ni nanolines as the energy dissipates into the film and substrate (red). | Figure adapted from [7]

the sample surface, using the Fraunhoffer approximation [25] allows us to gain useful insight. In this approximation, the electric field after transmittance through an aperture can be proven to be the Fourier transform of the aperture evaluated at the spatial frequencies $f_x = x/(\lambda z)$ [26]. We can then use the machinery we have for Fourier transforms on the diffraction gratings where the reflectivity changes as our height does to gain an insight into what information is contained in each peak of the diffraction and in the diffraction efficiency variation. I show the work for the case for our 1D periodic arrays of nanolines, but this can be easily extended to the 2D array of nanocubes, as well as to the deformations caused by a transient grating excitation scheme. A 1D periodic array of nanolines of line width L, complex reflectivity r and period P is well approximated by the convolution of a comb of spacing P with a *rect* function of width L. The Fourier transform is then given by:

$$\mathcal{F}[comb(x/P) \otimes rect(x/L) \times r] = comb(Pf_x)sinc(Lf_x) \times r \tag{2.4}$$

This result corresponds to the far field diffraction from this grating, where the location of the diffraction peaks on the camera are set by the periodicity of the grating, and the height of the diffracted orders is governed by the average single line behavior and the r term. In our experiments, the r term is not as simple as a different reflectivity on the nanostructures (although that term exists), and we are ignoring the complex phase diffraction by a grating of height h. But this rough approximation allows us to see where on the camera we expect to capture information useful to our study, and where does that come from: peak's positions set by P and height of the peaks set by L and h. This already tell us that the time-dependent diffraction efficiency modulation will depend mostly on h, as the sensitivity to it in the real experiment, due to our small probing wavelength, is really high. The resulting diffraction doesn't come as a surprise, but what we really are interested in are the impact of perturbations to the surface profile by the thermal and acoustic dynamics launched in an excited sample. Deformations to the surface, such as the ones coming from LAWs and SAWs will also change the general form of this diffraction. For LAWs, their contribution will change the height of the nanostructures such that it will affect the diffraction pattern and manifest

itself as small discontinuities in our signal, as seen in Fig. 2.10. The signatures of SAWs are very interesting. Following the same approximation as Eq. 2.4, SAWs can be represented by cosine modulation of the reflectivity on the surface of the grating. The fundamental SAW launched by our grating will have a wavelength set by the period P, and higher orders of order n will just have a wavelength be a fraction of that period P/n. When approximating SAW as cosines with amplitude A, in our far-field diffraction approximation we get the following result:

$$\mathcal{F}\left[(comb(x/P) \otimes rect(x/L) \times r) + (comb(x/P) \otimes cos(xn/P) \times A)\right]$$
$$= comb(Pf_x)sinc(Lf_x) \times r + (\delta(f_x - n/P) + \delta(f_x + n/P)) \cdot (PA\sqrt{\pi/2}) \quad (2.5)$$

It is then clear that the diffraction looks like the one without SAWs plus a contribution that aligns perfectly with different diffracted peaks depending on the amplitude and wavelength of the SAWs. The most remarkable feature is that the contribution of SAWs of different order n will contribute to different diffraction peaks of the original $sinc(Lf_x)$ corresponding to the diffraction from a single nanoline (our average nanoline). That means that we can study the different orders of SAWs by just focusing on different diffracted orders on the diffraction pattern. An example of this is shown on an actual data trace in Fig. 2.11.

This then gives us the intuitive understanding of what information is contained in the different parts of our diffraction pattern. Again, the approximation we made ignored the phase terms in our diffraction, which is were most our sensitivity to vertical deformations come from, as will be shown in section 2.3.2.4, but provides a good framework to understand our traces and has analytical solutions.

2.3 Modeling for extracting nanoscale thermal an acoustic properties

We can understand our signal generally using the approach described in section 2.2.4, but in order to extract quantitative information from our experiments we need a more systematic approach to analyze our signal. What implications do certain SAWs frequencies have? How unexpected are the thermal decays observed? These question cannot just be answered using an intuitive under-

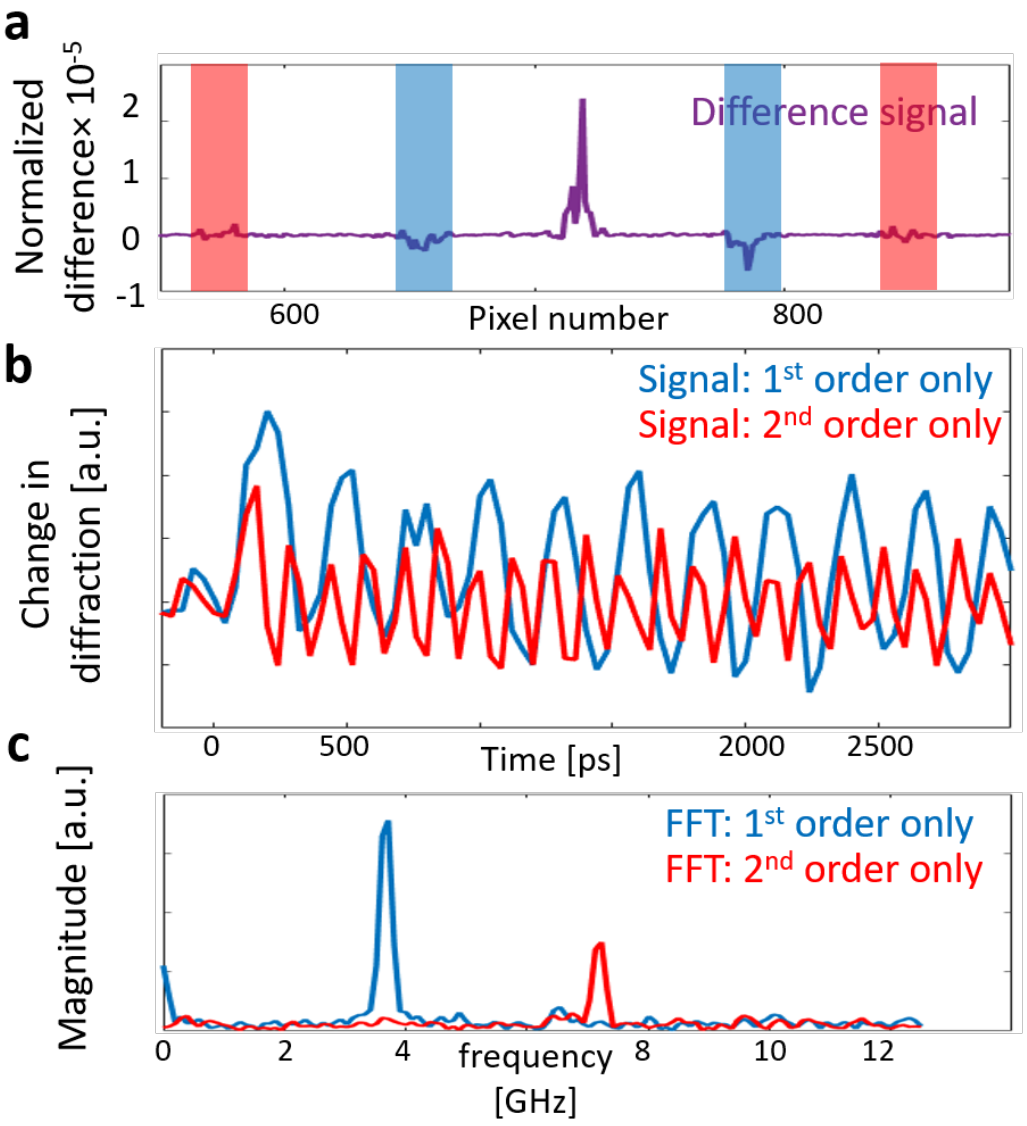

Figure 2.11: **Diffraction peaks highlight specific SAW orders** By selecting different diffracted peaks to build a diffraction difference signal, different SAW orders are captured in it. **a** shows the normalize difference signal from a periodic grating of nanolines of linewidth $350nm$ and period $1400nm$ on a silicon substrate and highlights in blue the contribution from 1st order diffracted peaks and in red the contribution from 2nd order diffracted peaks.**b** shows the result of building our time-resolved signal using only the 1st order diffracted peaks (blue) and the 2nd order diffracted peaks (red). It is clear that the acoustic dynamics captured in the blue data trace are from the fundamental SAW and in the red data trace are from the 2nd order SAW. **c** the Fourier transform of the data traces shown in **b** confirms that when only using the 1st order diffracted peaks the fundamental SAW is present in the data, and that the 2nd order diffracted peaks contain information about the 2nd order SAW.

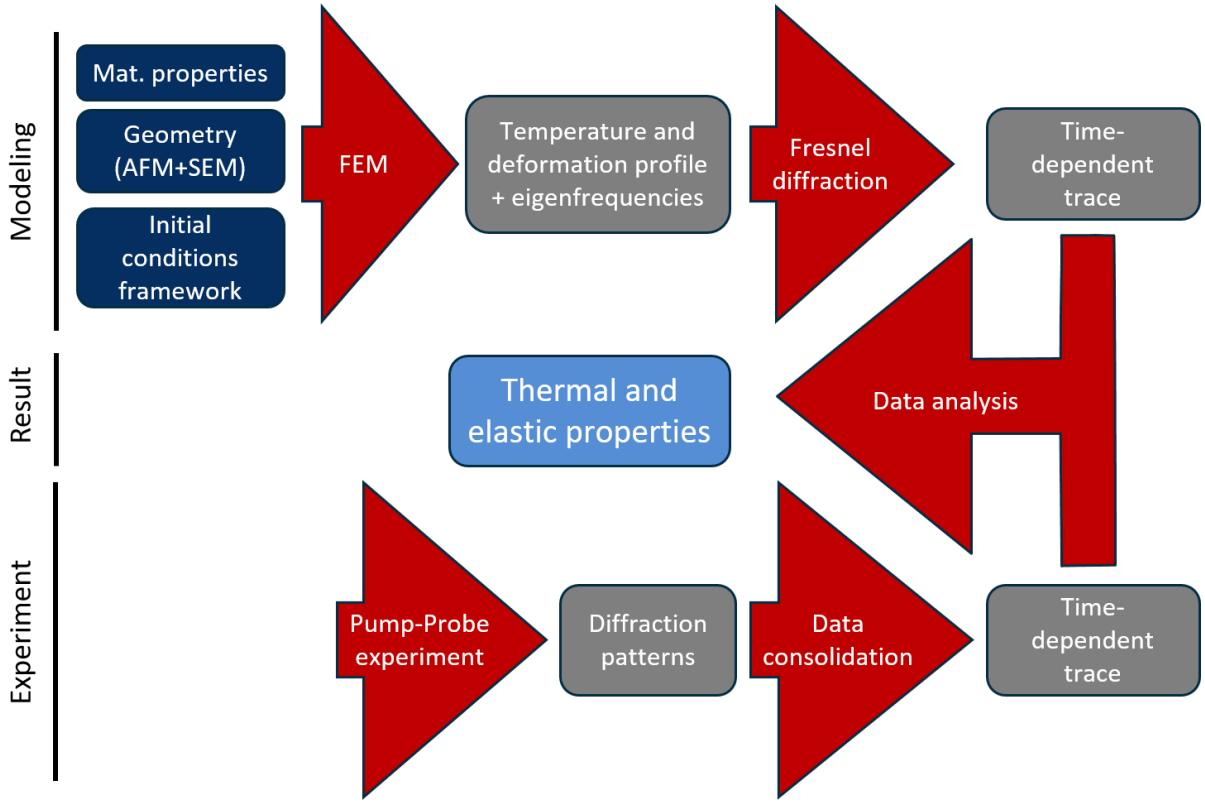

Figure 2.12: **Data flow chart** This chart summarizes the different steps taken in coherent EUV nanometrology to extract thermal and elastic properties of nanostructured materials. The experiment (bottom row) is performed as described in section 2.2 and the resulting diffraction patterns at different delay are consolidated in time traces as the one shown in Fig. 2.10. However, in order to perform the data analysis, modeling of the experiment (top row) is performed to also generate time-dependent traces that can be compared to the experiments. This allows to narrow down the properties of the real sample by sweeping the parameter space of the simulations.

standing. This is why I developed a data analysis flow that allows for a quantitative understanding of our data. This data flow and analysis procedures are illustrated in Fig. 2.12 and has two main sections: Data processing and experiment modeling.

In order to interpret the information extracted from the data we need to have a framework in which to understand our experimental data. Once a model is chosen, we can simulate the experiments with finite element analysis with a wide variety of parameters. In the case of the study of acoustic/elastic behavior, we use continuum mechanics framework which has proven to be valid even for sub-$10nm$‘ layers of material. For thermal transport studies, we use the Fourier model of heat diffusion with and effective parameter that allows us to quantify the observed deviations in the experiment. The details of each framework is presented in the relevant chapters 5 and 3, respectively.

Finally, by comparing the experimental data to the results of the simulations, we can interpret the extracted information and generate new knowledge. In this section, I present the techniques used in the models the data analysis, and further chapters will lay out the details of the data analysis relevant for each experiment.

2.3.1 Data analysis

A few processing steps should be carried out before analyzing data in order to extract information. The first step is to acquire the same data several times (we usually do > 5 different acquisitions, each consisting of several iterations, called “loops”) on different days, or even months (therefore in slightly different experimental situations) so that we can check for consistency and are able to reduce our error bars. Once we have many time-dependent diffraction patterns (both $Pump\_on$ and $Pump\_off$) for the same sample we have to consolidate the time-dependent data traces (like the one shown in Fig. 2.10). This process cannot be fully automatized since experimental data doesn’t always look as clean as simulated ones.

I programmed a software that allows us to quickly build traces by detecting the different peaks in the diffraction pattern, so that we only use the useful information and don’t add any

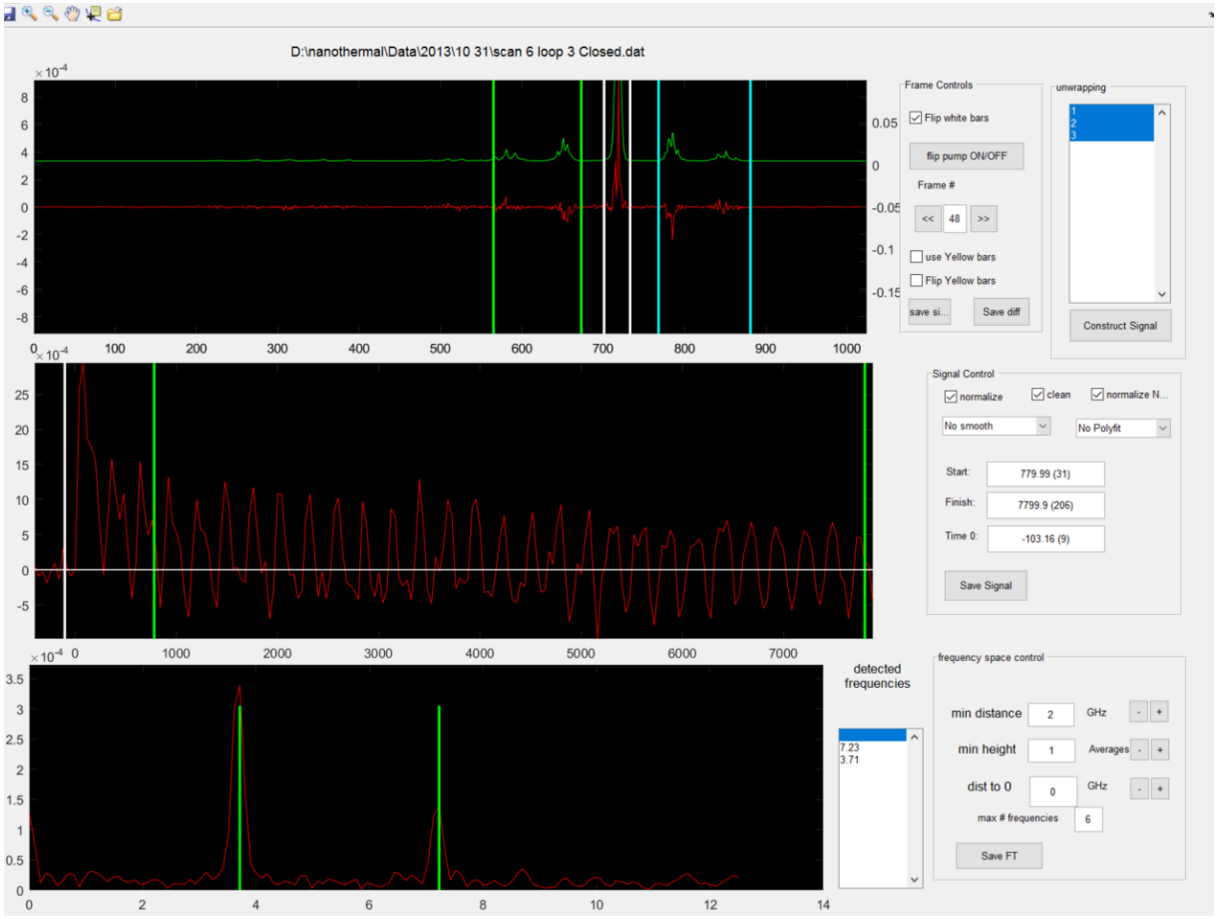

Figure 2.13: **Data consolidation software** In this screen-shot of our tailor made data consolidation software the scientist can visualize on the **top panel** the raw diffraction (green) and raw $Pump\_on - Pump\_off$ difference data (red) for different frames, loops of the scan. This top panel allows for the scientist to move the vertical colored bars on the raw data to choose the diffracted peaks to include in the data consolidation procedure as described in Eq. 2.3. This consolidated time-dependent data trace (red) is updated real time in the **middle panel**, where the scientist can choose the data point corresponding to "time 0", this allowing the software to perform the normalization to reduce the noise present the consolidated trace. The **bottom panel** updates in real time the Fourier transform of the consolidated data trace and automatically detect the peaks present in frequency space. All consolidated data and Fourier transform can then be saved for the data analysis procedure.

noise to our data traces. As our HHG probe beam contains not one, but 3-5 different wavelengths, the diffraction pattern is a complex superposition of the diffraction from the different wavelengths, making the diffracted diffraction peaks wider than just a Dirac comb. The user of the software can choose the camera pixels corresponding to the zero-order peak, first and second order as well, and the software builds a data trace real time according to the procedure described in section 2.2.3, with the inclusion of subtracting the camera white electronic noise. A screen shot of this part of the software is shown in Fig. 2.13. This manual operation by a trained eye allows us to enhance our signal to noise ratio. In general, we include as many diffracted peaks as possible, in order to capture as much of the information in the data trace. In some cases, some loops (iteration) in a scan might not be usable due to thermal drift of the pump or probe beam during the scan, or due to a cosmic ray. In some cases, not all the diffracted peaks are captured by the camera and we have to rely heavily on the zero-order. We need to be able to detect and filter the data in those situations.

Once a consolidated time-dependent data trace is built, it is ready to be analyze for thermal decay as it is described in chapter 3. For analysis of elastic behaviors, we use FFT and Chipr-Z transform to extract the frequencies present in the signal [8] and determine the LAW return time by checking for the characteristic signal in several as shown in Fig. 2.10 measurements of different gratings fabricated on the same sample. This information is key for the analysis of the elastic properties of materials as described in chapter 5.

The data trace, SAW frequencies and LAW return time, together with the grating geometry from AFM and SEM measurements, are the input parameters for our simulation and analysis procedures.

2.3.2 Simulation setup

In order to model our experiments we need two steps of computations: the material's response given the geometries and excitation schemes, and the diffraction of our ultrashort EUV pulse of the material. For the first step, we use finite element method (FEM), a very powerful computational

approach that has become widely available through more powerful computing power and high quality commercial software. FEM is used to solve partial differential equations (PDEs) that can be discretized in their independent parameter space. A particular setup involving the PDEs and a set of initial conditions and geometries can be solved by writing down the conservation equations between neighboring mesh points, building a matrix of this system of equations, and solving it by inverting it.

These broad principles apply to a wide variety of both steady-state and time-dependent problems. For time-dependent systems, the system of equations is solved for a Δt of time, and the result, as well as its approximate numerical time derivatives, are fed as initial conditions for the next time step. This numerical approach is very powerful in solving known PDEs in real geometries, an example of a mesh used in our procedures is shown in Fig. 2.14. Since all of our samples are periodic in nature, we only model a single cell of the system, and apply periodic boundary conditions in the in-plane direction. The mesh needs to be tight enough to be a good numerical approximation to the dynamics set by the PDEs. In order to find the right mesh density, we perform the models with increasingly tighter meshes, until we see that the results are repeatable and don't change with increasing mesh density. The sizes of the simulations are set by the sample's geometry, and the particular model details for different studies are detailed in other chapters. Here we describe the general equations and approximations available for us to work with.

2.3.2.1 Material temperature response to ultrafast excitation pulse

The first step in modeling our experiments, is to model the excitation of the sample under the influence of our pump pulse from which absorbing materials will heat up and expand. We take two different approaches to this, depending on the needs and characteristics of the experiment. .

As long as the dynamics observed are linear with pump power, we can make a very broad approximation when analyzing just the thermal decay without the acoustic behavior. We can then just model the excitation with an initial temperature field composed of two temperatures: T_{hot} and T_{cold}, where T_{hot} corresponds to the temperature of the areas of the sample that absorb the

pump light and T_{cold} is the initial temperature of the rest of the sample. This approach is called the linear quasi-static model. The particular values of the initial temperatures are not important in this case, since we are in the linear regime and the results can be scaled, but we still use realistic values obtained with the two-temperature model and the typical values of our pump pulse energy. In the case of nickel nanostructures on a substrate for example I use the values of $T_{hot} = 593K$ and $T_{cold} = 293K$, calculated using the two temperature model and our laser pump pulse parameters. This approximation only captures quasi-static thermal dynamics, and doesn't capture any of the elastic response of the sample, but it is a very useful approach as it is low cost computationally and allows us to very quickly simulate a wide variety of situations.

If we want to be more accurate in our modeling of the dynamics, we have to model the absorption of the energy contained in the ultrafast pulse by the materials in the system. This is not an easy task, and still an ongoing research subject. Photons in the excitation pulse will interact with the electrons in a metal, these electrons will then scatter with other electrons in $\approx 100fs$ time scale and create a thermalized electron gas.At a longer time scale $\approx 1 - 3ps$ electrons scatter with the lattice, bringing the lattice temperature up. For dynamics past 1 picoseconds after the excitation pulse has arrived, there is a good approximation, especially for metals In our work, we use a two-temperature model for metals, following the work of Banfi et al. [27] and using the model developed by Anisimov et al [28]. In this model, the electrons have a single temperature T_e (the model assumes the electrons are instantaneously thermalized) and are coupled to the lattice temperature T_{ph} in a linear way through a electron-phonon coupling term. This leads to the following system of PDEs to be solved in the metal absorbing the pulse:

$$\begin{aligned} C_e(T_e)\frac{dT_e}{dt} - \nabla \cdot (k_e(T_e, T_{ph})\nabla T_e) &= -g_{e-ph}(T_e) \times (T_e - T_{ph}) + S_{pulse}(t) \\ C_{ph}\frac{dT_{ph}}{dt} - \nabla \cdot (k_{ph}\nabla T_{ph}) &= g_{e-ph}(T_e) \times (T_e - T_{ph}) \end{aligned} \tag{2.6}$$

Where $C_e(T_e)$ and $g_{e-ph}(T_e)$ are the electron heat capacity and electron-phonon coupling in a metal (for nickel the values can be found in [29]), $k_e(T_e, T_{ph})$ is the electron thermal conductivity in a metal, given by the Drude model [30, 29], $S_{pulse}(t)$ is the intensity profile of the laser pulse, and C_{ph}

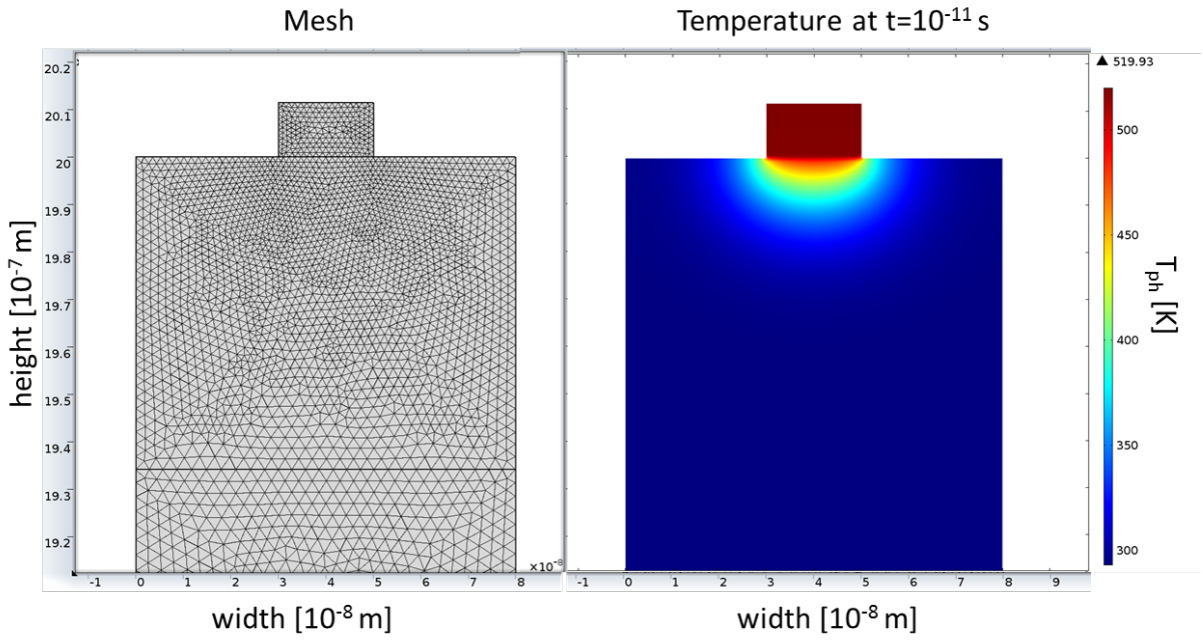

Figure 2.14: **FEM mesh example** On the left is the mesh used on a FEM simulation of a $20nm$ linewidth nickel structure on top of an SiC:H thin film on top of a silicon substrate. The size of the simulation cell is $80nm$, and periodic boundary conditions are set on both left and right side of the simulation cell to emulate a periodic grating with period $80nm$. On the right is the result for the lattice temperature profile at $t = 10^{-11}s$ after a short pulse excited the nickel structure.

and k_{ph} are the lattice heat capacity and thermal conductivity. $S_{pulse}(t)$ at a mesh point below the surface also needs to be modeled correctly, with the appropriate absorption coefficients depending on the materials and the pump light.

These PDEs are of course spatially dependent, and need to be solved for mesh points inside the absorbing material. In our experiments, we use this model for the case of nickel nanostructures. An example of a result is shown in Fig. 2.15. Now, since we are really interested in the surface displacement response of our samples (as that is what we measure in the experiment, not temperature), we will also need to couple these equations to the mechanical response of materials.

2.3.2.2 Thermal-mechanical transient behavior

Our experimental method is really a probe or surface deformation dynamics, therefore we need to simulate not only the temperature response to the pump pulse, but also the deformation field. The PDEs corresponding to this situation are:

$$\begin{aligned} \nabla \cdot (\mathbf{c} : \nabla(\mathbf{u} - \alpha \Delta T_{ph})) &= \rho \frac{d\mathbf{u}}{dt} \\ C_{ph}\frac{dT_{ph}}{dt} + \rho C_{ph}\mathbf{u} \cdot \nabla T_{ph} - \nabla \cdot (k_{ph} \nabla T_{ph}) &= Q \end{aligned} \tag{2.7}$$

where $\mathbf{c}$ is the elastic tensor of the material (more details in chapter 5), $\mathbf{u}$ is the strain field, and ρ is the material density. Q is set to 0 in linear quasi static model, but is set to $Q = g_{e-ph}(T_e) \times (T_e - T_{ph})$ when using the two temperature pulse model, effectively coupling Eq. 2.7 to the first equation of Eq. 2.6.

Again, Eq. 2.7 can also be simplified when certain approximations are made. In the case of just modeling the thermal transient dynamics on the deformation field of the sample, we can use the quasi-static approximation. Effectively, the quasi-static approximation sets the acceleration term (the double time derivative) in the first equation of Eq. 2.7 to 0 at each time step. When we don't us the QS approximation but use the full physics approach, we capture all of the acoustic and thermal dynamics in a sample, as shown in Fig. 2.16, but simulations can take about two orders of magnitude longer.

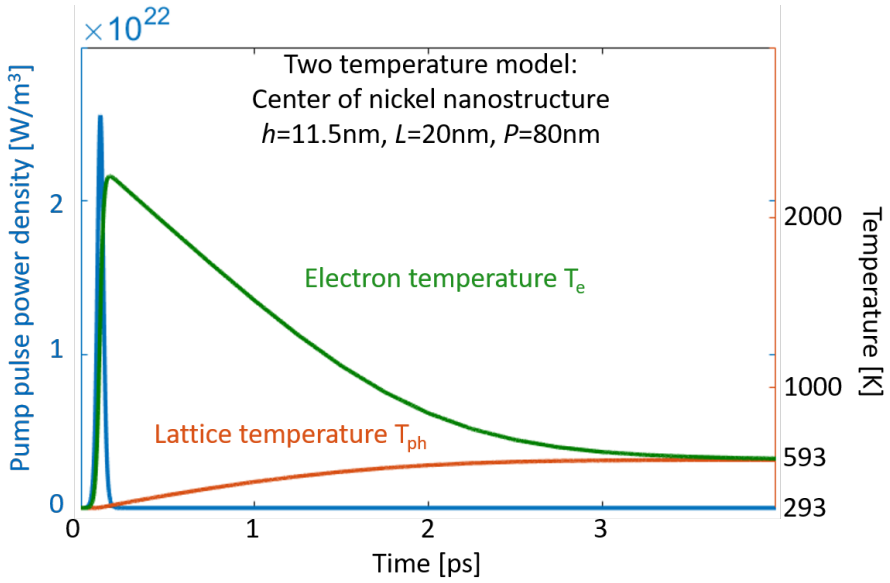

Figure 2.15: **Temperature dynamics in the two temperature model** This graphs shows the calculated response from a $20nm$ linewidth, $11.5nm$ tall nickel nanostructure to a $10\mu J$, $25fs$ long infrared pulse. The values of the variables plotted are calculated at the middle of the nanostructure. $S_{pulse}(t)$ is shown in blue, happening in the first few femtoseconds. The fast response of the electron temperature T_e, followed by the slower response of the lattice temperature T_{ph} are observed. Both then thermalize within $4ps$.

2.3.2.3 Mechanical eigenfrequency analysis of structured materials

We have described so far only transient modeling. However, we make use of another powerful method for acoustic studies which is based on an eigenfrequency analysis of the grating-film-substrate system in thin film studies to extract the normal modes of the geometry. In this case, we solve only the mechanical eigenfrequency equation:

$$\rho(f2\pi)^2\mathbf{u} - \nabla \cdot \sigma = \mathbf{F}_V \tag{2.8}$$

where σ is the stress of the material, F_V the load on it, and f the eigenfrequency of a mode. The FEM solver looks for a solution in a certain range specified by the user, and finds the eigenmodes of this equation. More details are given in chapter 5.

2.3.2.4 Fresnel diffraction of EUV light

The final step needed to compare models to experiment is to be able to model the EUV pulse diffraction from a sample. In order to do this accurately, we use the Fresnel propagation, and take into account both the reflectivity gratings as well as the phase grating due to deformation of the surface. In section 2.2.4, we ignored the phase grating totally, even though that is where most of our sensitivity to surface deformation originates from. In order to simulate the diffraction of EUV light from our surfaces, we implemented a numerical function that takes in a time-dependent surface deformation profile, the reflectivity of the materials involved and the wavelength of probing light and outputs the time-dependent change in the Fresnel integral [26] pattern at the surface of the detector just like in the experiment. As shown in Fig. 2.16, the results are successful in reproducing the dynamics we observe in our experiments (if all the parameters are known).

2.4 Conclusions

Using EUV light has many benefits over other wavelengths when probing lattice dynamics. The clearest one is that the diffraction limit of a system using EUV light, given by $\frac{\lambda}{2NA}$ (where λ is the light wavelenght and NA is the numerical aperture), is at least one order of magnitude

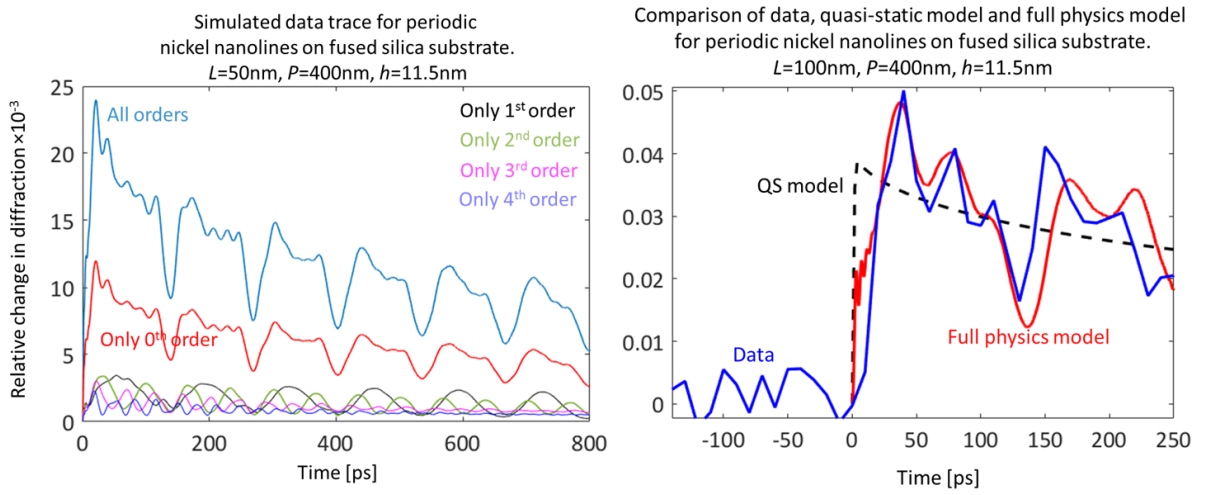

Figure 2.16: **Simulation results** On the left, in blue the time-dependent signal from the simulation of a periodic grating of nickel nanolines of linewidth $L = 50nm$, period $P = 400nm$ and height $h = 11.5nm$ on fused silica. In other colors are the results of the diffraction efficiency modulation when only taking into account certain diffracted orders, and we observe the expected SAW order sensitivity (since it is a simulation results, the noise in the diffraction is 0). On the right, the comparison between two temperature model simulations using the quasi-static approximation (dashed black), using the full-physics approximation (red) and a time-dependent data trace of a periodic grating of nickel nanolines of linewidth $L = 10nm$, period $P = 400nm$ and height $h = 11.5nm$ on fused silica.

smaller than the one of an visible probe. This allows to probe much smaller periodicity gratings and SAW wavelengths than other sources, which is paramount for confining measurement sensitivity within ultrathin film a as we will see in chapter 5 [7, 8]. It is also very relevant for the nanoelectronics industry as the sub-10nm characteristic dimension is being reached, and high density of nanostructures creates systems that cannot be characterized with available tools [3].

Another key benefit, is that the coherence and short wavelength of EUV probe light allows for an exquisite sensitivity to vertical surface displacements of samples. To date, we have observed dynamics corresponding to less than 10pm displacements, much smaller than a single atomic layer. This allows us to measure vertical displacement dynamics of micron scale periodicity samples with competing sensitivity with high repetition, locked-in amplification techniques that can't access smaller nanostructures. This allows us to probe a wide range of geometries both deep into the nanoregime and into the macroscale.

Finally, an often overlooked benefit of using EUV probe light is that the reflectivity of materials to EUV does not change significantly with temperature or with material density. Meaning that EUV probes are insensitive to hot electron dynamics, or material expansion [31], unlike visible probes.

The experimental and modeling setup of EUV nanometrology span a wide range of physical concepts and techniques that come together to harvest the power high harmonic generation for the study of nanoscale lattice dynamics. It uses concepts that have been developed in the last few hundred years and allows for a flexible, robust and reliable tool to analyze nanostructured samples that cannot be characterized otherwise. But most importantly, it allows for a high impact use of table-top HHG coherent sources, as understanding nanoscale ultrafast lattice dynamics is becoming an increasingly important field. The following chapters will discuss specific application of this tool, and will show how the straightforward interpretation of EUV nanometrology has enable us to uncover new phonon physics in condensed matter systems as well as launch and detect the shortest SAW to date.

Chapter 3

Measuring nanoscale thermal transport

Understanding heat flow to inform heat management has been at the center of every manufacturing technology since the mastery of fire. From sword making thousands of years ago, to steel foundries a few hundred years ago, to microelectronics today. The link between motion and heat plays a key role when understanding heat flow. Heraclitus (540-480 B.C.E.) was one of the first philosophers to link motion to heat, as he developed a view of the world where air, water and heat were the building blocks of the Universe and motion was the link between them, as he famously wrote: "everything flows" (which became the current motto of the of the society of Rheology [32]). Later, The Arabian scientist and philosopher Al-Biruni (973-1048 A.C.E) explicitly connected motion with heat generation. He observed that friction produced heat, and he argued that it was the reason behind warmer temperatures near the equator (He was a strong defendant of a spherical earth model, and developed the first models to calculate latitudes, as well as accurately determined the earth radius) [33]. Although he was not right about the conclusion, his observations informed future scientists. Much progress in the understanding of heat was made in the 18th century, where most of the ground work for modern thermodynamics was developed (Lavoisier, Count Rumford, Lord Kelvin, Carnot and finally Bernoulli). In the 19th century heat and work were proven to be equivalent forms of energy and Joseph Fourier, in 1822, developed the mathematical model that is today used to describe thermal transport [34]. The heat equation (also known as Fourier's law of heat dissipation), is based upon some important length-dependent assumptions that break down as the characteristic size of the heat sources, or material size get smaller. Be-

ing able to understand the nanoscale counterpart of heat transfer has become extremely relevant in view of modern technology development and the miniaturization of electronics. Critical applications including high efficiency thermoelectric materials [35, 36, 37, 38], nanoparticle-mediated thermal therapies in medicine [39, 40], nano-enhanced photovoltaics [41], and thermal management in integrated circuits [42, 43, 44] require a comprehensive understanding of energy transport at the nanoscale in solid state matter.

Recent work with low dimensional and nanostructured materials have shown both experimental and theoretical deviations from the macroscopic models. In particular, that the rate of heat dissipation from a heat source is significantly reduced from the one predicted by Fourier's law when the characteristic dimension of the heat source is smaller than the mean free path (MFP) of the dominant heat carriers (phonons in dielectric and semiconductor materials) [45, 46, 47, 48, 49]. However, a complete fundamental description of nanoscale thermal transport is still elusive, and current theoretical efforts are limited by a lack of experimental validation.

This chapter will discuss the application of coherent EUV nanometrology, described in chapter 2, to the challenge of measuring heat dissipation away from nanoscale heat sources when the heat source size and the spacing between sources becomes on the order of the mean free path of the energy carriers in materials. This information is contained in the picosecond- to nanosecond-long thermal decay present in the change-in-diffraction signal shown in Fig. 2.10.

The chapter begins with an introduction to the theoretical background on heat flow in solid state materials and the connection between microscopic and macroscopic views of thermal transport. it then gives a quick review of the different types of nanoscale thermal transport experimental efforts in the literature. The chapter will then present details on our sample preparation and data analysis procedures before focusing on the main results of probing heat dissipation away from periodic nanoscale heat sources in various geometries. I find that not only does heat dissipation from nanoscale heat sources depend on the size of the heat sources, it also depends on the spacing between them. This dependence is quite surprising, and predicts that heat sources that are closer together cool down faster that if farther apart. I present the first experimental evidence of this new

regime of nanoscale thermal transport first [5], and then present systematic experimental testing of its effects on heat dissipation away from 1D-confined heat sources on different substrate materials [6], and in 2D-confined heat sources on Sapphire (in preparation). Finally, I present the model I developed to connect our experimental observations to a funamental material property: the phonon MFP spectrum. I present the first experimentally extracted differential phonon MFP spectra of Sapphire and Silicon substrates [5], and expand on the implications of this model on future work. I conclude the chapter with some discussion on current experimental results that complement ours and a roadmap for future work.

3.1 Theoretical background to thermal transport

In solid state materials, thermal and electrical transport are the main mechanisms behind energy flow. The energy is carried either by the electrons that are somewhat free to move, such as in metals, and by the vibration of the individual atoms around their equilibrium position in the lattice. We will focus on the later, as it is the main mechanism of energy transport in semiconductors, dielectrics, and low temperature metals. More work on electronic thermal transport in thin layers of metals and the joint role of electrons and phonons can be found in [50].

I will start this introduction by working on the simplest solid state lattice: the infinite one dimensional monoatomic lattice, represented in Fig. 3.1. A more in depth work on both this case and more complex ones can be found in [30]. This work will allow for the introduction of the concepts of phonons, phonon mean free path, phonon distribution, and the microscopic description of macroscale bulk thermal conductivity.

In a perfect one dimensional lattice of N atoms, each atom has an equilibrium position in the lattice $R = na$, where a is the lattice vector that defines the distance between two neighboring lattice sites and n is the atom label. In a case of a perfect infinite lattice, if all the atoms are at their equilibrium positions there are no net forces exerted on any atom. However, upon excitation an atom will change its position around the equilibrium position by a distance *u(R)*. Therefore its position at a given time is given by $r(R) = R + u(R)$. How do we characterize the dynamics of such

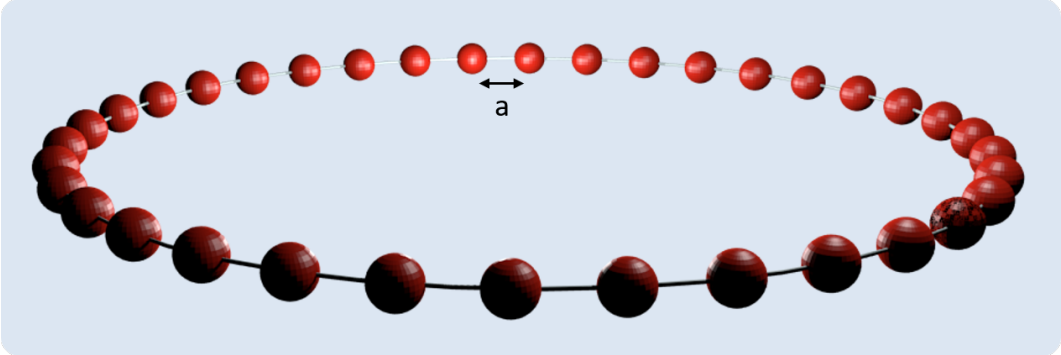

Figure 3.1: **Representation of a one-dimensional monoatomic lattice** Illustration of a one dimensional atomic chain of size $N = 36$, lattice spacing a and periodic boundary conditions.

lattice? First, since the atoms will interact with each other, each pair of atoms will contribute to the total potential energy of the crystal:

$$U = \sum_{RR'} \frac{1}{2}\phi(r(R) - r(R')), \tag{3.1}$$

where $\phi(R - R')$ if the potential between two atoms. If we expand:

$$U = \sum_{RR'} \frac{1}{2}\phi(R - R' + u(R) - u(R')). \tag{3.2}$$

This expression for the potential between all pairs of atoms in the lattice makes it impossible to compute exactly the dynamic properties of any macroscopic lattice. However, a very powerful approximation widely used in solid state physics can be used: the harmonic approximation. This approximation's assumption is that the displacement around the equilibrium position of the lattice's atoms is small. Actually, this condition can be relaxed to only be applied to atoms that have a strong $\phi(R - R' + u(R) - u(R'))$ term. This assumption allows to perform a Taylor expansion of the potential energy of the lattice around the equilibrium positions of the atoms:

$$U = \sum_{RR'} \frac{1}{2}\phi(R-R') + \sum_{RR'} \frac{1}{2}(u(R)-u(R'))\nabla\phi(R-R') + \sum_{RR'} \frac{1}{2}((u(R)-u(R'))\nabla)^2\phi(R-R') + O(u^3). \tag{3.3}$$

The first term is a constant: the equilibrium potential energy of the lattice, which will vanish for time-dependent studies. In the second term, $\nabla\phi(R - R')$ corresponds to the force exerted on site

R by the interaction with the atom at R'. By definition, the sum of the force on a atom R exerted by all other atoms in the lattice when all atoms are in their equilibrium positions is zero, therefore the second term vanishes. We are then only left with the harmonic term (giving the name to the approximation). The assumption of the harmonic approximation can be applied in most situations that are in the linear regime, both for elastic and thermal properties.

$$U = U^{equilibrium} + \frac{1}{2}\sum_{RR'}(u(R) - u(R'))^2\nabla^2\phi(R - R'). \tag{3.4}$$

This result can be generalized to two and three dimensions and more complicated Bravais lattices, and these concept can then also be used for amorphous lattices. Continuing with our simple case study, we apply a further approximation in order to gain insight about energy transport. We will only consider the interaction between nearest neighbors (two for each atom), arguing that the magnitude of the interactions with nearest neighbor is much stronger than with the rest of the atoms in the lattice (which is a pretty good approximation for most atomic potentials). We can then rewrite the potential energy as:

$$U = U^{equilibrium} + \frac{1}{2}\phi(a)''\sum_{n}(u(na) - u((n+1)a))^2. \tag{3.5}$$

This allows us to define the equations of motion for an atom at lattice site na

$$M\ddot{u} = -\phi(a)''(2u(na) - u((n+1)a) - u((n-1)a)). \tag{3.6}$$

This equation is the same as if all the atoms had massless springs of spring constant $K = \phi(a)''$. Now the last piece of the puzzle is to model an "infinite lattice". For the one dimensional case it is pretty straightforward: we can picture the atoms to be arranged in a wring, as illustrated in Fig. 3.1, so that the N^{th} atom is a neighbors of the first atom. We look for solutions of the form:

$$u \propto e^{ikna-\omega t}. \tag{3.7}$$

The periodic boundary conditions require $k = \frac{2\pi n}{aN}$, which leads to solutions that satisfy the following relation:

$$\omega(k) = \sqrt{\frac{2\phi(a)''(1 - \cos ka)}{M}}. \tag{3.8}$$

This result is known as the phonon dispersion relation which contains an acoustic branch of this lattice, plotted in Fig. 3.2. If the one dimensional lattice wasn't monoatomic, but had a two atom basis (with two different masses, two different interaction potentials, same lattice vector basis a and with a basis vectors $a_1 = 0$ and $a_2 = b$), there will then be a second set of normal modes, the optical branch, also plotted in Fig. 3.2 (more in depth analysis can be found in [30]). There is a lot of information contained in this result. First, there will be as many normal modes as there are atoms in the lattice, which when generalized to real size crystals justifies the quasi-continuum treatment of normal modes that is generally applied. Second, it contains the allowed normal modes that have crystal momentum k and energy $\hbar\omega(k)$ depending on the inter-atomic potential and crystal geometrical characteristics. This means that by measuring the dispersion relation of a crystal we can extract the second derivative of the inter-atomic potential given the lattice structure (which can be measured using x-ray crystallography). Third, this is the origin of the quasi-particle: the phonon. A phonon is a normal mode of displacement of a lattice, it is a direct consequence of the global geometry and potential energy of the lattice, but has characteristics of a particle!

A phonon has a momentum k, a velocity $v_k = \frac{d\omega(k)}{dk}$, carries an energy $\hbar\omega(k)$, is massless (like photons), travels a mean time before scattering τ_k (or inversely, has a mean free path $\lambda_k = v(k)\tau_k$, and follows the Bose-Einstein statistics.

The density of states of phonons $g(k)$ refers to the quantity of available states there are in k-space. This quantity is not easily calculated (Molecular dynamics and lattice Boltzmann calculations are used to get good approximations to it), but a quick approximation for the acoustic branches can be derived by approximating $\omega(k) = v_s k$, that is to say that close to $k = 0$, the acoustic branch shows a linear relationship between k and $\omega(k)$. The slope of the acoustic branch close to $k = 0$) corresponds to the speed of sound in the material. The Debye approximation uses this value to describe material properties and is as follows. In three-dimensions: $g(k) = \frac{k^2}{2\pi^2}\frac{1}{v(k)}$ for $|k| < k_D$ and zero otherwise, where : $k_D = \frac{(}{6\pi^2 N}V)^{\frac{1}{3}}$ is the cutoff wavevector for the acoustic branch, and V is the unit cell volume in k-space.The region where it is non zero does NOT define the Brillouin zone, as it is just an approximation. Each phonon mode corresponds to a normal

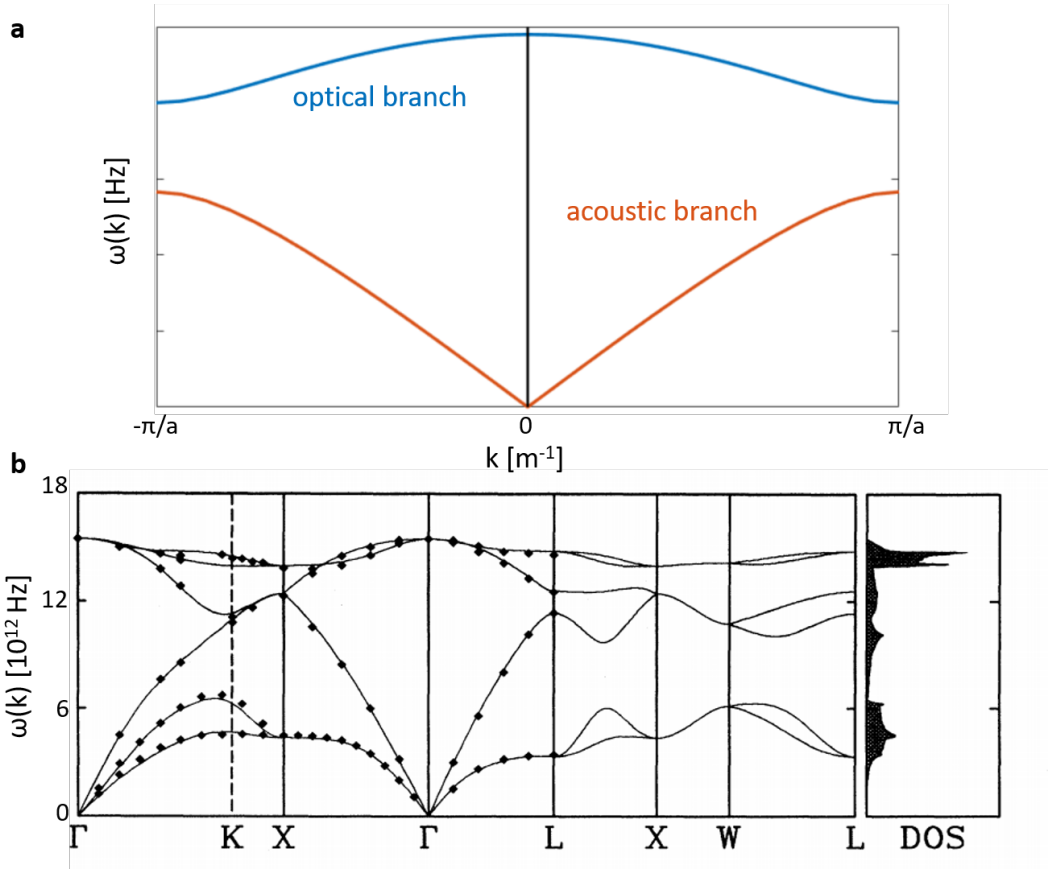

Figure 3.2: **Phonon dispersion relation for a one dimensional two atom lattice and silicon a** Results of the dispersion relation of an two atom basis one dimensional chain of atoms. In blue, the optical branch, in orange the acoustic branch. **b** Results of ab-initio calculations of the three dimensional silicon dispersion relation (solid lines) compared with experimental measurements (diamonds), from [51]. The first three acoustic branches and the first three optical branches are visible. On the right, the calculated density of states.

mode of the crystal, but many phonons of a particular mode can be present at any point in time in the same volume. Phonons follow the Bose-Einstein statistics just like photons, the main difference is that not all values of k are allowed, as the values are limited to the first Brillouin zone and that three polarization s of phonons exist in 3D matter, in contrast with two polarizations for photons. With this, we can define a thermal energy density:

$$U(\mathbf{x}) = \sum_s \int \frac{d\mathbf{k}}{(2\pi)^3} \frac{\hbar\omega_s(\mathbf{k})}{e^{\beta\hbar\omega_s} - 1}, \tag{3.9}$$

with the integration being over the first Brillouin zone in momentum space, $\beta = 1/kT$.

With this information, we can now start building a full macroscopic picture of thermal transport. At the microscale, at a given temperature there will be a phonon spectrum present in the material. This spectrum depends on the temperature, but for small changes in the temperature i.e. $\frac{\Delta T}{T} < 10\%$ the spectrum can be approximated as not temperature dependent. During this introduction, we have so far derived the dispersion relation for phonons in a crystal, however this only tells us the allowed phonon modes in a crystal $\omega(k)$, the speed at which a particular mode travels $v_k = \frac{d\omega(k)}{dk}$. We also have derived the 3D the density of states, but in order to tackle transport situations more information is needed. In particular the scattering lifetime of a particular phonon mode τ_k and what happens once it scatters. The phonon-phonon scattering terms that are contained in the anharmonic terms are ignored in Eq. 3.4 (therefore not contained in our harmonic approximation results). These terms are responsible for thermal resistivity (thus dictate dynamic behavior) and are challenging to be both calculated and measured. One possible approximation is to use the concept of mean free path, or relaxation time, for each phonon mode independently (the relaxation time approximation, or RTA). This approximation provides an answer to the "how long does a phonon travel before scattering" question. I will revisit this approximation more in depth in chapter 4.

At the macroscale, a very useful and popular (but as we will see, not always accurate) approximation if the grey-MFP approximation. In this approximation, instead of dealing with the complexity of the phonon spectrum of a material, an average phonon mode is used. That allows the

treatment to be much simpler, with a single average (grey) MFP, energy, frequency, lifetime, etc. However, it is important to point out that the derivations done in the grey-MFP approximation can be extended to the full phonon spectrum if one approximated the different phonon modes behave independently, (under the RTA approximation). Within the grey-MFP approximation, a derivation of the heat flux at some point x along a thermal gradient in the x direction can be made. For a given grey-phonon number density $n_{grey}(x)$, energy $\hbar\omega_{grey}$ and average velocity $\frac{v_{grey}}{3}$ (since phonons move randomly, the average speed in a particular direction is $\frac{1}{3}$ of the average three-dimensional one), the heat flux q_x through a surface at x is given by the particle fluxes in each direction from a distance equal to what they move at an in a time t.

$$q_x = \left(\frac{1}{2}(n_{grey}(x')\hbar\omega_{grey}\frac{v_{grey}}{3})\right)\Bigg|_{x-\frac{v_{grey}}{3}t} - \left(\frac{1}{2}(n_{grey}(x')\hbar\omega_{grey}\frac{v_{grey}}{3})\right)\Bigg|_{x+\frac{v_{grey}}{3}t} \tag{3.10}$$

since the random motion of phonons implies half will be moving in each direction. Applying a 1st-order Taylor expansion around $\frac{v_{grey}}{3}t = 0$ for each component implies

$$\begin{aligned} q_x = \frac{1}{6}\left((n_{grey}(x)\hbar\omega_{grey}v_{grey}) - v_{grey}t\frac{d(n_{grey}(x)\hbar\omega_{grey}v_{grey})}{dx}\right) - \\ \frac{1}{6}\left((n_{grey}(x)\hbar\omega_{grey}v_{grey}) + v_{grey,x}t\frac{d(n_{grey}(x)\hbar\omega_{grey}v_{grey})}{dx}\right) \end{aligned} \tag{3.11}$$

But because we are in the grey-MFP approximation the energy density is just $U(x) = n_{grey}(x)\hbar\omega_{grey}$, so:

$$\begin{aligned} q_x &= -\frac{v_{grey}^2 t}{3}\frac{dU}{dx} \\ &= -\frac{v_{grey}^2 t}{3}\frac{dU}{dT}\frac{dT}{dx} \end{aligned} \tag{3.12}$$

Furthermore, $\frac{dU}{dT}$ is the volumetric heat capacity C_V. We start recognizing a familiar form in Eq. 3.12. If we set $t = \tau_{grey}$ (which is usually on the order of a few picoseconds at most, making the Taylor expansion a pretty good approximation), we see that $v_{grey}\tau_{grey} = \lambda_{grey}$ and $K_{bulk} = \frac{1}{3}C_V v_{grey}\lambda_{grey}$ (which conceptually corresponds to the energy flux a phonon can transport over the distance it travels), we get:

$$q_x = -K_{bulk}\nabla T, \tag{3.13}$$

the well-known form of Fourier's law.

However, the validity of Fourier's law relies on many phonon collisions over the length scale of transport that is being considered. This main assumption breaks down for length scales that are on the order of the phonon mean free paths.

An intuitive example, although not from a solid state physics, comes from examining thermal transport in a gas in a cold room in Alaska. The barely functioning furnace at the center of the room heats up molecules in the air close to it, giving those molecules higher velocity. Through a multitude of scattering events and random walks the energy is diffused throughout the room, although not enough to make it a comfortable temperature. From your observations of the temperature gradient and the size of the room you could extract the thermal conductivity of air and use a diffusive model to describe the transport observed accurately. If instead of looking at the room as the volume of transport we zoom in and consider only a λ^3, where λ is the MFP of air molecules, of air adjacent to the furnace, a diffusive model using the parameters derived when studying the room as a whole would not describe the heat flux through this cube of air, the transport would rather look ballistic. This diffusive/ballistic duality picture is very present in many nanoscale studies involving molecules or fluids. When we try to apply it to phonons an extra layer of difficulty arises as i) the number of phonons is not conserved and ii) the MFP spectrum and energies for phonons is much wider than in a classical molecular transport situation. Phonon spectrum can span 3 or more orders of magnitude in both energy and in MFP for many materials.

This is why, when describing nanoscale thermal transport, we must resort to the more fundamental Boltzmann transport equation (BTE). The BTE is in essence a statement of conservation of energy for each differential volumetric element of the space being considered, it is very useful in the study of photon dynamics, neutron transport in nuclear reactors, charge transport for phonon transport. It is based on tracking the temporal perturbations of the distribution function of the particles (or quasi-particle) that one is studying: f. It is at its core a statement of conservation of energy:

$$\frac{\delta f}{\delta t} + \frac{\delta \mathbf{r}}{\delta t} \cdot \nabla_{\mathbf{r}} f + \frac{\delta \mathbf{p}}{\delta t} \cdot \nabla_{\mathbf{p}} f = (\frac{\delta f}{\delta t})_{collision} \tag{3.14}$$

This form of the BTE can be rapidly put in more comprehensible terms with a few obvious replacements:

$$\frac{\delta f}{\delta t} + \mathbf{v} \cdot \nabla_{\mathbf{r}} f + \frac{\mathbf{F}}{\hbar} \cdot \nabla_{\mathbf{k}} f = (\frac{\delta f}{\delta t})_{collision} \tag{3.15}$$

We can explicitly bundle the scattering terms into the collision term $(\frac{\delta f}{\delta t})_{collision}$. This is where the difficulty lies. In the case of phonon transport it will contain terms belonging to phonon-phonon scattering and phonon-electron scattering when relevant (in metals, for example). In the relaxation time approximation each phonon mode has an independent lifetime, and therefore the equation that has to be solved for **each** phonon mode becomes:

$$\frac{\delta f}{\delta t} + \mathbf{v} \cdot \nabla_{\mathbf{r}} f + \frac{\mathbf{F}}{\hbar} \cdot \nabla_{\mathbf{k}} f = \frac{f - f_0}{\tau} \tag{3.16}$$

Where, f_0 is the equilibrium distribution function. Solving the BTE exactly, even for a perfect infinite three-dimensional crystal, is computationally intensive. Different approaches have been taken, but as Massilta and Minnich put it "The calculation is quite formidable" [52]. A phonon spectrum in a material is very complex, with many variables and parameters. A common way of investigating the phonon spectrum is based on the phonon differential conductivity MFP spectrum, an example of this is shown in Fig. 3.3. In this space (MFP space), the contribution to the thermal conductivity of phonon modes is plotted against their MFP. This is a useful way of relating the thermal transport (the differential conductivity) with respect to a length scale that will be on the order of the geometry of the experiments when nanostructures are studied.

To finalize this section, I am going to show how the BTE and Fourier's law relate to each other. Starting from Eq. 3.16, defining $g = f - f_0$:

$$\frac{\delta f_0}{\delta t} + \frac{\delta g}{\delta t} + \mathbf{v} \cdot \nabla_{\mathbf{r}} f_0 + \mathbf{v} \cdot \nabla_{\mathbf{r}} g + \frac{\mathbf{F}}{\hbar} \cdot \nabla_{\mathbf{k}} f_0 + \frac{\mathbf{F}}{\hbar} \cdot \nabla_{\mathbf{k}} g = \frac{g}{\tau} \tag{3.17}$$

Then, we can apply the following assumptions that define the linear regime, where the deviations from equilibrium f_0 of f are small.

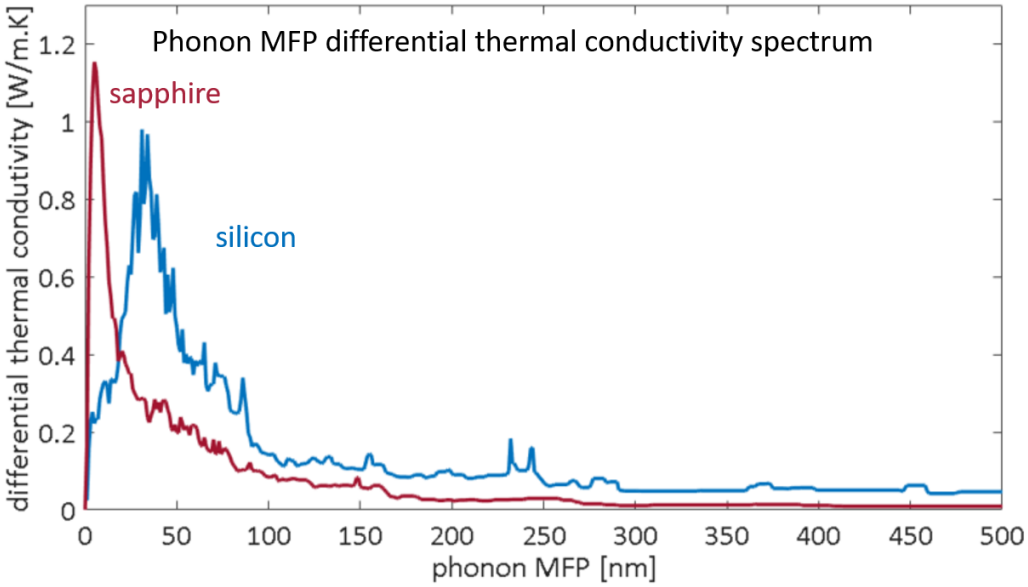

Figure 3.3: **Calculated phonon MFP spectrum for silicon and sapphire substrates** Calculated differential conductivity as a function of phonon MFP spectra for silicon (blue) and sapphire (red) substrates. Here, only the contributions from phonons with MFP$< 500nm$ is shown to highlight the difference in the materials. | from [5]

(1) the transient terms are negligible (with respect to τ time frame)

(2) $g << f_0$.

(3) $\nabla_{\mathbf{r}} g << \nabla_{\mathbf{r}} f_0$ and $\nabla_{\mathbf{k}} g << \nabla_{\mathbf{k}} f_0$

Under these assumptions the linearized BTE can be written down:

$$f = f_0 - \tau(\mathbf{v} \cdot \nabla_{\mathbf{r}} f_0 + \frac{\mathbf{F}}{\hbar} \cdot \nabla_{\mathbf{k}} f_0) \tag{3.18}$$

Because $f_0 = \frac{1}{exp(\hbar\omega/k_B T)-1)}$ only depends on T we can then drop the gradient in momentum space. This final step always feels like a big simplification, but let's stick with it for now.

$$f = f_0 - \tau(\frac{df_0}{dT}\mathbf{v} \cdot \nabla_{\mathbf{r}} T) \tag{3.19}$$

With this final expression, we can then analyze the heat flux in a material going in the x direction:

$$\begin{aligned} J_{q,x} &= \sum_{polarization} \int_{-\infty}^{\infty} \frac{d\mathbf{k}}{(2\pi)^3} v_x \hbar\omega f \\ &= \int_0^{\omega_{max}} d\omega \int_0^{2\pi} \int_0^{\pi} v \cos\theta \hbar\omega f \frac{g(\omega)}{4\pi} \sin\theta d\theta d\phi \end{aligned} \tag{3.20}$$

where ω_{max} is the maximum allowed frequency. Now, by using Eq. 3.19 into the equation we obtain:

$$J_{q,x} = \int_0^{\omega_{max}} d\omega \int_0^{2\pi} \int_0^{\pi} v \cos\theta \hbar\omega (f_0 - \tau(\frac{df_0}{dT}\mathbf{v} \cdot \nabla_{\mathbf{r}} T)) \frac{g(\omega)}{4\pi} \sin\theta d\theta d\phi \tag{3.21}$$

It should be clear that the first part of this expression that performs the integration over $()v \cos\theta \hbar\omega f_0 \frac{g(\omega)}{4\pi} \sin\theta)$ vanishes, as f_0 is the equilibrium distribution. We also will use the fact that the specific heat per unit frequency is $C_\omega = \hbar\omega g(\omega)\frac{df_0}{dT}$This leaves us with:

$$J_{q,x} = [\frac{1}{2} \int_0^{\omega_{max}} \int_0^{\pi} \tau v^2 C_\omega \sin\theta \times \cos\theta^2 d\theta d\omega] \times \frac{dT}{dx} \tag{3.22}$$

Which is Fourier's law! The definition of thermal conductivity, if v and τ are isotropic becomes

$$k = \frac{1}{3} \int_0^{\omega_{max}} \tau v^2 C_\omega d\omega \tag{3.23}$$

Hopefully it is clear by now how all of the different assumptions can fail when considering length-scales and/or time-scales that are on the order of the phonon MFP and lifetimes. Let us dive in the topic of nanoscale thermal transport size effects.

3.2 Review of nanoscale thermal transport experiments

Nanofabrication techniques can nowadays synthesize single atomic layer films or nanostructures with $<< 10nm$ dimensions, with single atom precision. Having access to exciting new samples with a wide variety of geometries has given a unique opportunity for a very diverse set of experiments around the study of nanoscale thermal transport. Here I present a brief overview of the experimental techniques that aim at measuring nanoscale thermal transport, more in depth reviews can be found in [35, 53, 54, 55].

Since phonon MFPs span the range of a few nm all the way to several μ, we can expect a lot of non-diffusive dynamics in nanoscale geometries, including in existing microelectronics that are sitting right in our pockets. Although this is true, different non-diffusive transport phenomena will happen depending on the geometry, leading to different "types" of nanoscale thermal transport experiments. Each one might be performed on the same materials (with the same phonon spectrum), but different experimental geometries will interact very differently with the material properties. The following list is not an exhaustive one, but provides a good first look at the literature:

(1) The study of the impact of constraining geometry on thermal transport properties across a material, it includes the study of thermal transport across nanocubes, nanolines, and thin films [37, 53, 56, 57, 58, 59, 60]. Illustrated in Fig. 3.4a.

(2) The study of transport in low-dimensional materials: 1D(molecules) [50] and 2D (graphene, MoS2) materials [61]. Illustrated in Fig. 3.4a.

(3) The study on the impact of defects, random and organized and both bulk and surface, on thermal transport. This includes the study of phononic meta-materials [62, 63, 64, 65] , and the study of thermal transport impact of surface roughness[66, 67], or of engineered surface defects (NPM) [38, 68]. Illustrated in Fig. 3.4b.

(4) The study of the impact of interface quality and properties on thermal transport between materials, critical for usable devices [69, 70, 71, 72, 73, 74, 75]. Illustrated in Fig. 3.4c.

(5) The study of the impact of energy distribution geometry on thermal transport. That is thermal transport from nanoscale heat sources in a system (bulk, films and nanolines)[47, 76, 77, 78, 79, 58, 80, 23] [45, 5, 6]. Illustrated in Fig. 3.4d.

I focus on the last category as our experiment studies heat dissipation away from periodic nanoscale heat sources on different substrates. Non-diffusive effects due to the size of heat sources have been known for over two decades. Chen [81], in 1996, was the first one to work out the limiting case of the heat flux away a hot spherical nanoparticle at a distance shorter than the MFP and proved that even though the phonons move ballistically, the energy transport resembles radiative transport. However, he also pointed out that the size of the heat source played a key role in this effect. If the diffusive model is used to model these situations, it over predicts the heat flux away from the nanoscale heat sources as illustrated in Fig. 3.5. Much work has gone into exploring the transition from diffusive transport to quasi-ballistic transport away from nanoscale heat sources with different geometries, dimension, and periodicities. In particular, the study of the non-steady state situations has become of great interest, as ultrafast measurements on the scale of nanoscale thermal transport are now possible.

In order to study the impact of confinement of heat sources on the heat dissipation dynamics, the first step is to create nanoscale heat sources. There are two main techniques used to generate them: i)using direct optical excitation with a particular spatial distribution such as a focused laser beam [47, 76], or to use the frequency-dependent absorption length into the material to create confined heat sources near the surface of the materials [82] and ii) creating a transient grating by interfering different beams of light onto a sample's surface [77, 78, 79, 58, 80, 23] . In all these references a thin layer of well-characterized material is deposited onto the samples of interest is needed to strongly absorb the excitation light and to provide a direct access to the temperature dynamics of the surface as its reflectivity to the probing light is very sensitive to temperature changes. These approaches have the advantage of being fast, not too expensive, with low complexity nanofabrication needs. However, they are limited by the diffraction limit of the

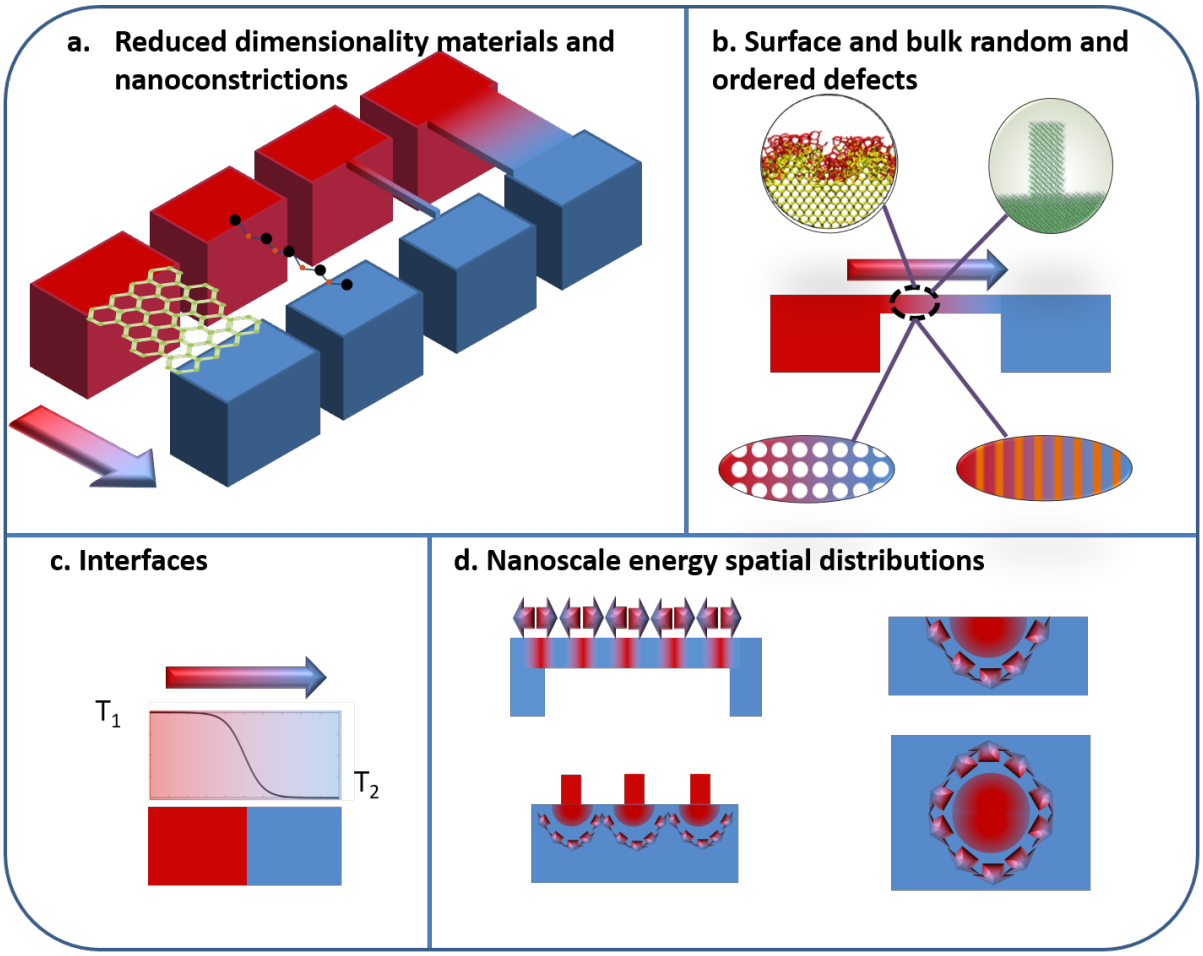

Figure 3.4: **Different types of nanoscale thermal transport studies a** Study of nanoscale thermal transport in low dimensional and constrained geometries.**b** Study of nanoscale thermal transport when defects (both organized and disorganized) are present | [67] [63].**c** Study of nanoscale thermal transport across interfaces. **d** Study of nanoscale thermal transport away from nanoscale heat sources in thin films, surfaces and bulk.

visible light used to create the confined nanoscale heat sources to hundreds of nanometers. In order to circumvent this, the use of patterned transducers has become more common. In this case the energy distribution geometry is not set by the pump light, but by the nanofabrication geometry. In this scenario,the visible wavelength as a probe light also represents a challenge. Recently, patterned transducer experiments that use visible light probes have been successful [83, 84]. These measurements are based on the principles of time dependent thermoreflectance (TDTR), a powerful technique first developed by Paddock and Eaesly in 1986 [85] that is today a standard technique to extract the thermal conductivity of bulks materials, a nice review can be found in [86]. However, the use of TDTR with a patterned transducer remains challenging as the interpretation of the signal from visible wavelength probes is sensitive to hot electron excitation dynamics, material density dynamics, and surface deformation changes, as well as strongly dependent on the modeling of interface transport between the transducer and substrate. Distinguishing between different contributions to the signal is extremely complex and requires many assumptions. Our approach overcomes these limitations by probing nanoscale heat dissipation away from nanoscale heat sources using coherent extreme ultraviolet (EUV) beams from tabletop high harmonic generation (HHG) as laid out in chapter 2 [87, 5, 6].

The different excitation geometries make it extremely challenging to compare the experimental results. In particular, transient grating (TG) experiments on thin films and pattern transducers on a bulk substrate measure different "kinds" of transport. In TG experiments on thin films, the thermal decay of the system corresponds to heat being transported from well-defined excited regions to well defined not excited regions. It measures how fast the film thermalizes (and the transport is 1D). In a pattern transducer experiment, the thermal decay corresponds to the heat dissipation away from the sources, regardless of where it goes (and the transport is 3-D) as illustrated in Fig. 3.4d. Comparison between constrained heat sources and other types of experiments are even more challenging to compare. Recently, the suppression function formalism has been proposed and used in multiple experiments as a pathway to be able to compare different types of experiments.

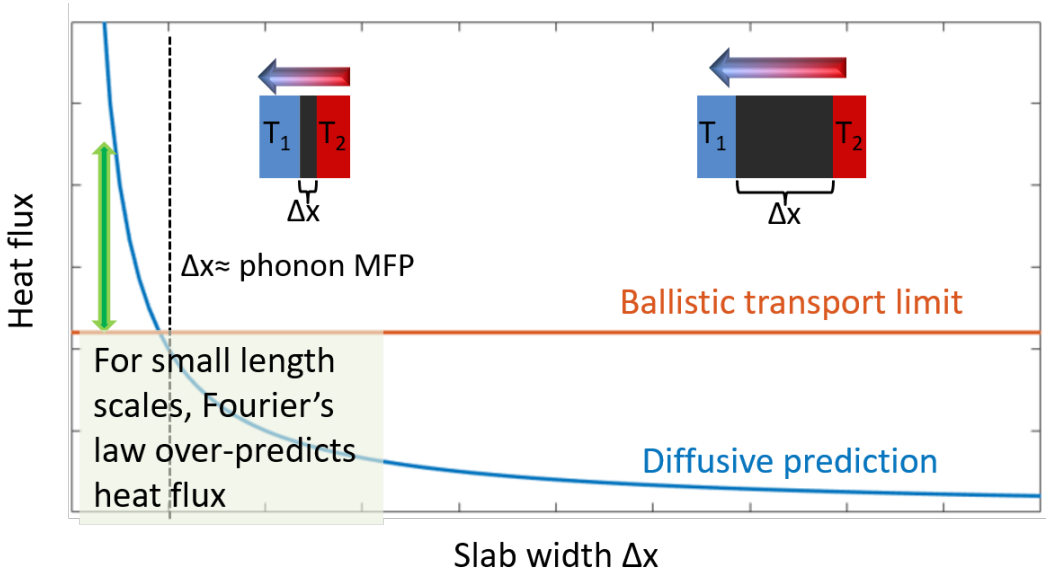

Figure 3.5: **Limit of the diffusive model** When analyzing for heat flux across a slab of material between a hot and a cold area as a function of the slab's width, it is quickly found that the heat equation (blue curve) is only accurate in the regime where the width of the slab is much larger than the MFP of heat carriers in the material. When the width is smaller than the MFP of heat carriers, the heat equation over-predicts the heat flux across the slab, which converges to the ballistic limit (orange curve) when the width becomes much smaller than the MFP of heat carriers.

The suppression function formalism is a very simple idea, where the thermal conductivity of a bulk material is given by Eq. 3.23, but that in the presence of a nanoscale geometry, the contribution to the thermal conductivity for a particular phonon mode i will be reduced by a factor $S(\lambda_i, geometry)$. The shape of the suppression function S depends on the experimental geometry, but the end result can be then compared between experiments. There is not always of way of analytically derive the suppression function for each particular geometry. There is an analytical form for the suppression function to the in-plane thermal conductivity due to the thickness of a thin film [88], as well as for the observations of nanoscale thermal transport in thin films due to a transient grating excitation [89]. There is so far no analytical form for the suppression function for 1D and 2D confined heat sources (nanostructured transducers) on a substrate, leading to a few numerical derivation based on strong assumptions [83, 84] and empirical approximations based on experimental results [5]. This idea will be further explored in section 3.6.

3.3 Sample preparation and characterization

As described in chapter 2, our experiments rely on nanostructured transducers being fabricated on top of different samples of interest. We probe heat dissipation away from arrays of nickel nanolines with different separations, and linewidths ($L = 20nm$ to $L = 1000nm$) and substrates (silicon, sapphire, and fused silica). Three series of arrays are studied: one where the spacing is maintained at four times the linewidth (25% duty cycle) and two where the period was kept constant (at $P = 400nm$ and one at $P = 1500nm$) and various linewidths were fabricated. The sample substrates where purchased at a commercial substrate supplier and the nanofabrication was performed at LBNL by Dr. Erik Anderson and Dr. Weilun Chao. The nanofabrication was done using ebeam lithography and liftoff and result in very successful gratings, as shown in Fig. 3.6.

The materials we chose for our experiment are crystalline silicon and sapphire and an amorphous glass, fused silica. Although applying the phonon model to amorphous materials is a rough approximation that is being revisited [90, 91, 92, 93] , It is a decent approximation for our intent and purposes for fused silica. In this picture, an amorphous material has a very narrow phonon

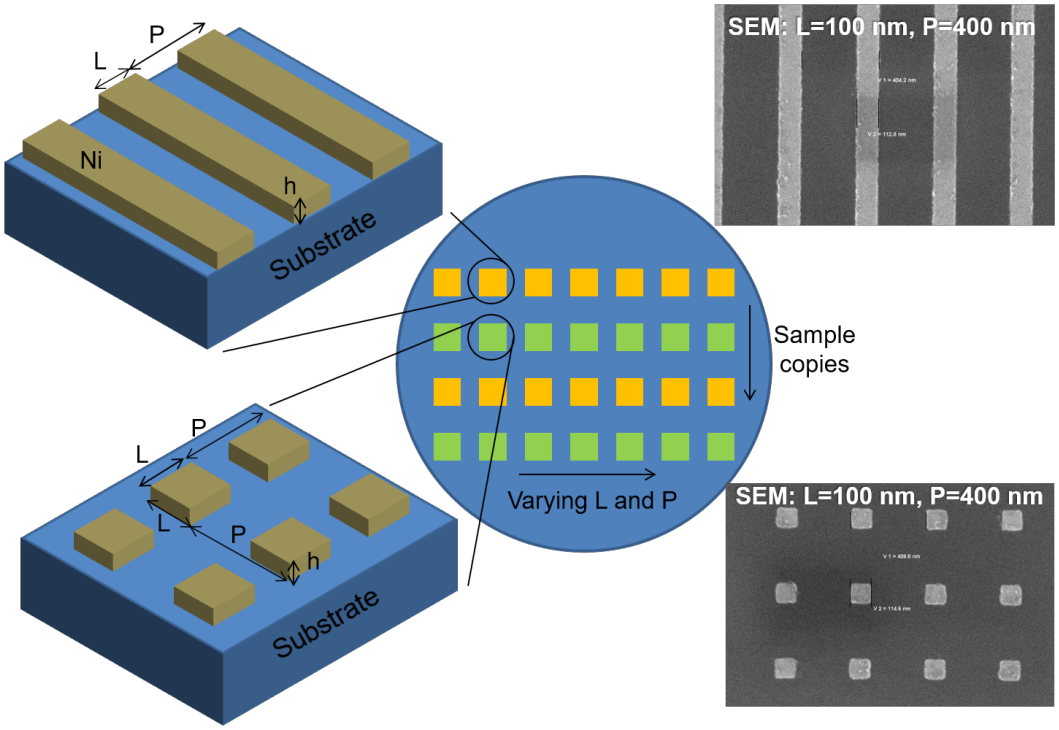

Figure 3.6: **Sample geometries for nanoscale thermal transport studies** Schematic representation of 1-D and 2-D gratings and SEM pictures obtained after nanofabrication. |

MFP spectrum, with most contributions to the thermal conductivity coming from phonons with MFPs ¡10nm (short MFPs). For this reason, we don't expect to see any non-diffusive dynamics in our experiment when probing fused silica. This choice also has the advantage of having been probed in the past in our group [94].

Silicon is an obvious choice as it hadn't been probed with EUV nanometrology before and has been shown to have very unique phonon spectrum properties. Its very large thermal conductivity ($k = 149\frac{W}{mK}$)) is the consequence of a very wide MFP spectrum as shown on Fig. 3.3. Based on most recent theoretical calculations [95], phonons with very long MFP (¿$1\mu m$) contribute more than 50% of the thermal conductivity. Therefore, we expect to observe non-diffusive dynamics starting at heat sources sizes on the order of $\approx 1\mu m$. Furthermore, because of the wide MFP spectrum it is known that the grey-MFP approximation fails at describing silicon [5]. Sapphire on the other hand has a moderate thermal conductivity ($k = 42\frac{W}{mK}$), and a fairly compact MFP spectrum which makes the grey-MFP approximation possible. We expect to see non-diffusive dynamics when heat source size is on the order of $\approx 300 - 500nm$.

The geometry of the samples is an important part of our data analysis. Each grating was characterized using atomic force microscopy (AFM) and surface electron microscopy (SEM) techniques. SEM was used to extract the average period and linewidth of a particular grating, while AFM was used to confirm those values and extract the average height for each grating. The average was the result of measuring several nanolines at different sections of gratings and doses, and averaging the obtained results. We also perform AFM measurements before and after the experiment, to determine a possible damage of the sample during the measurement.

3.4 Data analysis

The data was taken following the description of our experimental setup and technique in chapter 2, and the time-dependent traces are consolidated following the procedure described in section 2.3.1. Each time-dependent trace represents thousands of camera acquisitions at hundreds of different time delays for an specific sample geometry. When analyzing the thermal transport

dynamics in these samples we focus on the thermal decay present in our data, as it is highlighted in Fig. 2.10.

Even though the cooling dynamics in many of our samples are non-diffusive, there is no real solid alternative to describe the dynamics as of yet. In order to inform theory efforts in this direction, we decided to quantify the deviation from the diffusive prediction as a function of sample geometry. This is why we used effective diffusive theory to analyze our data.

3.4.1 The effective diffusive theory approach

Effective theories approach a problem from an established model that describes a type of phenomena, and then tweaks a parameter (making it the effective parameter) to describe a similar set of phenomena. This allows for a comparison between the established model and the observed novel dynamics.

When analyzing our experimental data, we use an effective approach that starts with the macroscopic heat equation for thermal transport in a continuum mechanics system as described in chapter 2, and we use the thermal boundary resistivity (r_{TBR}) between the nanostructures and the substrates as the effective parameter to describe the experimental dynamics. We chose to work with this parameter as it can be directly related to the heat flux that flows away from the nanostructures, and also because it inherently localized at the vicinity of the nanostructures. We expect the size of the heat sources to create non-diffusive dynamics in the nature of the heat flow away from them, and the impact of the size of the heat source will be localized in the vicinity of the heat source. When analyzing our data, we expect to see a fabrication-dependent r_{TBR} (that depends on the fabrication procedure, material properties and interface quality) constant as a function of heat source size. We also look for a correction to r_{TBR}: r_{corr} when non-diffusive dynamics create a deviation from the diffusive model prediction. Therefore, when fitting our data, we extract a value for the effective parameter $r_{eff} = r_{TBR} + r_{corr}$ that generates the simulated time-dependent trace that most closely replicates the experimental result. This allows to:

- Quantify the deviation from the bulk model prediction of the observed dynamics for a particular value of L, P, h and substrate.

- Have a framework to compare the dynamics as a function of L, P, h and substrate.

I modeled our systems based on the geometries extracted from AFM and SEM sample characterization using the commercial software COMSOL Multiphysics, as described in chapter 2. I simulated the thermal and mechanical responses of the samples under different values of r_{eff} covering a very wide range of values for r_{eff}: from $1 \times 10^{-9} \frac{m^2 K}{W}$ to sometimes $12 \times 10^{-9} \frac{m^2 K}{W}$ by steps of $5 \times 10^{-9} \frac{m^2 K}{W}$. An example of the resulting simulated time-dependent experimental data is presented in Fig. 3.7 and an example of using the two-temperature model in the quasi-static approximation is shown in Fig. 3.11.

3.4.2 Data flow and error estimation

Firstly, we make use of our simulated curves to directly find a best fit to the experimental results. This would have an intrinsic error bar equal to the simulated step in thermal boundary resistivity, which is $5 \times 10^{-10} \frac{m^2 K}{W}$. A better results can be achieved by first fitting a double exponential through the simulated curves $diff_simulated(r_{TBR}, t) = a(r)e^{b(r)\cdot t} + c(r)e^{d(r)\cdot t}$. This is equivalent to have an interpolation between the simulated curves, which allows to have a lower step in r_{eff}.. An example of the result of the parametrization step is shown in Fig. 3.8. This small error bar could also be achieved by simulating more traces at a smaller step for r_{eff}, but the parametrization turns out to be very successful and much cheaper computationally. Two exponential terms are, in most cases, enough to fit a wide range of r_{eff} with r-square values of 1 (up to 10^{-4}), but for very large values of L and for very slow thermal decays (such as on fused silica substrates), three or sometimes four exponential terms are needed to achieve the same success in fitting the simulated results. One must be careful to not attach much physical meaning to the amplitude and decay constants of the fits, this procedure is only meant to represent the simulated results, not to interpret it. The values of the coefficients are fit with a polynomial function as

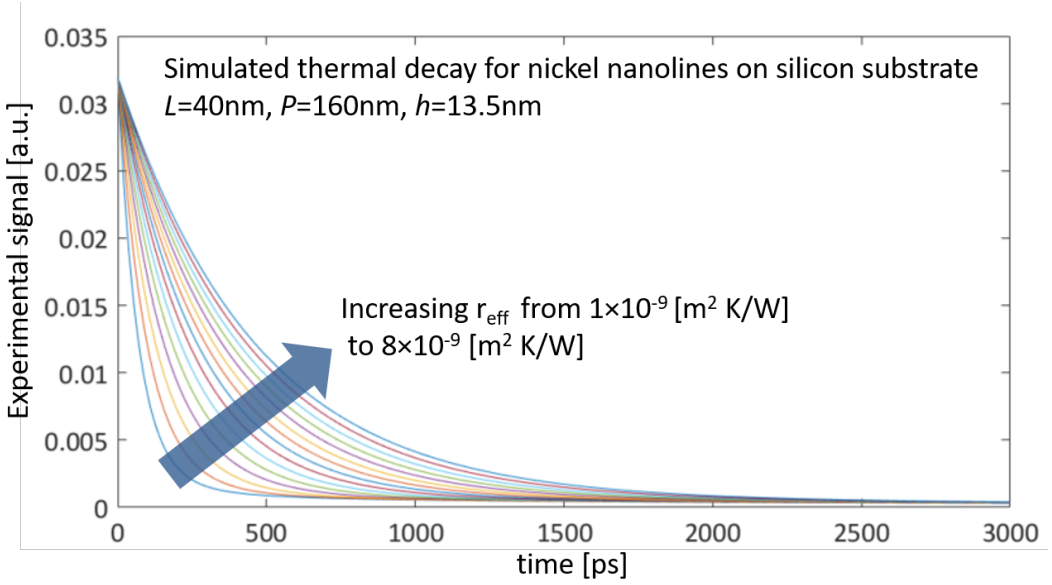

Figure 3.7: **Change in simulated experimental traces as function of the effective parameter** Simulated experimental time-dependent traces using the linear approximation is shown as a function of the effective parameter r_{eff}

a function of r_{eff}, which allows for a very compact representation of the simulated results for a particular geometry and substrate. We do this procedure for all different values of substrates, L,P, and h.

Equipped with a compact form of the simulation results $sim(r_{eff}, t)$, we use a standard least square fit algorithm to fit the thermal decay from experimental traces to the simulated traces. We expect least square fit to give an accurate description to the thermal decay as the acoustic oscillations should be roughly symmetric around the thermal decay. The symmetric argument is a good approximation to handle the acoustic wave oscillations. An example of a successful fit is shown in Fig. 3.12.

The fitting procedure has three parameters besides the effective thermal resistivity r_{eff}. These three relate to experimental noise and are shown in Fig. 3.11. These parameters allow us to quantify and propagate our experimental error into the data analysis. The first one is a temporal (horizontal) offset ΔH to account for the fact that our experimental signal had a finite time step and our time error on "time 0" is equal to a time step of the data. The second one is a signal (vertical) offset ΔV that is kept at under a fraction of the amplitude of our noise level on data points before time 0. In more recent fits we have limited it to two times the variance of the noise level, which takes into account the number of data points before time 0. Finally, an overall normalization coefficient A to the fit, that would account for the fact that our simulations do not capture inertial behavior of the samples, and therefore have a different initial amplitude as our experimental traces. The ideal allowed ranges for A for nickel nanolines on fused silica substrate are summarized in Fig. 3.9 and Fig. 3.10.

The actual ranges have to be relaxed and adjusted to account for the noise levels of each scan. We perform a standard least square fit for the permitted values of these three fitting parameters space and r_{eff} with the function $A \cdot sim(r_{eff}, t + \Delta H) + \Delta V$. Different combinations of the fitting parameters will yield a different r_{eff} value that best describes the data. We have to point out that just running a least squares fitting procedure without bounding the range of the fitting parameters can yield to wrong conclusions, especially for large linewidth structures ($h/L > 10$). The range

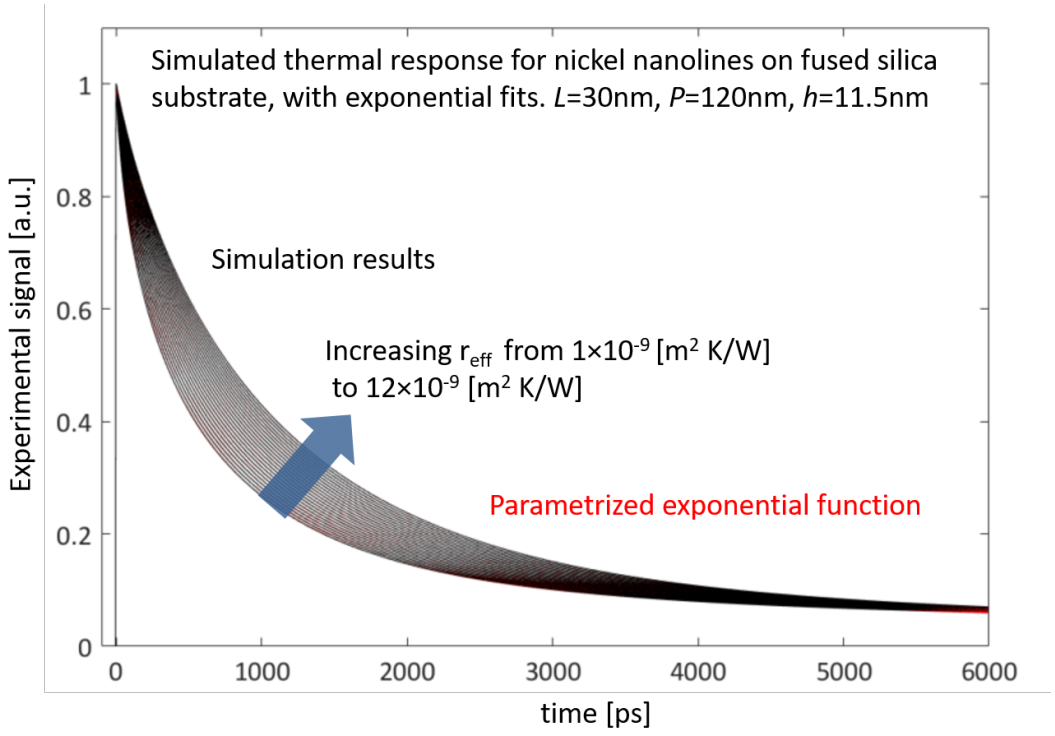

Figure 3.8: **Different values of the effective parameter represented with a sum of decaying exponentials** In black, time-dependent two-temperature model quasi-static simulations for a periodic array of nickel nanolines on fused silica substrate. Different values of r_eff result in different time decays. In red, the exponential function fits to the decay. The fits are excellent, therefore aligning with the simulation curves. |

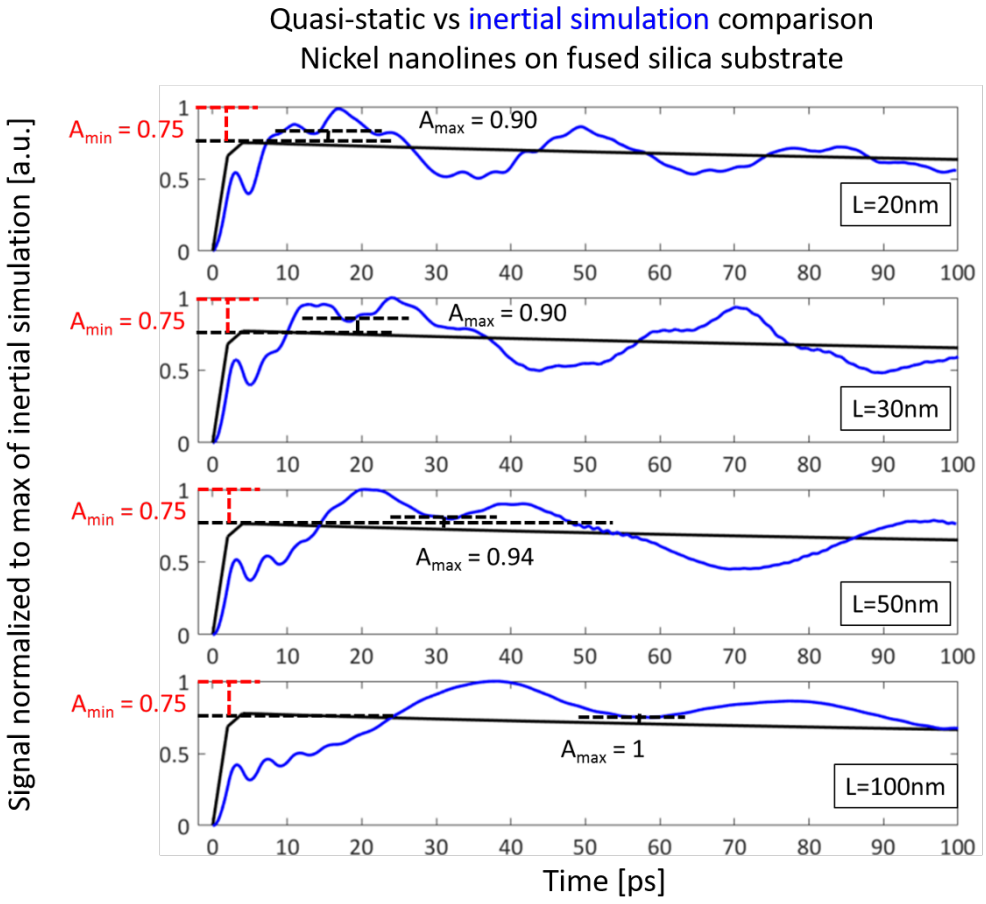

Figure 3.9: **Determining the ideal range for the normalization coefficient with FEA results-small linewidth nanolines** Time-dependent traces of the two-temperature model simulations with the full inertial terms (blue) compared with the quasi-static approximation (black) show the maximum of the signal changes as a function of the linewidth of nickel nanolines on top of fused silica substrate.|

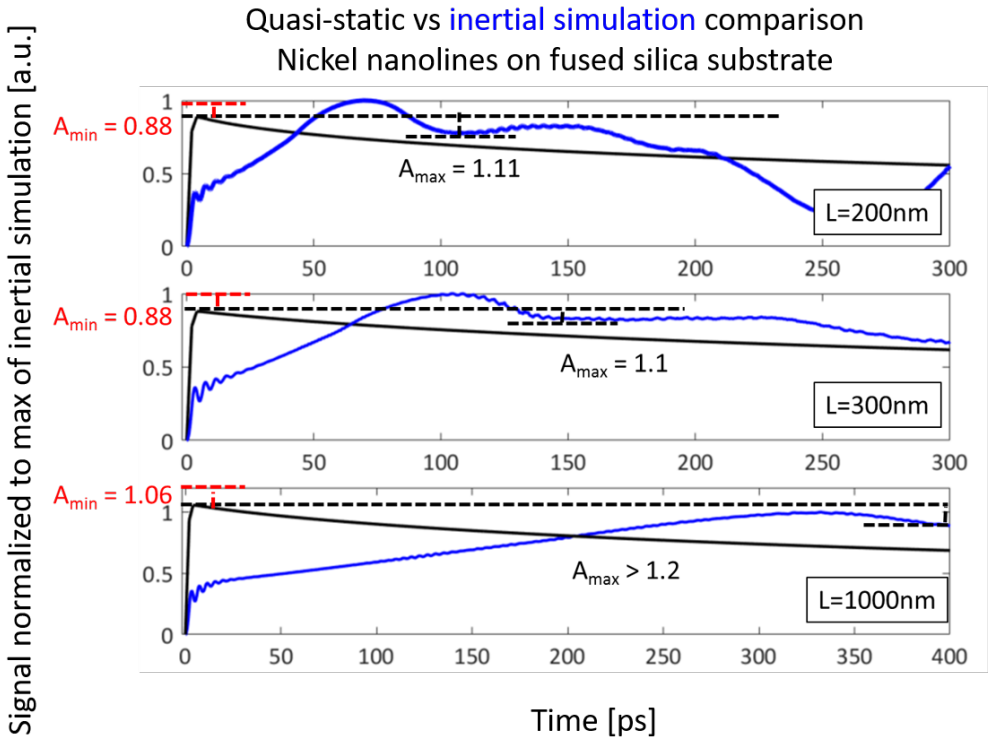

Figure 3.10: **Determining the ideal range for the normalization coefficient with FEA results-large linewidth nanolines** Time-dependent traces of the two-temperature model simulations with the full inertial terms (blue) compared with the quasi-static approximation (black) show the maximum of the signal changes as a function of the linewidth of nickel nanolines on top of fused silica substrate.|

the best fit r_{eff} values gives us the error bar for that particular data trace, which is most likely an overestimation of the error. The results from several scans are then averaged together to obtain the final result and error bars.

3.5 Experimental results

In this section, I present the results obtained using coherent EUV nanometrology to study nanoscale thermal transport on several samples. I first present the results obtained by probing the heat dissipation from 1D confined heat sources on sapphire and silicon substrates that had a constant duty cycle (25%). These results lead to the uncovering of a new regime of thermal transport at the nanoscale, where heat sources seem to cool down faster when close together than if farther apart. I then present the experimental results on the heat dissipation of 1D confined heat sources on silicon, fused silica and sapphire substrates that had a variety of duty cycle gratings. These results directly verified the prediction made based on the constant duty cycle samples, and also allowed us to have more information on the properties of the different nanoscale thermal transport regimes. I also present the results of probing heat dissipation away from 2D confined heat sources on sapphire substrate and how the three regimes of nanoscale thermal transport observed in the study of 1D confined heat sources are also present in 2D confined geometries.

3.5.1 Uncovering the collectively-diffusive regime of nanoscale thermal transport

For this work, published in [5], the nickel nanolines gratings with an average height of $13.5nm$, were fabricated at LBNL by Erik Anderson on a silicon and a sapphire crystalline substrates. The data analysis was performed many times successfully (an example of some fits are shown in Fig. 3.12), and the results are plotted in Fig. 3.13. For large linewidths on both sapphire and silicon substrates, the effective resistivity converges toward a constant value the intrinsic thermal boundary resistivity that exists between two materials and depends on the fabrication procedure. As the linewidth is reduced, the r_{eff} rises as thermal transport turns into the quasi-ballistic regime in both substrates. In this regime, the contribution to the thermal transport by

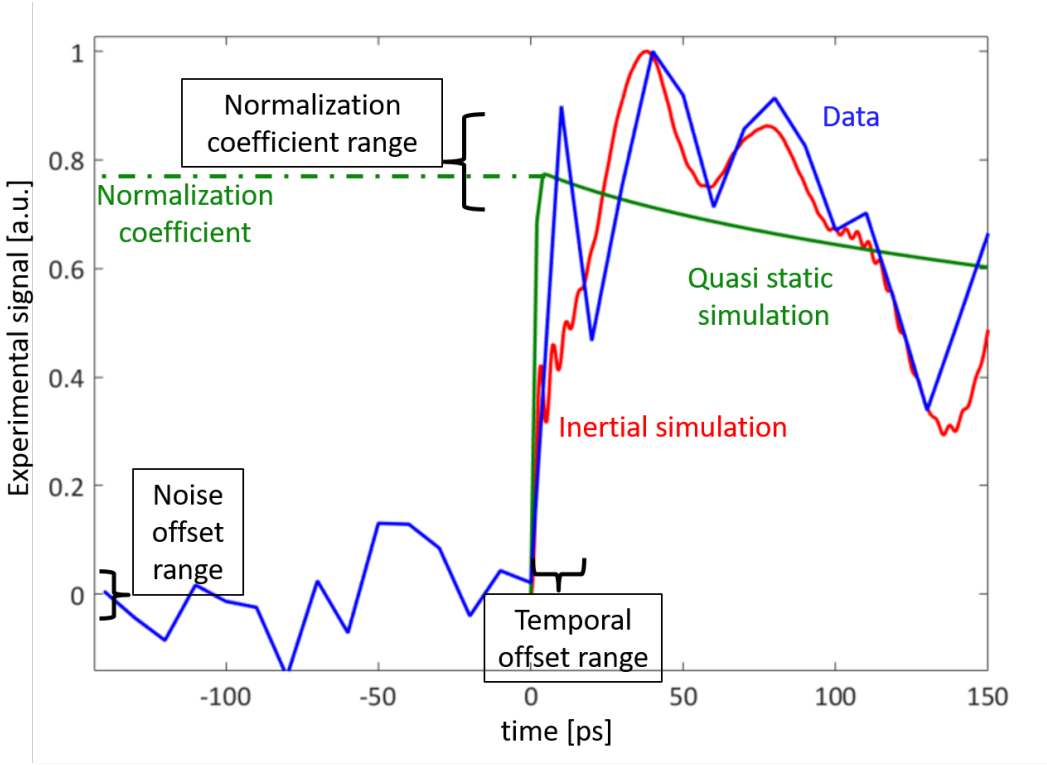

Figure 3.11: **Fitting parameters for nanoscale thermal transport studies** An experimental data trace (blue) is compared to a two-temperature model simulation with the full inertial terms (red) and a quasi-static approximation simulation (green) with the same value of r_{eff}. The different parameters of fitting the quasi-static simulation to the data trace are shown (black boxes) as well as their ranges (black brackets) |

phonon modes with long MFPs (compared to the heat source size) is reduced with respect to the diffusive model. The heat sources are essentially isolated, as both the phonon MFPs and the thermal penetration depth (the distance heat travels a time t in a material with thermal diffusivity α_d according to the diffusive model $l_{thermal} = \sqrt{t\alpha_d}$) are smaller than the distance between the sources set by P. The quasi-ballistic regime results of this work are consistent with previous work citeminnich2011thermal,siemens2009quasi. This regime can be successfully modeled using a grey MFP approximation, where the correction term to the thermal boundary resistivity is proportional to $\frac{\lambda_{grey}}{(L/2)}$ [45]; this model's prediction is plotted in dotted-red in Fig. 3.13.

However, as the linewidth (and period) shrinks further, Fig. 3.13 shows that the effective resistivity starts to decrease rather than continuing to increase. As we are studying constant grating duty cycle of period 4L samples, small linewidths directly imply small separation between neighboring heat sources. Thus, for sufficient small linewidths the separation becomes comparable to dominant phonon MFPs. For silicon, this peak in r_{eff} is shifted toward longer linewidths/periods compared to sapphire because the phonon MFP distribution in silicon peaks at longer MFPs than in sapphire. As illustrated in Fig. 3.14, in this new collectively-diffusive regime, longer-MFP phonons from neighboring heat sources seem to be able to interact with each other (scatter in the same regions) as they would if they originated from a single, large heat source, leading to diffusive-like heat dissipation in certain regions and decreasing the effective resistivity. The quasi-ballistic model for isolated heat sources clearly fails to capture this experimental observation, and a new model for r_{corr} is required to account for the transition to this new collectively-diffusive regime.

Before introducing the model that successfully describe the observed dynamics, it is useful to take a step back and take a look back at previous work. Models by Chen [81] and Siemens *et al.* [45] derive the origin of deviations from diffusive behavior of nanoscale heat source by comparing the radiative and diffusive contributions to the heat flux. And derivations of the approximate constriction resistance derived by Wexler [96] and Prasher [97] relate to that.

The periodic nanolines samples used in this work, as introduced in section 2.3.2.2, can be fully modeled with a 2D unit cell of width P with periodic boundary conditions in the horizon-

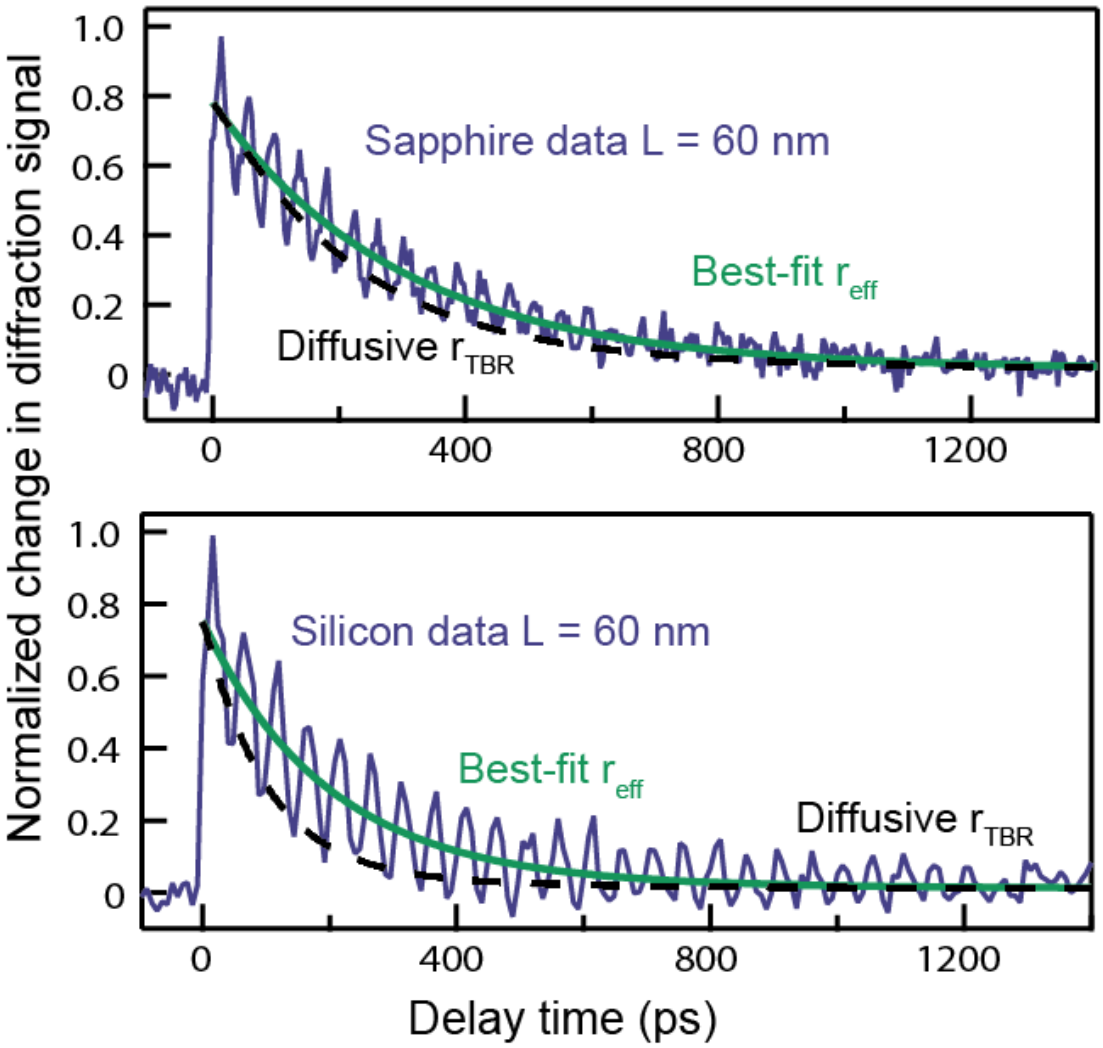

Figure 3.12: **Results on sapphire and silicon substrate with constant duty cycle gratings** Dynamic diffraction from 60nm-wide nickel lines on sapphire (top) and silicon (bottom) display a sudden rise due to impulsive thermal expansion following laser heating, a long decay due to thermal relaxation and oscillations due to surface acoustic waves. Dashed black lines plot the diffusive prediction, which significantly underestimates the thermal decay time. Green lines plot the decay using a best-fit to the effective thermal boundary resistivity. | [5]

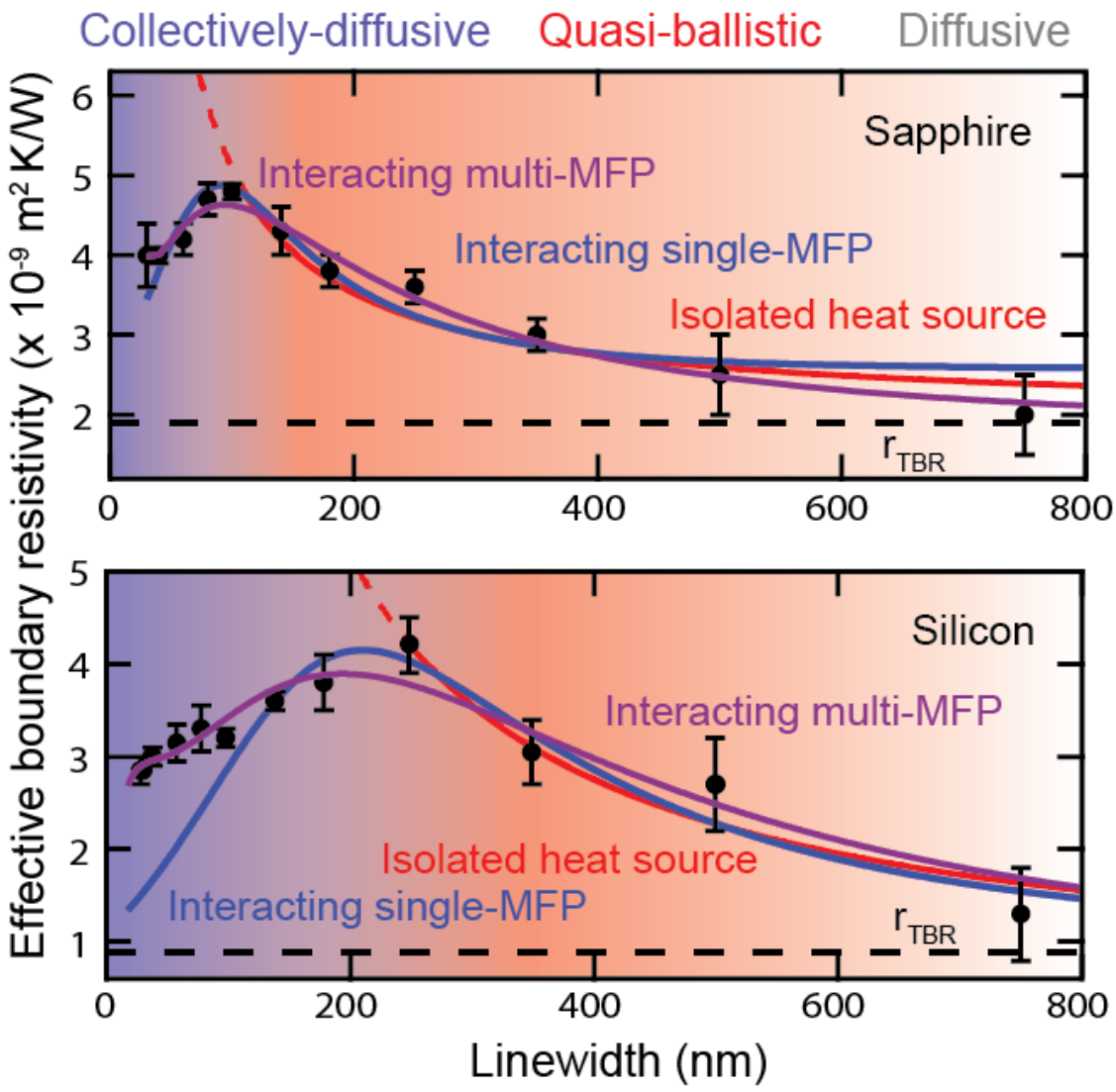

Figure 3.13: **Results on sapphire and silicon substrate with constant duty cycle gratings** Extracted effective resistivities for each linewidth L on both substrates increase with decreasing linewidth until the periods (equal to 4L) are comparable to the average phonon MFP. For smaller periods (spacing), the effective resistivity decreases and approaches the diffusive limit (black dashed line). The error bars represent the standard deviation among multiple data sets for the same linewidth samples. Dotted red lines: predictions for isolated heat sources based on the grey model. Solid blue lines: grey model including the onset of the collectively-diffusive regime. Solid purple lines: more complete model that includes contributions from multiple phonon MFPs. | [5]

tal direction. In order to study the heat flux away from this sample, Siemens et al.[45] defines two concentric circles (that represented cylinders when considering the third dimension across the nanoline's length): one of radius $L/2$, one of radius $P/2$, both centered at the center of the nanoline-substrate interface. Transport between the cylinders at the ballistic limit is just phonon radiation with heat flux $q_{ballistic}$, as shown by [81]. Working in the grey approximation:

$$q_{ballistic} = \frac{C_V v}{4}\Delta T \tag{3.24}$$

where C_V is the volumetric heat capacity, v is the group velocity and ΔT represents the temperature difference between the two cylinders [97]. The resistivity associated with this heat flux component is given by $r_B = \Delta T/q_{ballistic} = 4/(C_V v)$. Given that the thermal conductivity k_{bulk} can be approximated by $\frac{1}{3}C_V v\lambda_{grey}$, we can write:

$$r_{callistic} = \frac{4}{3}\frac{\lambda_{grey}}{k_{bulk}} \ . \tag{3.25}$$

In the diffusive limit, the heat flux between the cylinders is just given by the Fourier equation:

$$q_{diffusive} = \frac{k_{bulk}\Delta T}{\ln(P/L)L/2} \tag{3.26}$$

so that

$$r_{diffusive} = \frac{\ln(P/L)L/2}{k_{bulk}} \ . \tag{3.27}$$

Taking the ratio between both we then encounter the expected ratio:

$$r_{ballistic}/r_{diffusive} = \frac{4}{3\ln(P/L)}\frac{\lambda_{grey}}{L/2}. \tag{3.28}$$

in this particular approximation, the total resistivity of the geometry is given by the sum of the two terms, ballistic and diffusive. However, in most experiments either a single effective resistivity or a single conductivity is extracted from a particular geometry, therefore we need to relate these quantities to the one extracted from experiments.

$$\frac{\ln(P/L)L/2}{k_{bulk}} + 4\lambda_{grey}/3k_{bulk} \equiv \frac{\ln(P/L)L/2}{k_{nano}} \ . \tag{3.29}$$

Or, in the case of a resistivity being measured:

$$r_{Corr} = \frac{d}{k_{nano}} - \frac{d}{k_{bulk}} = \frac{4\lambda_{grey} d}{3k_{bulk}(L/2)\ln(P/L)} \tag{3.30}$$

Where A is a geometrical constant with units of distance, k_{nano} is the measured nanoscale thermal conductivity and k_{bulk} is the macroscopic thermal conductivity. This constant is related to the size of the region where ballistic effects are important should be determined only by the phonon MFP distribution, it should have no dependence on L or P. Thus the proportionality to $\lambda/(L/2)$ is maintained and the finite region where the conductivity change should apply is built in.

This model has a few problems, most importantly, it has wrong physical limits: it diverges for the case where $P = L$ instead of returning simply to a diffusive model. It is certainly a useful model to get an intuition, but it is definitely not a complete model. Moreover, it can only apply to isolated cases.

3.5.2 Interacting heat sources model

In order to build a model that includes both isolated as well as close packed heat sources, we used the concept of a phonon conductivity suppression function, $S(L, P, \lambda_i)$, as described in section 3.1. This model relies on two assumptions. First, the central ideal of this model is based on the hypothesis that if the size of the heat sources impacts the heat dissipation efficiency when the length scales are on the order of the MFP, the spacing between the heat sources will also affect the heat dissipation efficiency, but in an opposite way. The second assumption consist on the idea that if the suppression function has a certain effect on the thermal conductivity as a function of linewidth L, it will have the exact opposite effect as a function of period P. The advantage of this approximation is that it will create the right limits when $L = P$, i.e. a thin film whose dynamics are fully described by the diffusive model. However, the suppression function approach operates in conductivity space, and we have used an r_{corr} to describe our data. Both quantities are related. We first start with the discrete version of *knano*:

$$k_{nano} = \sum_i k(\lambda_i) S(L, P, \lambda_i), \tag{3.31}$$

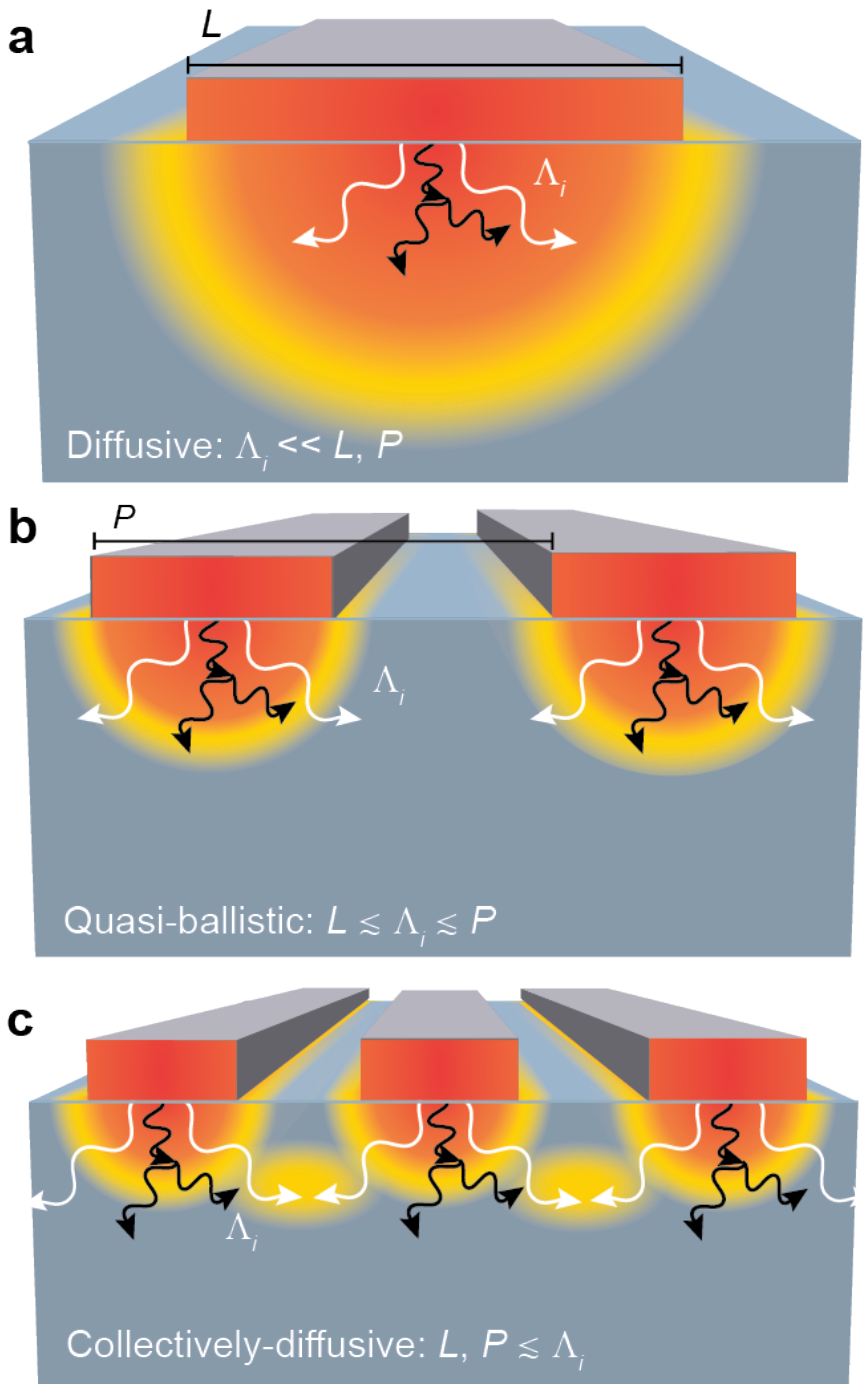

Figure 3.14: **Conceptual illustration of the three regimes of nanoscale thermal transport** Nanoscale heat transport is determined by the interplay between three length scales: the size of the heat sources L, the spacing of the heat sources P, and the MFPs λ_i of heat-carrying phonons. Materials support a broad distribution of MFPs, represented here by short (black) and long (white) MFP phonons. **a**, When all MFPs are much smaller than L, heat dissipation is fully diffusive. **b**, As L shrinks, long-MFP phonons travel ballistically, decreasing the rate of heat dissipation relative to diffusive predictions. Short-MFP phonons remain diffusive. **c**, When both L and P shrink, long-MFP phonons originating from neighboring heat sources interact as they would if they originated from a single, large heat source, enabling more efficient diffusive-like heat transfer. | [5]

We then relate r_{corr} to the change in conductivity represented by this suppression.

$$r_{corr} = A(\frac{1}{k_{nano}} - \frac{1}{k_{bulk}}), \tag{3.32}$$

where A collects geometrical constants, including a length scale (discussed further in section 4.1) and k_{bulk} is the bulk conductivity of the substrate, simply given by $\sum_i k(\lambda_i)$. For a given phonon MFP λ_i, S must approach unity in the diffusive regime when both L and $P$are large and at the limit of a thin film when $L = P$. For the limit of small, $L << \lambda_i$, isolated heat sources when $P >> \lambda_i$, S must reproduce the behavior of isolated heat sources, where the quasi-ballistic model has been successful in the past [45, 98]. To capture these behaviors along with smooth transitions among regimes, the two effects are represented by a special case of the generic family of logistic functions, where the total suppression function is written as:

$$S(L, P, \lambda_i) = tanh(L/2\lambda_i) + [1 - tanh(P/2\lambda_i)]. \tag{3.33}$$

Fig. 3.33 represents the first attempt to include the contribution of heat source spacing and offers a model which is simple enough for fast integration into existing models of heat transfer in nanoscale devices, for example, but complex enough to capture both past and current behavior and make successful predictions. We first use this model to fit our data within the grey-MFP approximation, plotted in grey in Fig. 3.13. Not surprisingly this approach is successful to fit the results on sapphire substrate, but fails to capture the results on a silicon substrate. As I have mentioned previously, silicon has been proven by DFT calculations and other experimental work to have a very wide phonon MFP spectrum, making the grey-MFP approximation a bad approach. The fitting function in the grey approximation is given by:

$$r_{corr,grey}(L, P) = \frac{A}{k_{bulk}}(\frac{1}{S(L, P, \lambda_{grey})} - 1), \tag{3.34}$$

Fitting this interacting model to the r_{eff} data for sapphire, we extract values for the intrinsic r_{TBR} and λ_{grey} which are consistent with previous results [45]: $\lambda_{grey} = 131 \pm 11nm$, $r_{TBR} = 2.58 \pm 0.19 \times 10^{-9} m^2 K/W$. This good agreement with the previous larger-linewidth data and the accurate fit for the full range of our data validate our model as an improved method to account for nanoscale size

effects in heat transport for both quasi-ballistic and collectively-diffusive regimes. Using this model for silicon gives a clearly bad fit, but it is still interesting to check the result:$\lambda_{grey} = 306 \pm 17nm$, which is consistent with previously reported values in the grey-MFP approximation. Luckily, the extension to our model beyond the grey approximation in order to encompass the entire phonon spectrum is straightforward and illustrated in Fig. 3.15:

$$r_{corr}(L,P) = A(\frac{1}{\sum_i k(\lambda_i)S(L,P,\lambda_i)} - \frac{1}{\sum_i k(\lambda_i)}), \tag{3.35}$$

The use of our toy model accounting for a spectrum of phonons is now very successful at fitting our experimental data as well as to extract information about the phonon spectrum as can be seen in Fig. 3.13. This model work in the other direction as well, and can also be used to extract the phonon spectrum of a material as it is discussed in section 3.6.This model has a surprising implication which is valid for both the grey approximation as well as for when the full spectrum is included. Illustrated in Fig. 3.15, our suppression function is similar to a notch filter. When taking the case where L is fixed and small enough L so that a significant portion of the phonon MFP spectrum is suppressed we encounter a surprising prediction: a smaller value of P will suppress less of the phonon MFP spectrum contribution to the thermal conductivity as would a larger one. This translated into the following statement: nanoscale heat sources will cool down faster if place close together than if farther apart This is the opposite than macroscale behavior!

This prediction was the first to make such a statement, later others arrived to similar conclusions that will be discussed in more detail in section 4.1. Although surprising and non-intuitive at first, the possibility of having a predictive model for close packed nanoscale heat sources is too tempting to not try. In order to be a successful milestone the predictions need to be verified, and that is exactly what we set out to do.

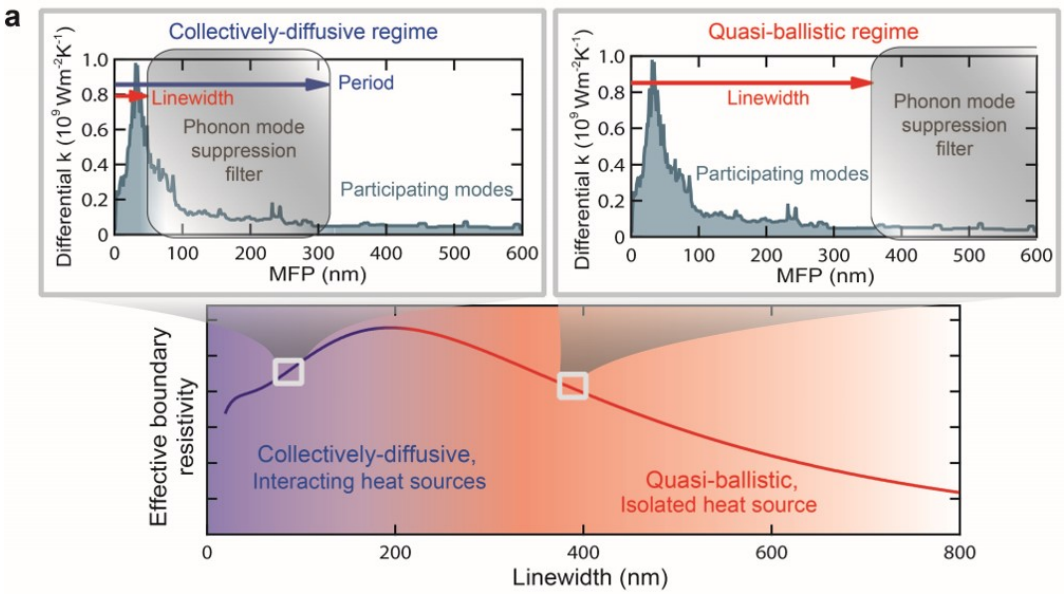

Figure 3.15: **Conceptual illustration of non-isolated heat sources suppression function** Linewidth and period define a suppression filter for phonon mean free path spectra. The observed increase in effective thermal boundary resistivity for small linewidths L is due to the suppression of the contribution to thermal conductivity of phonon modes with MFP larger than L. Decreasing the period P can reactivate modes with MFP larger than P, decreasing the effective resistivity. In the limiting case of a uniformly heated layer, P approaches L and all phonon modes participate in thermal transport. We use as an example the smoothed differential conductivity distribution for silicon (top graphs, green line), calculated from first-principles density functional theory. | [5]

3.5.3 Experimental confirmation of the collectively-diffusive regime in multi spacing heat sources

In order to test our interacting heat source model's predictions, we designed new gratings on three different substrates, silicon, sapphire and fused silica which were fabricated at LBNL by Dr. Weilun Chao [6]. Several grating geometries were common with the old ones (25% duty cycles with $L = 30, 50, 100nm$), others were still 25% duty cycle with different L to fill in the gaps of the previous measurement (25% duty cycle and $L = 1000, 300, 200, 20nm$) as well as two new series of gratings where the period was constant at $P = 400nm$ with linewidths of $L = 20, 30, 50nm$ and $P = 1500nm$ with $L = 100, 200, 300nm$. By comparing the traces of gratings with the same value of L and different values of P, we expected to see evidence (or disproof) or our hypothesis. The raw data for the cooling of 20 and 30nm linewidth nanolines on silicon Fig. 3.16a,b at two different periodicities (one "close-packed" and one "isolated") present clear evidence that heat sources that are widely-spaced $P = 400nm$ cool slower than closely-spaced ones $P = 4L$ on silicon. The raw data for 20 and 30nm linewidth nanolines on fused silica plotted in Fig. 3.16c,d show no difference between the different periodicities, as expected. The sapphire raw traces are sadly not available at the moment, due to unexpected melting issues.

These Raw data results are a direct confirmation of the reality of the collectively-diffusive regime and of the dependence of heat dissipation away from nansocale heat sources on the spacing between the heat sources. This is true regardless of the modeling framework used to analyze the data, which makes it a very solid result. When analyzing the data in the effective resistivity space, we again see the predictions of our model confirmed. The results for silicon are plotted in Fig. 3.17. The extracted and predicted trends of the notch-filter suppression function that is recovered from the data: a monotonic increase in effective resistivity when the period is held constant and the linewidth is reduced, and a significantly lower effective resistivity for nanolines with smaller periodicities.

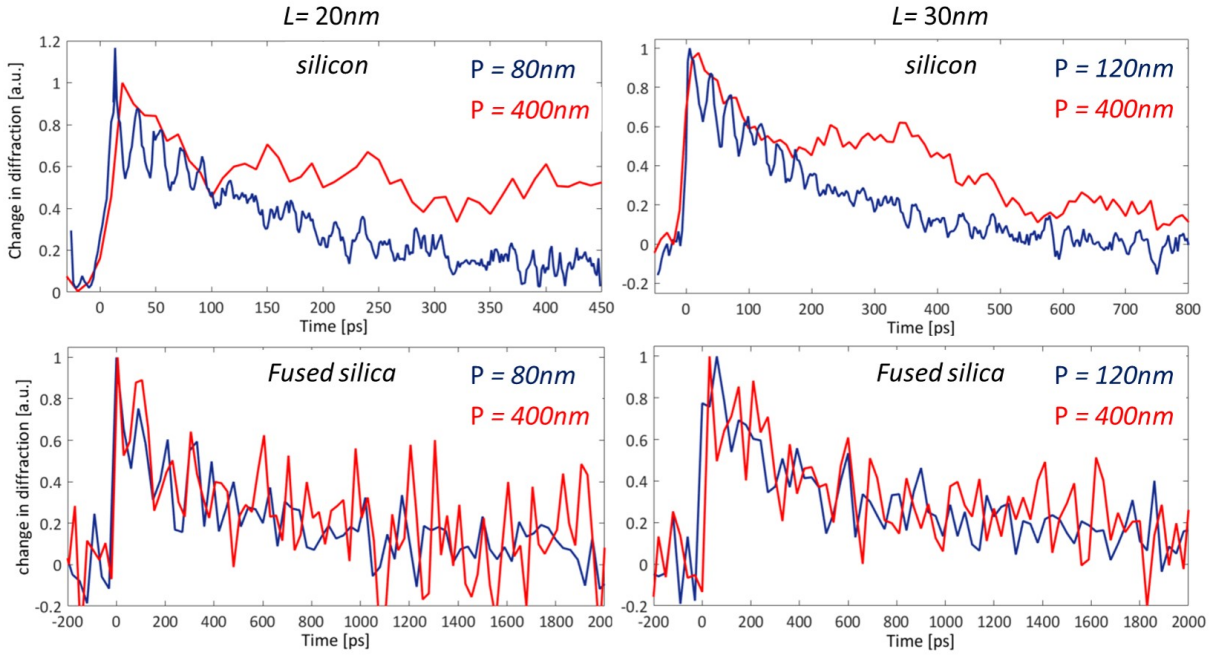

Figure 3.16: **Experimental traces of nanoscale heat sources at different spacings confirm predictions of the collectively diffusive regime** Raw experimental traces of periodic arrays of nickel nanolines on different substrates. In blue, arrays with $P = 4L$, in red $P = 400nm$. The data on silicon for $L = 20nm$ (**a**) and $L = 30nm$ (**b**) shows clearly that nanolines that are closer together (blue) appear to cool down faster than if farther appart (red). he data on fused silica for $L = 20nm$ (**a**) and $L = 30nm$ (**b**) shows clearly that the periodicity has no impact on the temperature decay of the system, as expected. |

The results on a fused-silica substrate are used as a control, as the MFPs of its heat carriers is $< 10nm$ and the phonon modes do not see their contribution to the thermal conductivity reduced by nanoheater geometry (L and P) as shown in Fig. 3.18. The data shows the expected lack of deviation from the diffusive prediction for this material, within fairly large error bars. The error bars for fused silica are not great as our experiment looses sensitivity to the thermal dynamics when the thermal conductivity is low. As shown Fig 3.8, a wide variation in r_{eff} (a variation from 1×10^{-9} to 8×10^{9} is shown on the graph) does not actually change the decay constants significantly. No matter what, a constant hypothesis is supported by the data, which is nice.

These results not only provide a qualitative and quantitative confirmation of the collectively-diffusive predictions, but also important experimental evidence to guide current and future models. However, these results also point out limitations of using an empirical model that is unable to make quantitative predictions without fitting parameters, and highlights the need for more fundamental approaches that solve the Boltzmann transport equation in experimental geometries. This would provide a quantitative method to extract the phonon differential conductivity spectrum from these nanoscale thermal transport measurements.

3.5.4 2D confined heat sources data further confirms new understanding of nanoscale thermal transport

Probing heat dissipation from 2D confined nanoscale heat sources is significantly more difficult than 1D confined ones mainly for one reason: the surface area covered by the nanostructures is considerably reduced. Our experimental signal, as discussed in chapter 2, originates mainly from the large thermal expansion of the nanostructures as their temperature varies. In 2D gratings, a $L/P = 0.25$ ratio corresponds to only 6.25% of the surface being covered by nanostructures, making the signal to noise ratio lower. However, we have been able to successfully measure the $L/P = 0.25$ gratings so far. Measuring lower duty cycles will only be possible once hardware upgrades are done to the experiment (such as a locked-in chopper instead of a shutter to control the pump pulses).

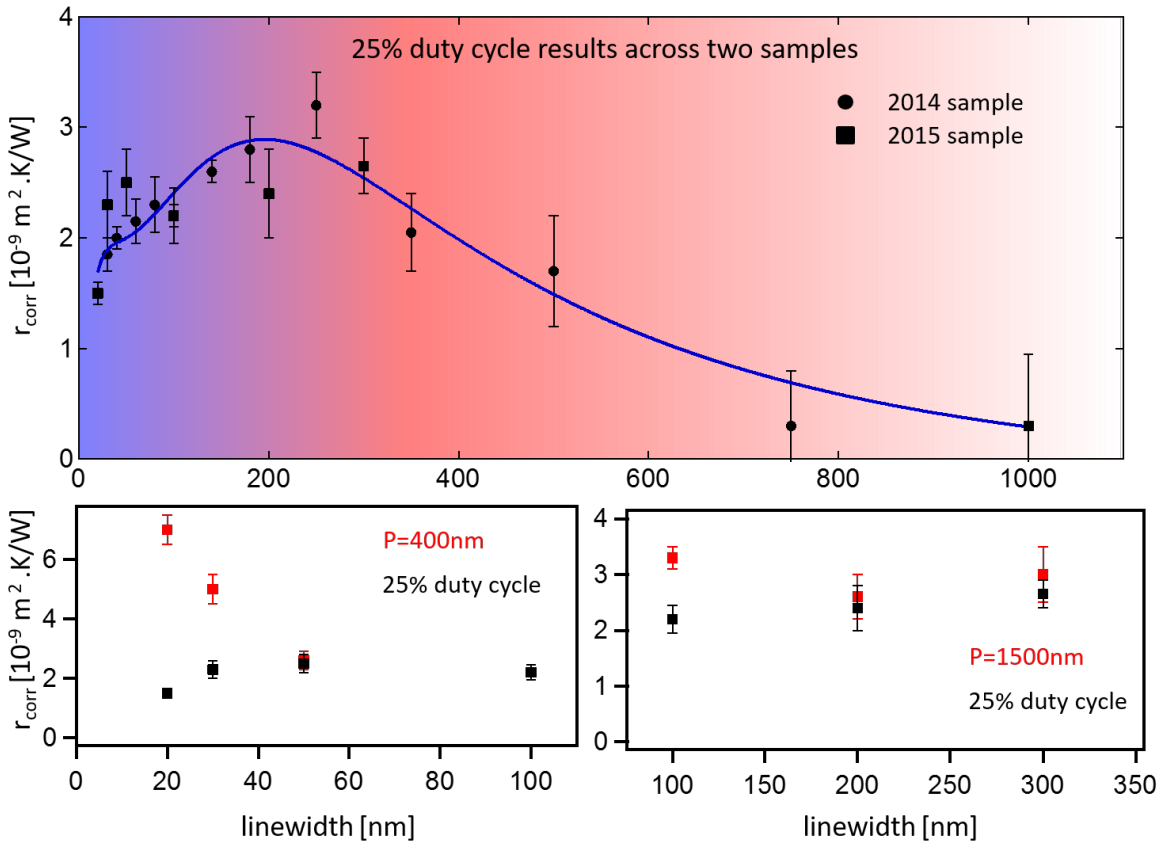

Figure 3.17: **Analyzed data of 1D confined heat sources on silicon confirm predictions of our interacting heat sources model top**. The extraction of r_{corr} for the 25% duty cycle gratings on nickel nanolines on silicon for the 2015 sample (black squares) is compared to the 2014 sample (black circles). The consistency between the data is very high, with the same trends showing in both data sets. **bottom left**. r_{corr} for the 25% duty cycle gratings (black) compared with fixed period $P = 400nm$ gratings (red). The higher value for r_{corr} for the $P = 400nm$ samples confirms the predictions of the collectively-diffusive regime **bottom left**.r_{corr} for the 25% duty cycle gratings (black) compared with fixed period $P = 1500nm$ gratings (red). The higher value for r_{corr} for the $P = 1500nm$ samples confirms the predictions of the collectively-diffusive regime.

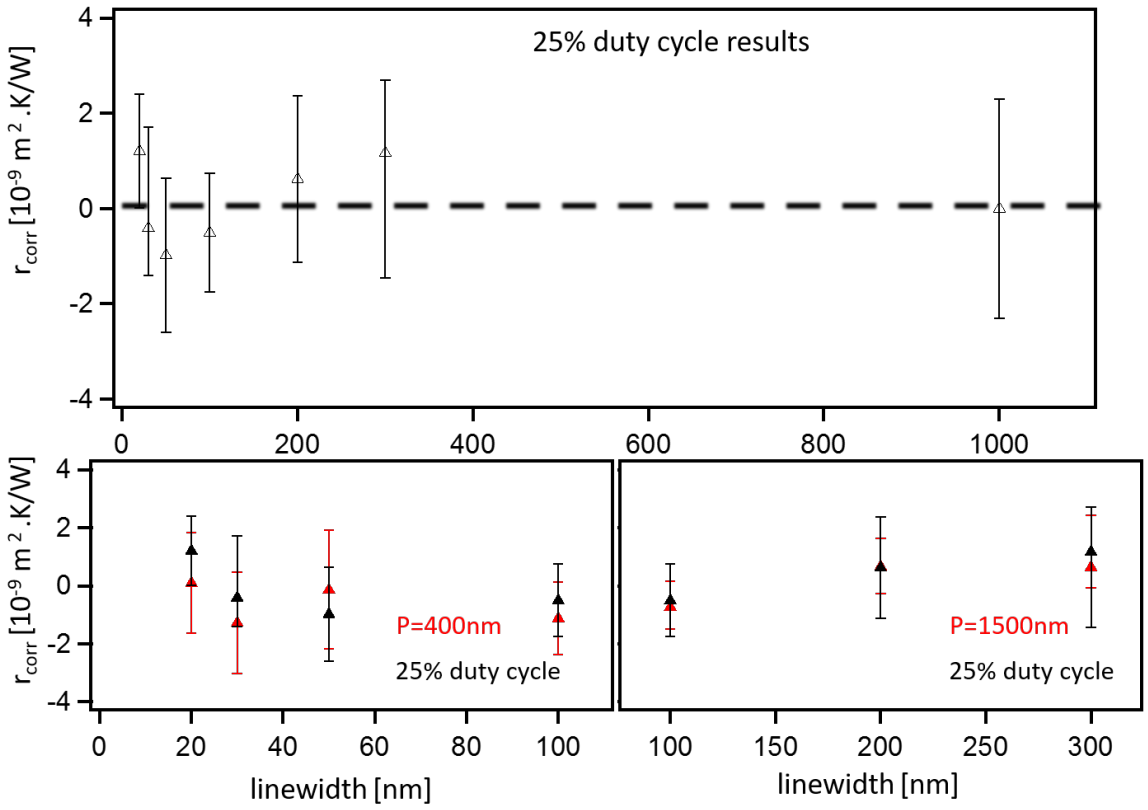

Figure 3.18: **1D confined heat sources on fused silica show little to no deviation from diffusive model prediction top**. The extraction of r_{corr} for the 25% duty cycle gratings on nickel nanolines on fused silica is plotted as a function of linewidth L. As expected, $r_{corr} \approx 0$ as a function of L with no visible trend within error bars, since the phonon MFP in fused silica is $<< 10nm$. **bottom left**. r_{corr} for the 25% duty cycle gratings (black) compared with fixed period $P = 400nm$ gratings (red). there is no impact of the grating periodicity on the heat dissipation efficiency **bottom left**.r_{corr} for the 25% duty cycle gratings (black) compared with fixed period $P = 1500nm$ gratings (red). Again, there is no impact of the grating periodicity on the heat dissipation efficiency

In the RAW traces we can observe that qualitatively the effects present in the 1D confined heat sources are also present in the 2D ones, but in a more pronounced manner. This qualitative look at the data is not very informative, especially without the varying duty cycle samples. But we can attempt to analyze the data in resistivity space

The FEA calculations in 3D require significantly more computing power than the 2D ones, but I successfully was able to run most of the geometries. The results for sapphire are shown in Fig. 3.19. Not surprisingly, the three regimes of thermal transport are present in the results, just as in the 1D confined case, but the magnitude of the changes are different.

Sadly, the values of r_{eff} from 1D and 2D confined heat sources cannot be compared directly, as there are many geometrical factors involved that we are uncertain of. It is however, a work in progress that once finished, will provide an interesting way to probe anisotropic thermal conductivity. It is interesting to see that the magnitude of r_{eff} for 2D confined heat sources is much different than for 1D.

3.6 First steps towards phonon MFP spectroscopy

It is important to point out that after our first experimental results and suppression function were published in 2015, more recent work by other groups (both experimental and theoretical), uses the knowledge that the suppression function in a periodic grating of nanostructured transducer depends on the linewidth of the sources L **and** on the spacing between P them $S(\lambda_i, L, P)$, therefore making the expression for the thermal conductivity:

$$k_{nano} = \frac{1}{3}\int_0^{\omega_{max}} \tau v^2 C_\omega S(\lambda_\omega, L, P) d\omega \tag{3.36}$$

After the development and experimental validation of the new model which captures the transitions from diffusive, to quasi-ballistic, to collectively-diffusive regimes, we can now extend our calculations beyond the simple single-MFP model and use our data to extract the MFP-dependent contributions to thermal conductivity in different materials down to MFPs as small as $14nm$ for the first time. Making use of the data from our 25% duty cycle samples, the contribution to thermal conductivity

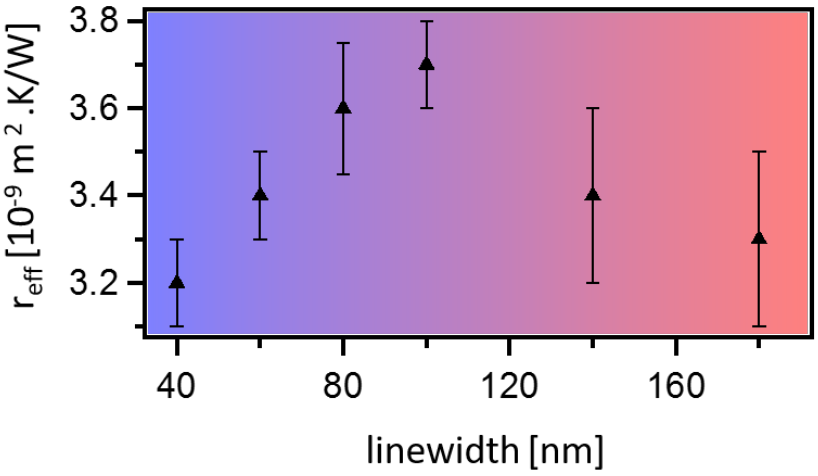

Figure 3.19: **Preliminary results of r_{eff} on 2D confined heat sources on sapphire** Extracted r_{eff} for gratings of nanocubes with $L/P = 4$. Since only L up to $180nm$ has been analyzed, r_{corr} cannot be extracted with confidence, but it will once $L = 500, 750nm$ are analyzed.The visible trend in the data is consistent with the trend present in the 1D confined nanolines, with both the quasi-ballistic and collectively-diffusive regimes present.

of different MFP ranges of phonon modes with a resolution controlled primarily by the number of configurations tested is sampled This is possible because both linewidth L and period P set the location and width of the effective notch filter in the phonon MFP spectrum. Each geometry will suppress different phonon modes of the MFP spectrum in a different way, thus providing higher sensitivity to the MFPs that are suppressed the most. The line that represents the values of the most suppressed MFP as a function of L for a 25% duty cycle geometry are shown in Fig. 3.20.

The larger the resistivity correction needed for a given nano-grating, the stronger the conductivity contribution of phonon modes which were suppressed. In order to extract information about the differential conductivity spectrum, we use the full multi-MFP form of r_{corr}, given by Eq. 3.35.

In order to produce the fits shown in purple in Fig. 3.13, I implemented a fitting algorithm based on Eq. 3.35.

This algorithm retrieves the MFP spectrum by considering the influence of the suppression function given by our model and reproduces the observed values of r_{corr}. This allows us to essentially extract the phonon MFP spectrum of the material in which the heat is dissipating, making this the first technique to be able to extract the differential phonon MFP spectrum of a material.

In the procedure, we proceed to partition the full sum in bins according to the MFP-sensitivity of each grating configuration as illustrated in Fig. 3.20. Then by fitting our set of r_{eff} data as $r_{eff} = r_{TBR} + r_{corr}$ we extract the average $k(\lambda_i)$ of each bin, thus assessing the relative contributions to thermal conductivity of each region of the phonon MFP spectrum plotted in Fig. 3.21. By limiting the number of bins to be no more than half our number of data points, we ensure a conservative, well-conditioned fit, although we note that changing the bin number does not substantially alter the trends we observe.

As shown by the purple curves in Fig. 3.13, for sapphire, this procedure matches the experimentally measured r_{eff} as well as the grey model for interacting heat sources. For silicon, this more complete multiple-MFP interacting model is able to match our experimental measurements of ther-

mal boundary resistivity over diffusive, quasi-ballistic and collectively-diffusive regimes, including the exceptionally slow drop in resistivity for small linewidths below $100nm$.

In this first attempt, published in [5], the number of experimental data points limits the number of regions we can reasonably consider in this first demonstration. However, this approach still offers unprecedented new experimental access to the differential thermal conductivity contributions of phonons with different MFPs and for benchmarking theoretical predictions, including those from first-principles density functional theory (DFT) calculations shown in Fig. 3.3. In particular, our experimental data across all MFP ranges measured in silicon are in very good agreement with our DFT calculations. Differences between the experimental and theoretical spectra in this region may also be exaggerated by our limited set of small-linewidth gratings. Our data are also consistent with observations by others which emphasize significant contributions from long-MFP (¿ 1 m) modes, but the limited number of data points we have for structures much larger than the average phonon MFP results in a relatively large uncertainty in this region. For the purpose of comparison in Fig. 3.3, I normalized the experimental spectra in silicon by assuming the integrated conductivity up to 1 m should match that calculated by DFT.

For sapphire, both calculation and experimental data imply that phonons with MFPs shorter than $1\mu m$ are responsible for $> 95\%$ of the thermal conductivity. The discrepancy below 300 nm between experimental and theoretical curves (apparent in the cumulative distribution) is due to two factors. First, the sharper rise in the DFT cumulative curve arises due to the very strong short-MFP peak in the conductivity spectrum a peak that lies at approximately $5nm$, below the lower bound of our experimental sensitivity ($14nm$) using $30nm$ structures. Thus, the experimental data simply does not include the shortest phonon MFP peak. Second, because of the complex crystal structure of sapphire, the DFT calculations required the use of relatively small interaction-distance cutoffs for determining the harmonic and anharmonic force constants, which may cause a larger error in the predictions than for silicon.

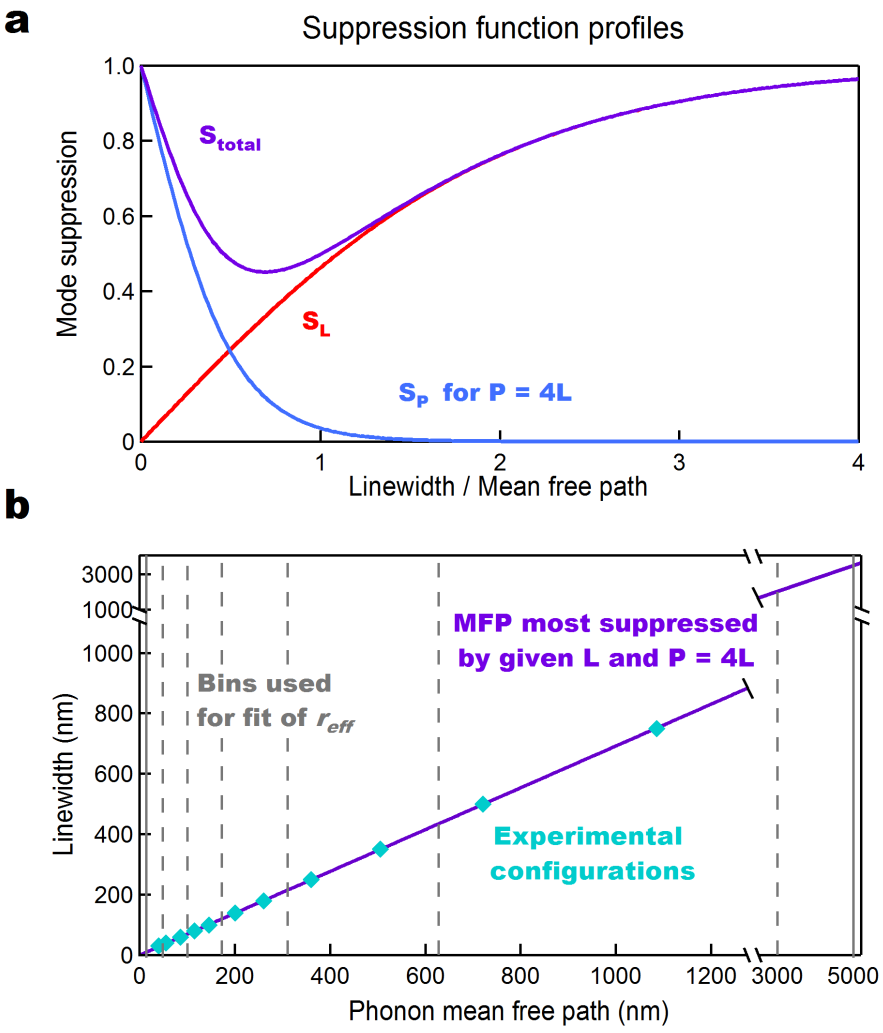

Figure 3.20: **Interacting heat sources model and the predicted sensibility to phonon MFP spectrum of a particular geometry a**, For a phonon mode with a given mean free path, S_L describes the suppression of this modes contribution to thermal conductivity as the linewidth of a heat source decreases. S_p undoes this suppression, and S_{total} represents the total suppression when both small heat source and interaction between heat sources are taken into account. Thus, each configuration for L and P can be related to one most-suppressed MFP (minimum of S_{total}). **b**, We use this information to set the MFP bins used when fitting r_{eff} data in the full interacting multi-MFP model.| Figure adapted from [5]

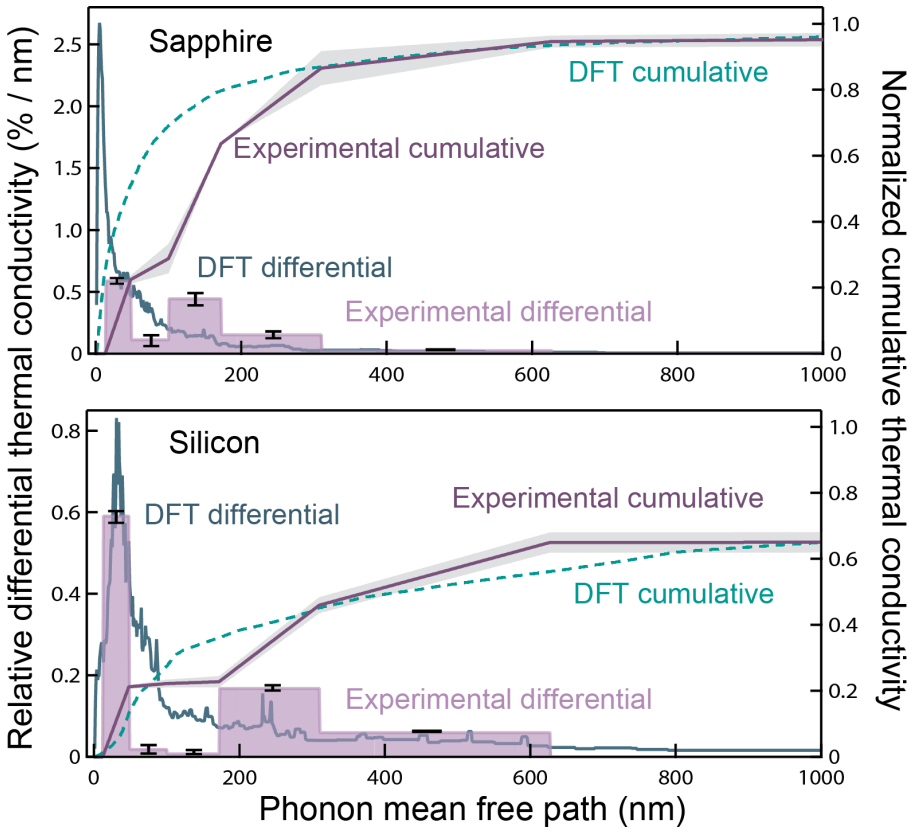

Figure 3.21: **Calculated vs Experimentally extracted MFP spetra for silicon and sapphire substrate** By fitting r_{eff} with multiple bins of phonon modes, the weights $k_{nano}(\lambda_i)$ assigned to those bins give the average relative contribution to the differential thermal conductivity (purple shading). Both differential (distributions) and cumulative (lines) conductivities are normalized to the total bulk conductivity. For sapphire (top panel), our data (solid purple line) and first-principles DFT calculations (dashed green line) indicate there are no significant contributions from long-MFP phonons, so the cumulative curves approach unity at $1\mu m$. For silicon (bottom panel), our data are consistent with large contributions from longer MFPs.| Figure adapted from [5]

This approach is overall very successful. However, efforts are still needed in order to make more useful and insightful predictions, specially by developing a model not based on an effective theory. More on this topic will be discussed in chapter 4.

3.7 Conclusion

Nanoscale thermal transport is a very rich field of research, with still many unknowns and many surprises. The high impact that it has on both technology and fundamental condensed matter physics is a motivation to continue making further progress in our understanding of it. In my dissertation work I have increased our knowledge on nanoscale thermal transport by developing a novel experimental technique to probe nanoscale thermal dynamics as well as a computational and theoretical framework to understand experimental results. In this chapter I have presented the theoretical foundations and work in literature upon which our work builds upon , I present the first evidence and further confirmation of a new regime of nanoscale thermal transport in 1D confined periodic heat sources on silicon, sapphire and fused silica substrate and for 2D confined heat sources on sapphire substrate. I present the theoretical models that I developed and how they present one of the only pathways towards a phonon lifetime spectroscopy.

For future work, probing more 2D confined and 3D confined heat sources will provide true insight into the mechanisms behind the regimes of nanoscale thermal transport. Furthermore, developing an excitation scheme to produce nanoscale heat sources ¡10nm without the need of nanofabrication will be needed, which is why I have started working on an EUV transient grating scheme that will be further discussed in chapter 7.

Chapter 4

Computational approach to nanoscale thermal transport

At the end of chapter 3, I demonstrated a proof of concept for a methodology to extract a fundamental condensed matter material property, the phonon mean free path (MFP) spectrum, from experimental results. However, in order to implement this technique, a more fundamental theoretical foundation is required since the accuracy of the resulting experimental spectrum is entirely dependent on the phenomenological model. More specifically, the necessary step of utilizing an effective diffusive model may not accurately represent the dynamics in the system. Additionally, the suppression function we derived is not based on first-principles even if it serves as a good approximation in this experimental geometry. Finally, as shown in Fig. 3.21, the resolution of this methodology is quite limited not only by the number of different geometries, but also due to the uncertainty in the effective models. In chapter 3, I presented the derivation of an empirical model based on the suppression function approach that not only successfully describes experiments to date, but also contains qualitative predictions that we confirmed experimentally. Even if this model is not based on first principles, it does capture the effect of varying important parameters that influence thermal transport at the nanoscale: the size of heat sources, the distance between heat sources, and the phonon MFP spectrum.

The success of the use of an effective theory motives the search for a more fundamental approach to our experimental results. As presented in chapter 3, when trying to solve dynamics at the nanoscale with an ab-initio approach, computational cost significantly increases. By just looking at the full phonon Boltzmann transport equation (BTE), one realizes the complexity of the

problem: three spatial variables, three momentum variables, time, and a spatially and temporally dependent distribution function. Solving this equation is computationally expensive in simple geometries; but, this does not even include the modeling of interfaces and boundaries, which are still current areas of research [99, 100]. Even in the linear approximation, as described in section 3.1, the BTE requires a large amount of input parameters in order to become solvable: transmission and reflection coefficients for interfaces, reflection models for boundaries, phonon lifetimes, models of scattering events, etc. These parameters are not readily available, and necessitate estimation by a combination of theoretical techniques, such as molecular dynamics (MD) and density functional theory (DFT) [101, 102]. Both MD and DFT techniques start from the atomic structure of a material and fundamental forces to determine the phonon spectrum and, within the relaxation time approximation (RTA), the lifetimes of phonon modes. DFT results from different materials can now be found in literature, and most of them are in agreement within 15% of each other [103]. The success of DFT approaches to extract phonon dispersion relation and lifetimes has enabled the work by the Minnich research group, as well as the Chen research group that relies on new and fast solvers for the linearized BTE in different geometries and materials, as used in the work of Zeng. et al [104] and Hu et al. [83].

In this chapter, I summarize some of the different models present in literature to interpret experimental results and briefly discuss the use of effective conductivity versus effective resistivity. Next, I present a powerful first-principles approach for understanding thermal transport and implement this technique to model the experimental geometries explored in chapter 3. Based on the results obtained, I discuss the potential mechanisms behind the new collectively-diffusive regime and propose a set of computational experiments to test the main candidates.

4.1 Discussion of recent results in literature

Most, if not all, of the published work on nanoscale thermal transport uses an effective diffusive model to interpret the experimental and computational results. For example, some work on solutions of the linear-BTE still go through an effective model to compare their results to the existing

experimental literature [83]. Typical experiments do not measure temperature directly; instead, most either rely on the modulation of the reflectivity of visible light or on the modification of the diffraction from a grating (visible or physical) due to reflectivity changes and surface deformation. Additionally, theory work compares results to published experimental data, which are based on an effective diffusive model, forcing theory work to use the same step in interpreting their result.In some cases, applying an effective diffusive model, which cannot describe the underlying physics, to describe results can lead to disputes over the validity of the interpretation; therefore, an effort is being made to eliminate this diffusive model step.

Several years ago, a grey-scale approximation and a simple model like the one presented in section 3.5.1 and [45] were the most advanced models available. The field has done much progress since. For visible transient gratings in suspended membranes, much work has been done [105, 106, 89, 107, 108]. In particular, it was proven that an effective conductivity is an exact solution for the temperature field dynamics when boundary scattering is not dominant [89]. For 2D and 3D geometries, effective conductivity is not a valid approach and several different methods to solve the linearized-BTE have been implemented [109, 110, 111].

Experiments which use frequency [82] or size of the laser spot [102] as heat sources have quite complex interpretations today, as it is hard for the experimental analysis to decouple in-plane and cross-plane results as was pointed out by Wilson et al. [112]. Therefore, I will not discuss those experiments, and I will focus the discussion on experimental geometries like the ones presented in chapter 3, where the heat sources are generated by using nanostructured transducers [45].

At the time I first presented our experimental results on the impact of spacing of nanoscale heat sources on heat dissipation efficiency [113], most of the successful ab-initio approaches had not been made public, but were being developed. Up until that point, heat sources that were close enough for the spacing to be on the order of the phonon MFP had not been probed, and our technique was unique and theoretical methods had not yet been employed to study transport in these geometries. Shortly afterwards, Zheng et. al. [104] used a discrete ordinate method to solve the 2D linear-BTE solver in a similar geometry as our experiment. In this work, Zheng et al

argues that the distance between periodic nanotructures will impact the effective conductivity such that structures that were close together could appear to cool down faster. He also argues that the experiments measure the temperature difference between structures and valleys rather than just the structure temperatures. In a following study, Zeng et al. [84] and Hu et al. published new calculations and experiments [83] supporting a faster heat efficiency for periodic nanoscale heat sources when the duty cycle L/P was small, rather than when P/λ_i is small. This discrepancy in our interpretation seem to spawn from the a few key assumptions that differ in the interpretation approaches to the experimental results.

First, there is the use of effective conductivity compared to the use of effective resistivity as effective parameters for the diffusive models used to interpret the experimental data. Although, effective conductivity is both more intuitive and easier to link to the suppression function and the phonon MFP spectrum, it is not a localized parameter. When modeling a system, the conductivity of the substrate at all positions is changed to the new value, having the potential of creating more exotic situations that are harder to relate to the experimental reality. This is most apparent when nanoscale effects are more pronounced, as shown in Fig. 4.1. The reality is that effective conductivity does not describe the experimental data in our experiment Fig. 4.1a, or even other experiments Fig. 4.1b [83]. As shown in Fig. 4.1b, the fit will give you the average thermal decay convoluting the interpretation. We use effective resistivity because it is inherently localized while carefully interpreting the effective parameter, not as physical reality but rather as a quantitative measurement as described in section 3.5.2. Another potential approach is a depth dependent effective conductivity (as hinted in section 3.5.2) as shown in Fig. 4.1a. It does provide a better fit to the data in general, but I cannot base the inclusion of an additional free parameter from first principles, and therefore do not trust the physical meaning of an additional fitting parameters (although I recognize the usefulness of this approach).

Second, Hu et al. can only compare the linear BTE solutions to experiments by assuming that the suppression function is monotonic; therefore, baring the possibility that P/λ_i influences the results. That is why they extract a different suppression function for each value of the duty cycle.

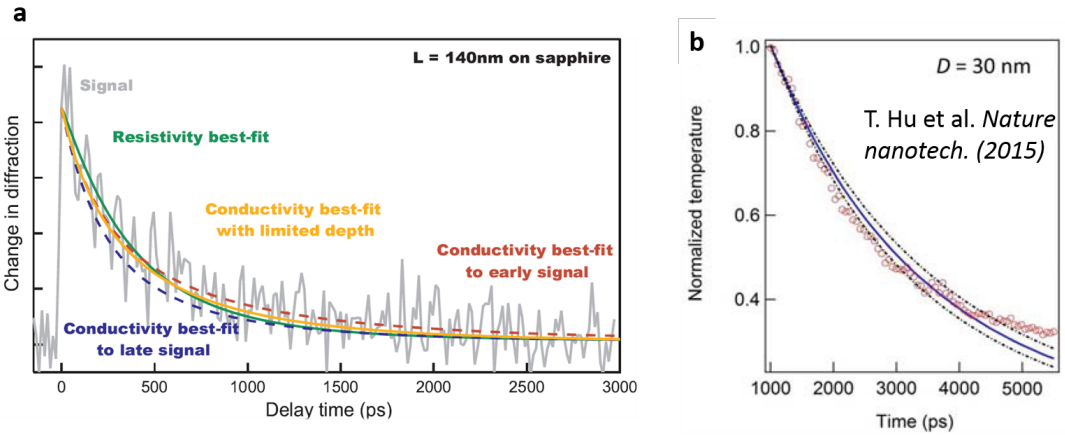

Figure 4.1: **Effective conductivity compared to effective resistivity when analyzing two different experiments** textbfa. An EUV nanometrology data trace probing thermal transport away from nanoscale heat sources $L = 140nm$ and $P = 4 \times L$ on Silicon substrate fitted with the best fit using effective resistivity (green), effective conductivity fitting the early signal (red) and late signal (blue) and using a depth-limited effective conductivity (yellow). It is clear that just using effective conductivity fails at describing the dynamics of the sample. This is also clearly in **b** from [83] where the best fit is shown for 30nm nanocubes on top of a silicon substrate.

According to those authors, our results on the 25% duty cycle samples that show a turnaround in effective resistivity are in contradictions with their findings using the BTE. However, the dependence on L/P is directly built in the assumptions they start with before analyzing their data. Further work is needed to shine a light on the physical mechanism of the observed turnaround.

More experimental work and theoretical calculation, where the assumptions do not favor a particular interpretation, are need to distinguish the physical mechanism for the observed trends. However, since the observation of the turnaround for r_{eff} in constant duty cycle samples was confirmed, it is likely that the suppression function directly depends on the value of the spacing between heat sources, similar to its dependence on the value of the linewidth of the heat sources.

In order to progress, experimental and theoretical efforts need to detach from their dependence on the effective diffusive models. A few models, also derived from the linear-BTE, have been proposed like the Levi flight model (or super diffusive model) [114] or hydrodynamic models [115, 116]. However, it might be useful to directly interpret experimental results from the linear (or full) BTE without intermediate models, as illustrated in Fig. 4.2.

4.2 Implementation of a variance Monte Carlo for real experimental geometries

When looking for a specific approach to solving the BTE directly, I needed a methodology which could solve for relatively large areas (and potentially volumes) with relatively low amount of computational power. Through collaboration, I received access to the work of Peraud et al. [110] who developed a variance-reduced Monte Carlo approach to solve the BTE. This technique is based on solving the BTE only in areas (and volumes) that are out of equilibrium. This method provides a fast computational approach for situations where the out of equilibrium areas (or volumes) are small compared with the rest of the geometry, as in our experimental geometries.

In this approach, the RTA BTE for a particular phonon mode is transformed into energy space:

$$\frac{\partial e^d}{\partial t} + \mathbf{v}_g \cdot \nabla e^d = \frac{(e^{loc} - e^{eq}_{T_{eq}}) - e^d}{\tau} \tag{4.1}$$

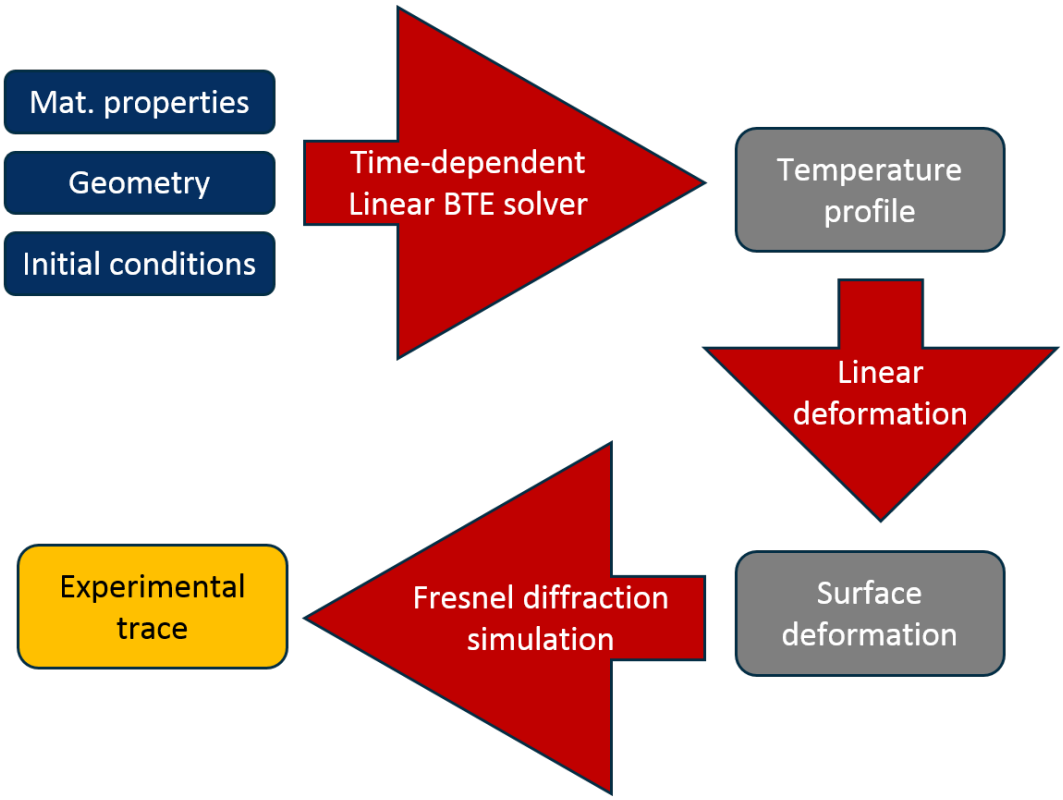

Figure 4.2: **Work-flow for implementing a direct route form the linear-BTE to our experimental traces** Illustration of the needed steps to generate experimental-like traces using a linear-BTE solver without a diffusive model interpretation step. The codes of light diffraction and thermal linear expansion are already available, as we use them in our work presented in chapter 3.

where $e^d = e - e^{eq}_{T_{eq}} = \hbar\omega(f - f^{eq}_{T_{eq}})$, $\tau = \tau(\omega, p, T)$ is the relaxation time, $f = f(\mathbf{x}, \omega, p, \theta, \phi)$ is the occupation number of phonon states, $\mathbf{v}_g$ is the group velocity of the phonon-bundle, and $f^{eq}_{T_{eq}}$ i.e. the Bose-Einstein distribution at the reference temperature T_{eq}. Dynamics simulations of a particular situation can now be solved with a Monte-Carlo scheme, where the particles are small bundles of energy that evolve according to Eq. 4.1 and scatter with relaxation time τ. Upon scattering, a particle deposits its energy (changing T_{loc}) and a new energy packet is drawn from the local distribution. However, if the temperature differences are not large, i.e. $< 10\%$, we can write $(e^{loc} - e^{eq}_{T_{eq}}) \approx (T_{loc} - T_{eq})\frac{\delta e^{eq}_{T_{eq}}}{\delta T}$. Which means that the particles can be drawn from the original distribution that does not depend on T_{loc} and energy conservation is ensured by conserving the number (and energy) of the particles. The upside of this formulation is that each energy bundle can be simulated independently (since particle scattering events do not depend on small variations of T_{loc}) and the results can be computed at the end once all particles are propagated through time. This allows for parallelization resulting in decreased computational time.

4.2.1 Building the calculations

I implemented a version of this code starting from the c++ code made available through github by Peraud et al. [117]. I then subsequently added thermal boundary conditions to be able to simulate an interface. I also implemented a matlab script that sets up the geometry, boundary conditions, and initial conditions required for the calculation. Just as described in chapter 2, periodic boundary conditions were used in order to simulate a grating. For each situation simulated, an appropriate number of energy particles was used (usually 1 million, but a larger number for larger simulations cells), and each simulation was run 100 times independently to average out numerical noise. Simulations input for silicon were used from Peraud et al.[117] and Minnich [47], allowing me to perform the calculations taking into account the full phonon spectrum.

The results of solving the linear BTE for periodic hot silicon nanostructures on top of silicon substrate without a thermal boundary (both made out of silicon) are presented in Fig. 4.3 and Fig. 4.4 for two different heating initial conditions. The temperature at each element in space

(visible in both Fig. 4.3 and Fig. 4.3) is calculated using the energy present in the element at each time step. Therefore, I can extract the temperature in the structure, the substrate just below the structures, and the substrate surface at the most distant point to the heat sources (the valley). I first validated a large heat source where both the BTE and the diffusive model predict the same temperature dynamics. Then, I performed the calculation for small nanostructures ($L = 20nm$) at different periodicities $P = 40nm$ and $P = 400nm$, shown in Fig. 4.5. When comparing with FEA using effective conductivity, the results where significant, and can be summarized as follows. First, the temperature in the nanostructures spaced close together is not lower than the temperature in the ones spaced far apart. Unfortunately, this does not directly reinforce or disprove the behavior suggested by our experiment. Second, when using an effective diffusive model to fit the temperatures, we do see that the value obtained for the nanostructures with $P = 400nm$ is $k_{eff} = 0.05 \times k_{bulk}$, and when using this same value in the nanostructures with $P = 40nm$ it completely misses the temperature dynamics. Therefore, the k_eff for $P = 400nm$ is **lower** than the one for $P = 40nm$. This confirms the strong effect of the spacing between heat sources on the thermal dynamics.

One possible explanation is that the observed dynamics of the experiment cannot be captured by the linear-BTE thus requiring a closer look at the full BTE or other non-linear effects. Since the experimental results are linear with temperature (we perform the same experiment at different pump powers and observe the same decaying dynamics), it is unlikely that we have non-linear phonon dynamics. However, recent work by [62] and [67] have demonstrated that nanoscale geometries can have non-linear effects on the phonon spectrum of materials. In a similar fashion as we measured in [8], nanoscale pieces of materials that are close together cannot be treated separately, leading to the idea that a nanostructured material is not like the average of the properties of the different components. So far, these computationally expensive calculations have been done in systems where the boundaries are either finite or periodic. The implementation of a semi-infinite case is challenging, but may be possible with current technology and theoretical framework. The most straightforward approach to test this hypothesis (but perhaps not the most efficient one)

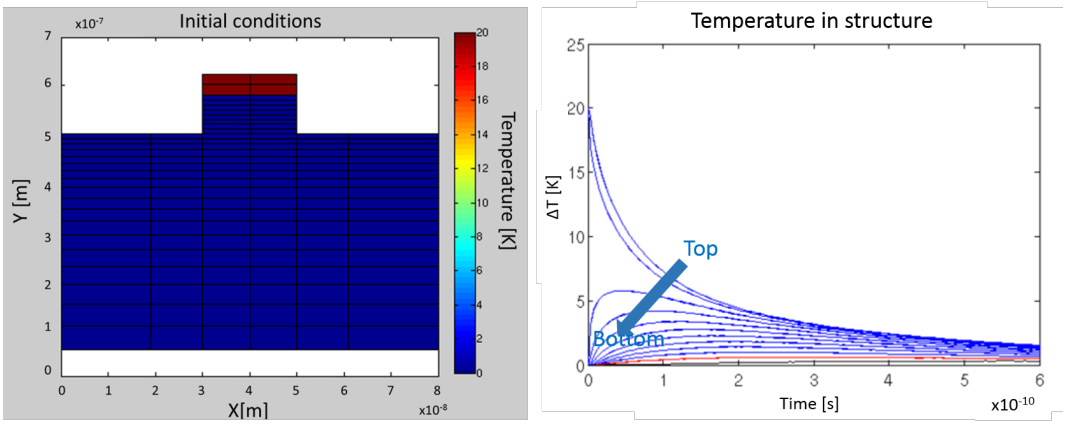

Figure 4.3: **Test of the variance-reduced MC linear-BTE solver in a finFET geometry** Results from heating only the top of a periodic grating $P = 80nm$ of tall $h = 100nm$ and narrow $L = 20nm$ silicon nanostructures on silicon. On the left the initial conditions for the temperature field. On the right, the time-dependent temperature dynamics for the nanostrucure. Areas to calculate the temperature are $10nm \times 10nm$ in area. The heat dissipation from top to bottom of the nanostructure is clearly visible.

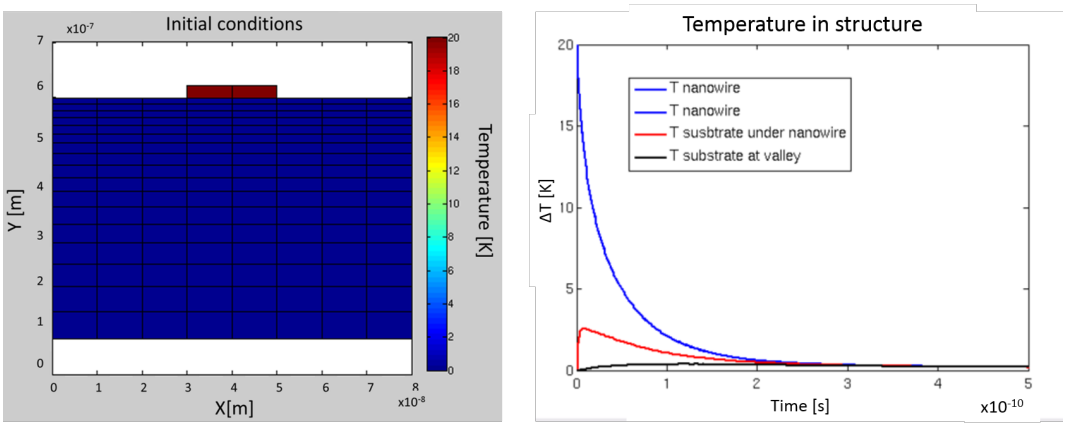

Figure 4.4: **Test of the variance-reduced MC linear-BTE solver in a typical experimental geometry** Results from heating only the top of a periodic grating $P = 80nm$ of short $h = 10nm$ and narrow $L = 20nm$ silicon nanostructures on silicon. On the left the initial conditions for the temperature field. On the right, the time-dependent temperature dynamics for the nanostrucure (blue), substrate underneath it (red) and valley areas (black).

is to use equilibrium molecular dynamics of the nanostructure-substrate system as a function of grating periodicity to detect trends in the in-plane thermal conductivity that are compatible with the experimental results.

Additionally, note that these results do not include a thermal boundary between nanostructures and substrate. I implemented this boundary and added it to the variance-reduced MC linear BTE, but preliminary results indicate similar observed dynamics. This reinforces the hypothesis of a geometry-driven non-linear effect on the phonon spectrum of the substrates at the surface. Finally, I only presents temperature results. I implemented a finite element approach to compute the elastic deformation of the system based on the temperature profile, similar to the approach of Siemens [45]. However, more work needs to be done to validate the computations.

4.3 Conclusion

In this chapter, I have discussed the current limitations of computational approaches used in experiments today. I discuss the differences present in literature today and discuss the potential sources of discrepancy. I also present the implementation of a variance reduced Monte Carlo linear BTE solver for geometries similar to our experiment. The results corroborate our experimental findings as they point out to a strong dependence of the heat dissipation efficiency on the period of the gratings. However, this model does not capture all of the observed dynamics. One possible explanation is that the nanoscale geometries on our samples are affecting the phonon spectrum of the substrates close to the surface in a significant non-linear way, as has been observed for thin films of similar in-plane length scales. In order to test this theory, ab-initio equilibrium molecular dynamics calculations are needed to calculate the phonon dispersion of our samples.

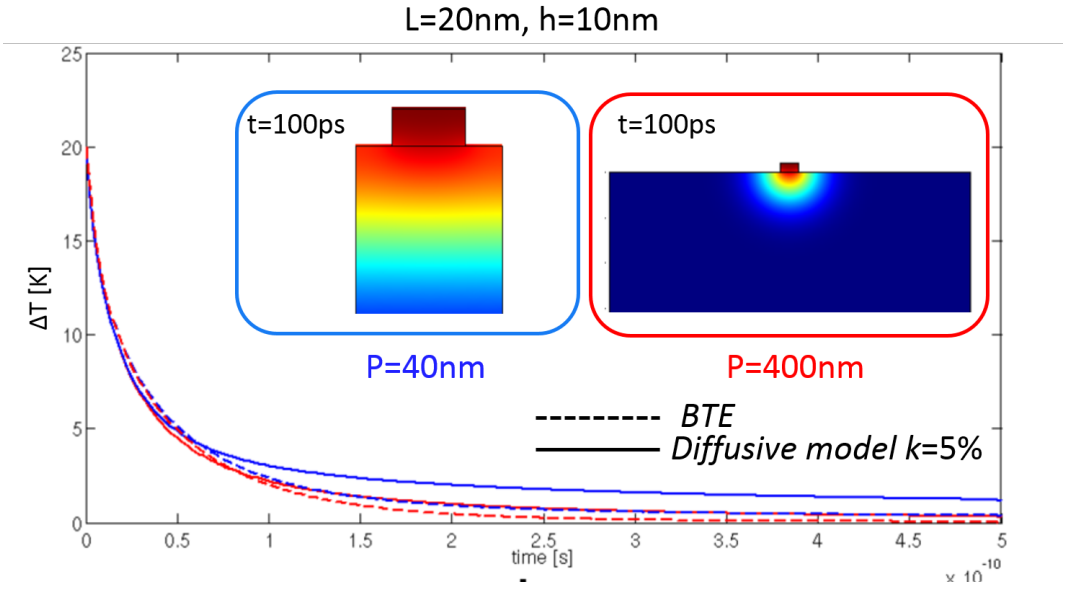

Figure 4.5: **Temperature from linear-BTE compared with effective diffusive model** Effective conductivity diffusive model (solid lines) and the linear-BTE (dashed lines) calculated temperature dynamics for nanostructures with height $h = 10nm$, linewidth $L = 20nm$. The case of close-packed nanostructures $P = 40nm$ (blue) is compared with semi-isolated ones $P = 400nm$ (red). Material is just silicon on silicon, no thermal boundary. We see that the linear-BTE does show that the semi-isolated nanostructures have a lower temperature. However, when using effective conductivity on the semi-isolated case, an effective conductivity os 5% of bulk value is found. This value is much higher for the close-packed structures, confirming the strong impact of periodicity on the heat dissipation dynamics of nanoscale heat sources.

Chapter 5

Novel ultra-thin film EUV metrology

Thin films have become ubiquitous to modern technology, used in a range of applications, including packaging, smaller semiconductors, enhanced conductors and insulators, chemical protection, among others. Films thinner than a few μm can be found in food and drinks cans, car engines and cellphones. Driven by technological needs, nanofabrication of thin films has reached impressive levels of precision (with atomic layer deposition techniques), and of scale (depositing thin films on areas as large as $45cm$ diameter wafers). However, as films reach tens of nanometers in thicknesses, traditional characterization tools fail. This chapter presents the successful use of coherent EUV nanometrology as a way of characterizing the complete mechanical properties of isotropic sub-100nm thin films, gaining access to information that was until now unavailable with other techniques.

The chapter starts with a short theoretical introduction to the continuum mechanics concepts at the core of our technique and a short review of current available techniques to characterize mechanical properties of thin films. It then moves on to present our measurements, data analysis and results.

5.1 Theoretical introduction

As discussed in chapter 3 and section 3.1, the microscopic atomic structure of solids is what dictates all macroscopic properties. In particular, the equilibrium position of the atoms and the forces resulting from deviations from equilibrium are consequences of the potentials existing in the

solid (van de Waals forces for example). However, when describing a solid from the continuum mechanics perspective, information on individual atomic dynamics is lost, and we focus instead on the integrated effects of the atomic forces on a solid. In continuum mechanics, a solid is often defined as a deformable body that can sustain shear strength (as opposed to liquids) [118]. Macroscopic properties such as stiffness, compressibility, hardness, etc. are then a direct consequence of not only the chemical composition of a material, but of the geometrical arrangement of atoms, which changes the inter atomic potentials. For example, coal, diamond, graphene and graphite have drastically different properties due to their different atomic structures, even though carbon is the only atom present.

Continuum mechanics provides a very useful approach to characterize a material that relates **strain** to **stress**. Strain is defined as the deformation of a body with respect to its equilibrium configuration and is the continuum equivalent of the deviation from the equilibrium of an atom $u(R)$ used in chapter 3 section 3.1. Stress is the mathematical representation of the force per unit area exerted on the material. For our experiments, it is a reasonable approximation to only consider relatively small strain so that two neighboring atoms in the lattice are still neighbors under a deformation. Moreover, for our experiment we stay within the limits of the linear regime (which allows us to have repeatable experiments). In a general form, stress can be represented as a 3×3 matrix contains the information of the pressure at any point in the body, so that the pressure alon a direction i is given by the sum of normal stress σ_{ii} and shear stresses $\sigma_{ij}, i \neq j$. Similarly, strain can also be represented by a 3×3 matrix where the different components of the strain along different directions, $L_{i,j}$. It can be shown [118] that both the stress and strain tensors are symmetric matrices, so that $\sigma_{ij} = \sigma_{ji}$ and $L_{ij} = L_{ji}$. Strain is related to the deformation (the usual calculated quantity) $L_{ji} = u_{ij}/L$, where L is the original size of the object.

The way a materials strain changes in response to stresses is at the core of the mechanical properties of the material. All of the more usual parameters (such as Young's modulus, hardness, stiffness, etc.) can be derived from this response. This fundamental mechanical property is represented by the elastic tensor of a material $\mathbf{c}_{ijkl}$,

$$\sigma_{ij} = \mathbf{c}_{ijkl} L_{kl} \tag{5.1}$$

This equation is the generalization of Hooke's law, the stress-strain relationship for the equation of motion of a spring under a small strain. The elastic tensor $\mathbf{c}$ contains all the information about the microscopic structure of a material. However, its components are inherently macroscopic, capturing the complex nature of the integrated microscopic strain at larger scales. Specific components of the tensor (or specific combinations of the components of the tensor) might be of more interest to a particular problem. For example the compressibility along a specific axis will involve both the strain caused parallel to that axis ($\mathbf{c}_{iiii}, i = 1, 2, 3$) as well the strain in the orthogonal directions to that compression ($\mathbf{c}_{iijj}, i \neq j$ and $\mathbf{c}_{ijij}, i \neq j$).

Mathematically, $\mathbf{c}$ is a $3 \times 3 \times 3 \times 3$ tensor, having 81 components. However, due to the following fundamental symmetries that apply to all materials under linear deformations, one can prove that $\mathbf{c}$ only has 21 independent components: $\mathbf{c}_{ijkl} = \mathbf{c}_{ijlk}$, $\mathbf{c}_{ijkl} = \mathbf{c}_{jilk}$, and $\mathbf{c}_{ijkl} = \mathbf{c}_{klij}$. This means that with only 21 independent parameters it is possible to characterize the linear elastic response of any material. A material with 21 independent parameters is called an anisotropic material.

Most of the materials of interest to our research are not fully anisotropic, as each symmetry in a materials atomic structure is translated into fewer independent parameters of the elastic tensor. For example, a monoclinic material (a material that has a symmetry with respect to one plane) only has 13 independent parameters. A cubic material's elastic tensor only has 3 independent parameters. Finally, an isotropic material (that has the same elastic properties in all directions) only needs 2 parameters to fully capture its elastic response (see [118] for more details).

As our experiments measure amorphous materials that can be approximated as isotropic, we only need to extract 2 parameters of the elastic tensor in order to fully characterize the elastic properties of these materials. These parameters are usually referred to as the Lamé constants, λ and μ. The elastic tensor for an isotropic material is then characterized by $\mathbf{c}_{iiii} = \lambda + 2\mu, i = 1, 2, 3$,

$\mathbf{c}_{ijij} = \mu, i, j = 1, 2, 3$ and $\mathbf{c}_{iijj} = \lambda, i, j = 1, 2, 3$. Lamé constants are not very often used when making measurements, as they are hard to extract directly. It is more common to find references to Young's modulus, E, and Poisson's ratio, ν, where:

$$\begin{aligned} E &= \frac{\mu(3\lambda + 2\mu)}{\lambda + \mu} \\ \nu &= \frac{\lambda}{2(\lambda + \mu)} \end{aligned} \tag{5.2}$$

The Young's modulus E characterizes compressibility of a material, and can be measured directly by exerting a load along a specific axis and measuring the strain along that axis, as shown in Fig. 5.1. The Poisson's ratio ν relates the strain in the orthogonal direction to the load exerted on a material, as shown in Fig. 5.1.

Young's modulus relates to what we sometimes call the stiffness of a material, and it can take a very wide range of values, from $MPa = 1^6 N/m^2$ (soft) to TPa (stiff). Poisson's ratio, on the other hand, is a well bounded parameter that only assumes values between -0.5 and 1. Positive values correspond to most conventional materials that expand in the orthogonal directions upon compression. A value of 0 corresponds to a "compressible" material that does not expand orthogonally to its compression (such as a cork), and a value of 0.5 corresponds to a fully incompressible material such as a water balloon (or rubber), where the expansion in both orthogonal directions is half of the compression. Negative values of Poisson's ratio correspond to an interesting class of materials that upon compression in one direction, the orthogonal directions are also compressed.

It is also useful to relate E and ν to the independent components of the isotropic elastic tensor, in particular $\mathbf{c}_{1111} = \mathbf{c}_{2222} = \mathbf{c}_{3333}$ which I will abbreviate $\mathbf{c}_{11}$ and $\mathbf{c}_{ijij}, i, j = 1, 2, 3$ which I will abbreviate as $\mathbf{c}_{44}$:

$$\begin{aligned} E &= \mathbf{c}_{44}\frac{3\mathbf{c}_{11} - 4\mathbf{c}_{44}}{\mathbf{c}_{11} - \mathbf{c}_{44}}, \\ \nu &= \frac{\mathbf{c}_{11} - 2\mathbf{c}_{44}}{2(\mathbf{c}_{11} - \mathbf{c}_{44})}. \end{aligned} \tag{5.3}$$

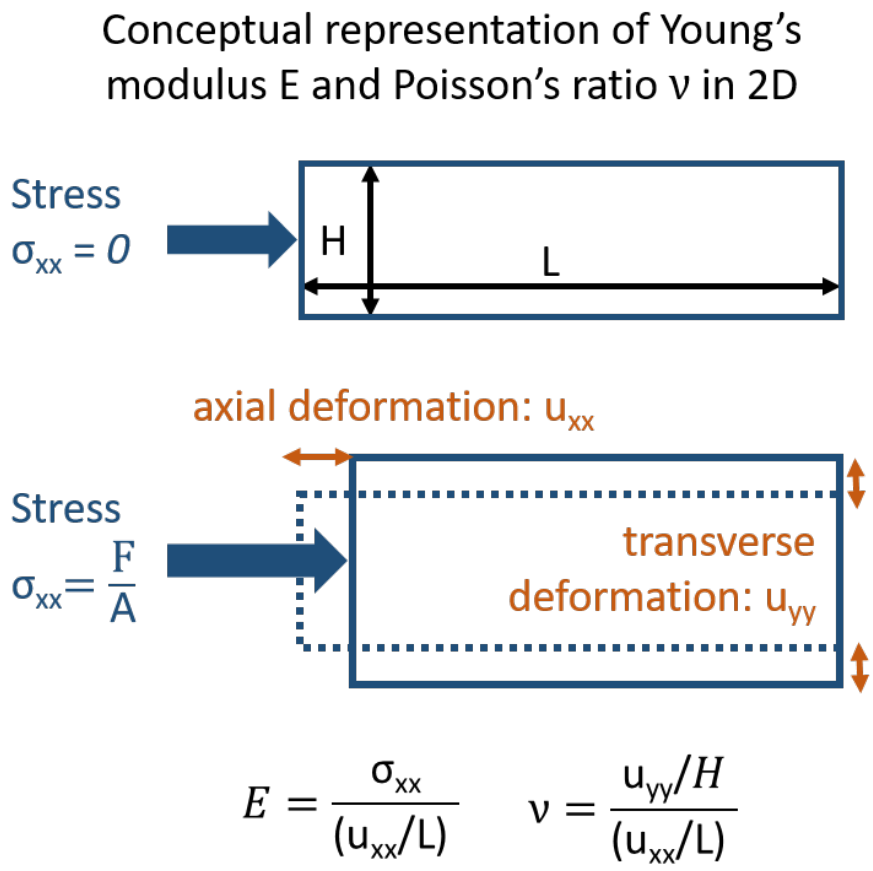

Figure 5.1: **Illustration of Young's modulus and Poisson's ratio in 2D** When comparing a stress-less body volume (top) to one subjected to stress in one direction (bottom), the resulting axial and transverse deformations characterize the material's Young's modulus and Poisson's ratio. The equations show how both parameters can be extracted from studying a body deform under a controlled pressure|

5.2 Current traditional elastic metrology techniques and their limits

While a number of techniques are available for the mechanical characterization of thin films, most become less accurate as the film thickness shrinks below 100nm. Contact techniques modeled after macroscale counterparts, such as nano-indentation, where an atomic force microscope (AFM) tip measures the responding stress to a load that it presses into the film, struggle to decouple the properties of the substrate from those of the film for thicknesses below $1\mu m$ [119]. Moreover, reliable measurements of films with thicknesses of hundreds of nanometers using nano-indentation is only possible by using complex modeling [120, 121]. This makes the characterization of multilayers, or of materials where the thickness is not well known, impossible, with the added disadvantage of damaging the samples upon measurement.

A newer atomic force microscopy-based technique is contact resonance AFM (CR-AFM), which relies on the shift of mechanical resonances of a AFM cantilever when the tip is moved into contact with a material surface. This technique involves a smaller area of contact and smaller forces, which minimizes the damage to the sample [122]. However, this technique still struggles to decouple the properties of sub-$200nm$ thin films from the substrate's, but it is more successful in doing so with high quality AFM tips [123]. This technique does, however, require strong models for both cantilever eigenmodes and substrate properties, as well as reference samples for comparison [124]. CR-AFM has proven to offer a very sensitive tool for mapping local variations in elastic properties across a surface when the differences, rather than the absolute values, are of interest.

For both nano-indentation and CR-AFM, when characterizing thin films, the absence of sensitivity to shear stress makes them only able to measure the Young's modulus of the material, therefore not allowing for a full characterization of the elastic properties.

Non-contact techniques can be used successfully for sub-$1\mu m$ films, but still face various challenges. Brillouin light scattering techniques rely on the study of the interaction of light and acoustic phonons and can ideally extract the full elastic tensor of a material. When the acoustic impedance between the film and the substrate is large, Brillouin light scattering has been used to

successfully characterize the full elastic tensor of a 25nm thin film [125]. However, in the majority of cases, interpretation of the experimental data requires complex modeling, making it difficult to extend this approach to sub-100nm thin films. Moreover, the weak intensity of the scattered light, combined with the challenge of properly identifying the phonon modes, make this approach strongly dependent on the experimental accuracy attained [126].

Picosecond ultrasonics, another powerful non-contact technique, utilizes visible light to probe the propagation of acoustic waves in materials launched either by a train of short laser pulses, or by the impulsive excitation of metallic transducers on the surface of the sample [127, 128, 129, 130, 131, 132]. This technique traditionally only measures the longitudinal acoustic wave (LAW) velocity, giving only access to one parameter of the elastic tensor and forcing the assumption of the Poisson's ratio of the material. The introduction of patterned transducers to launch surface acoustic waves (SAW) that propagate in an almost orthogonal direction as the LAWs [133, 134, 135, 136] allows to gain access to both Young's modulus and Poisson's ratio. However, as thinner films require shorter-wavelength surface displacements, these techniques are limited by the wavelength of the visible probe when measuring sub-$200nmfilms$. Thus far, visible-light picosecond ultrasonics with nanostructured transducers has been used to characterize films as thin as $260nm$ [133]. Nevertheless, due to the simplicity of the data analysis, this approach is attractive for characterizing the Youngs modulus of films down to $5nm$ in thickness [130], provided that a value for the Poissons ratio can be assumed. However, this is not always a correct assumption.

In recent years, asynchronous optical samplings (ASOP) has increased the sensitivity of picosecond ultrasonics such that vertical breathing modes can be resolved in metallic films 5-15nm in thickness[137, 138]. In ASOP, the pump and probe pulsed lasers operate at GHz frequencies that are slightly detuned from one another, and the pulse to pulse reflectivity change of the probe is measured. This removes the need for a mechanical delay stage, and allows for very high statistics, high temporal frequencies and long time-windows. Nonetheless, the fundamental diffraction limit of visible light probes prevents these techniques from resolving structured nanoscale systems. Moreover, the data analysis needed makes the study of non-uniform films extremely challenging.

However, this technique is an attractive one to keep in mind for future work, as sources of short wavelength coherent light increase in repetition rate (currently in the tens to hundreds of KHz).

5.3 Coherent EUV nanometrology for the full elastic characterization of sub-$100nm$ isotropic thin films

5.3.1 Sample preparation and characterization

As described in chapter 2, our experiments rely on nanostructured transducers being fabricated on top of different samples of interest, in this case, low-k dielectric thin films (SiC:H and SiOC:H). We follow SAW and LAW dynamics launched by the impulsive excitation of arrays of nickel nanolines with different separations, and linewidths ($L = 15nm$ to $L = 500nm$) on top of several low-k dielectric thin films (SiC:H and SiOC:H). The period of the nanolines is maintained at three times the linewidth (1/3 duty cycle) so that SAWs with wavelengths as small as $45nm$ can be excited. Each grating covers a total film area of 150m by 150m. The pump laser beam consists of $30fs$ duration pulses at a central wavelength of $780nm$, which irradiate the sample at a fluence of $\approx 10J/pulse$ in a $400m$ diameter spot size. This ensures a nearly uniform heating of the full Ni grating area. The small height ($\approx 12nm$ on average) of the nanolines ensures a nearly uniform heating through the depth of the individual grating lines. The samples were fabricated by Intel corp. under the leadership of Dr. Sean King. The nanofabrication was done at LBNL by Dr. Erik Anderson and Dr. Weilun Chao using e-beam lithography and liftoff and result in very successful gratings, as shown in Fig. 5.2.

The thin films that we probed were extensively characterized at Intel corp. using XRR measurements for thickness and density, and Rutherford back-scattering and nuclear reaction analysis for chemical composition detailed and CR-AFM for Youngs modulus in [139, 140].

5.3.2 Data analysis

In our experiment, we extend concepts from picosecond ultrasonics into the deep nano-regime by using shorter wavelength coherent beams ($\approx 30nm$ wavelength). Upon heating, the metallic

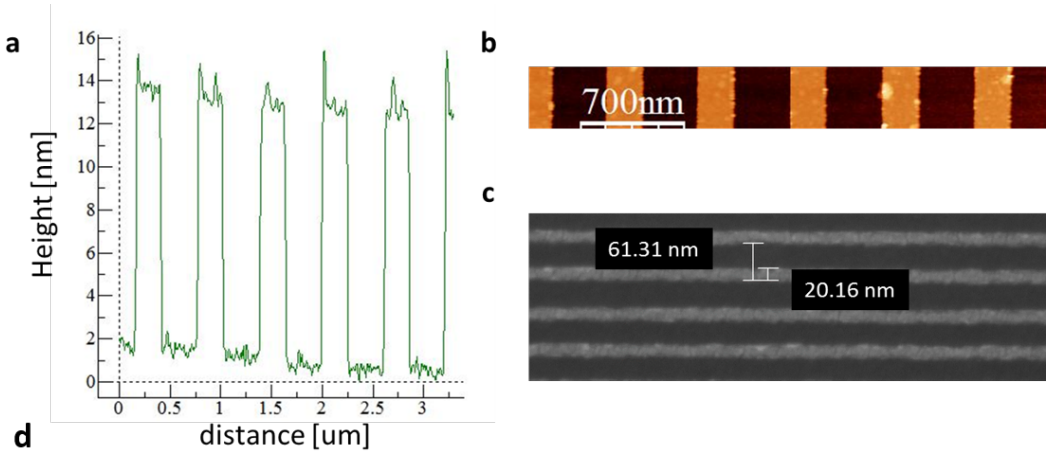

Nominal thickness [A]	Measured thickness [A]	Nominal Young's modulus [GPa]	Wafer #	Network connectivity	C/Si ratio	Density [kg/m^3]
1000	658	4.7	63	2.02	1.10	1300
1000	1031.6	13.05	7	2.39	1.20	1900
1000	1316.2	12.87	5	2.43	1.50	1800
1000	952.5	33.12	75	2.56	1.10	1800
1000	979.1	62.08	65	2.62	1.10	1900
1000	1033	153	9	3.06	0.98	2200
1000	836.4	175	49	3.2	1.02	2700
100	109.1	25	155	N/A	N/A	1500

Figure 5.2: **Characterization of gratings used for the elastic characterization of thin films** The gratings nanofabricated on top of the thin film samples were characterized using AFM **a,b** and SEM **c**. The thin film properties in **d** were extracted at Intel corporation using XRR measurements for thickness and density, and Rutherford back- scattering and nuclear reaction analysis for chemical composition detailed in [139, 140]

nanostructures expand impulsively and launch acoustic waves: SAWs in the film and substrate, and longitudinal acoustic waves (LAWs) within the nanostructures and also within the film and substrate. The first order SAW wavelength, Λ, is set by the period, P, of the nanostructures. The $45nm$ grating period produces SAW wavelengths that are as small as the previous record setting work[141], and an order of magnitude shorter than those accessible using current visible transient grating techniques [59, 142].

By monitoring the EUV diffraction as a function of delay time between the laser pump and EUV probe pulses, we can simultaneously resolve the different acoustic and thermal dynamics of the sample, as illustrated in Fig. 2.10. Resonant longitudinal acoustic waves (LAWs) are launched in the metallic nanostructures with few picosecond periods and lifetimes. Echoes can be seen from LAWs propagating down into the film and reflecting off the substrate interface with return times between $\approx$ 5-50ps. SAWs with $\approx 100ps$ periods are launched at the same time. Finally, one can observe the nanosecond-scale thermal decay of the nanolines as heat dissipates into the film and substrate. The SAW wavelength is set by the periodicity of the gratings, and the SAW penetration depth is directly related to this period $\zeta \approx \Lambda/\pi$ [143, 144]. For sufficiently short nanostructure periods, the SAW is mostly confined in the thin film, and thus the extracted LAW and SAW velocities are exquisitely sensitive to the elastic properties of the films. The LAW and SAW velocities, v_{LAW} and v_{SAW} are given by:

$$v_{LAW} = d/t_{echo}, v_{SAW} = P f_{SAW}, \tag{5.4}$$

where d is the thickness of the thin film material obtained through X-ray reflectivity (XRR) measurements, t_{echo} is the measured round-trip time between LAW echoes at the surface, and f_{SAW} is the measured SAW frequency. Therefore, the two parameters extracted directly from the dynamic diffraction data are: the SAW frequency using Fourier transform and chirp-Z transform and the LAW pulse return time by detecting the characteristic signal in the data traces from several gratings on the same film, as shown in Fig. 5.3.

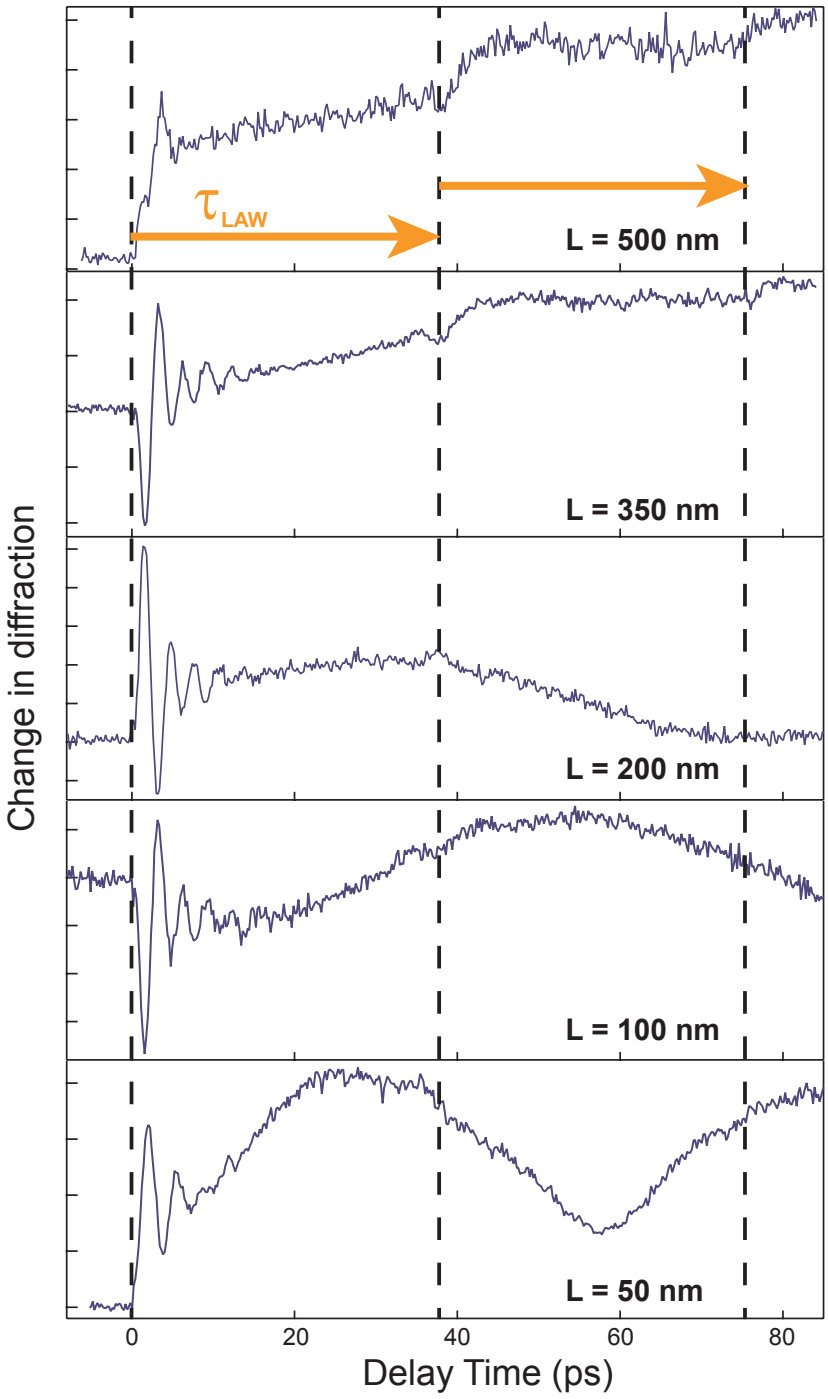

Figure 5.3: **Resolving the return time of LAW echoes at the sample surface** The signatures of the echoes of LAWs reflecting off the thin film-substrate interface are present in all the grating measurements. By checking the consistency of the signal among different nanograting responses, we can extract with the return time of these echoes, and thus the LAW velocity for a film of known thickness. | Figure adapted from [22]

This technique can detect the LAW reflection echoes even from interfaces with low acoustic impedance mismatch (less than 20%) due to the exceptional sensitivity of the EUV probe. By performing measurements on each film with different grating periodicities, we selectively probe different depths into the sample, as demonstrated by the experimentally extracted v_{SAW} values shown in Fig. 5.4. This selectivity allows us to probe either the elastic properties of the silicon substrate for large grating periodicities, or of the ultrathin film for very small grating periodicities, as well as following the transition from one regime to the other. By extracting the velocities of the surface acoustic waves excited by the smallest gratings, we can calculate the independent components of the elastic tensor of the films using:

$$\mathbf{c}_{11} = \rho(v_{LAW})^2, \mathbf{c}_{44} = \rho(v_{SAW}/\xi)^2, \tag{5.5}$$

where ρ is the density of the thin film material obtained through XRR measurements (shown in Fig. 5.2, and ξ is the ratio between SAW velocity and bulk transverse wave velocity [144]. By using the film thickness and density (Fig. 5.2), we can directly calculate $\mathbf{c}_{11}$ from the LAW pulse return time and provide an estimate of $\mathbf{c}_{44}$. In order to extract an exact value for $\mathbf{c}_{44}$, the mass loading of the nanostructures needs to be accounted for using numerical simulations. We extend the framework for SAWs developed by Nardi et al. [136] to include systems with a thin film between the nanostructures and the substrate. Our numerical approach is extremely similar to the procedure outlined in Nardi et al.[136] for the cases involving a fully confined SAW. The extension of this procedure to account for SAWs propagating in both the thin film and the substrate assumes a perfect interface between the film and substrate. However, this assumption is valid in our experiment for two reasons. First, to extract the elastic properties of the thin film, simulations of only the largest and smallest gratings are required. In both of these cases, the interface quality has the smallest impact. Second, the simulations reproduce the observed dynamics at all sizes of gratings, demonstrating the validity of this assumption and the simulation procedure itself at each penetration depth.

For our FEA calculations, a plane strain approximation was used to perform calculations in 2D. The main assumption of this approximation is that the strain in the direction parallel to the nanolines is 0, which is valid in this case, but not for 2D nanocubes. The three main steps of the FEA calculations are as follows:

(1) We execute a simulation to solve the coupled equations for the profiles of temperature, T, and deformation field, u, in the time domain for a single nanostructure on top of a thin film. The simulation uses Eq. 2.6 and Eq. 2.7, as described in chapter 2.

We perform this calculation for the first 100-200 picoseconds, depending on the size of the structure, in order to find the maximum initial deformation of the surface. The maximum initial deformation is identified by the first maximum displacement of the outer corners of the structure. For these calculations, the temperature dynamics are only calculated for the nanostructure, whereas the mechanical dynamics are calculated throughout the system. Therefore, precise knowledge of the thin film thermal properties is not required.

(2) We perform an eigenfrequency analysis of the grating-film-substrate system to extract the normal modes of the geometry. In this case, COMSOL solves only the mechanical eigenfrequency equation using Eq. 2.8, as described in chapter 2.

(3) Finally, we decompose the deformation field of the time-dependent simulation at the moment of maximum displacement into the normal eigenfrequencies basis. We vary the value of $\mathbf{c}_{44}$ around its estimate until the simulated frequencies of the SAWs match those observed in the experiment. The value of $\mathbf{c}_{44}$ at which this match occurs is the true $\mathbf{c}_{44}$ of the thin film since COMSOL can account for the perturbation to the SAW velocity caused by the mass loading of the nanostructures.

To calculate the thin films elastic tensor, first we verify the silicon substrates elastic properties. We use these same three steps to reproduce the experimental observations at large grating sizes (with approximate film properties given by the experimental results) as the SAW frequency depends

largely on the substrate properties at these large penetration depths. Next, we determine the thin films elastic properties by setting $\mathbf{c}_{11}$ to the experimentally extracted value and following the three steps above, sweeping $\mathbf{c}_{44}$ to reproduce the experimental results for small grating sizes where the SAW is fully confined to the film material. Lastly, we perform the three steps of calculation on the intermediate grating sizes where the SAWs may be very sensitive to interface effects to verify the validity of our findings. Most of the extracted values for v_{SAW} for the intermediate sizes are in good agreement with the experimental values. The few discrepancies present which are most likely due to a complex interface between the thin film and substrate, and could be used to study interface quality. However, we do not focus on this aspect here. The simulations on these intermediate grating sizes corroborate the success of our approach and demonstrate that the interface quality is quite good.

5.3.3 Data Flow and error propagation

Our extraction of SAW frequencies and of LAW return times have error bars inherent to the experimental setup and analysis procedure. For the SAW frequencies, the experimental error is given by the standard deviation of the extracted frequencies of different scans on the same grating size. For the LAW return time, the experimental error is given by the standard deviation across scans and how short in time the signal from the echo is. Note that samples in which the acoustic impedance between the film material and silicon is high have much clearer LAW echoes, and therefore lower error bars.

The final error bar on Youngs modulus and Poissons ratio is determined by propagating the experimental error on LAW and SAW measurements through our analysis procedure. As mentioned above, the value for $\mathbf{c}_{11}$ can be directly calculated from the experimental measurement of the LAW pulse return time. This value depends on the measured echo return time, density, and thickness of the thin film. There is an error associated with each of these quantities, and thus the error on $\mathbf{c}_{11}$ requires independent error propagation using the derivative method,

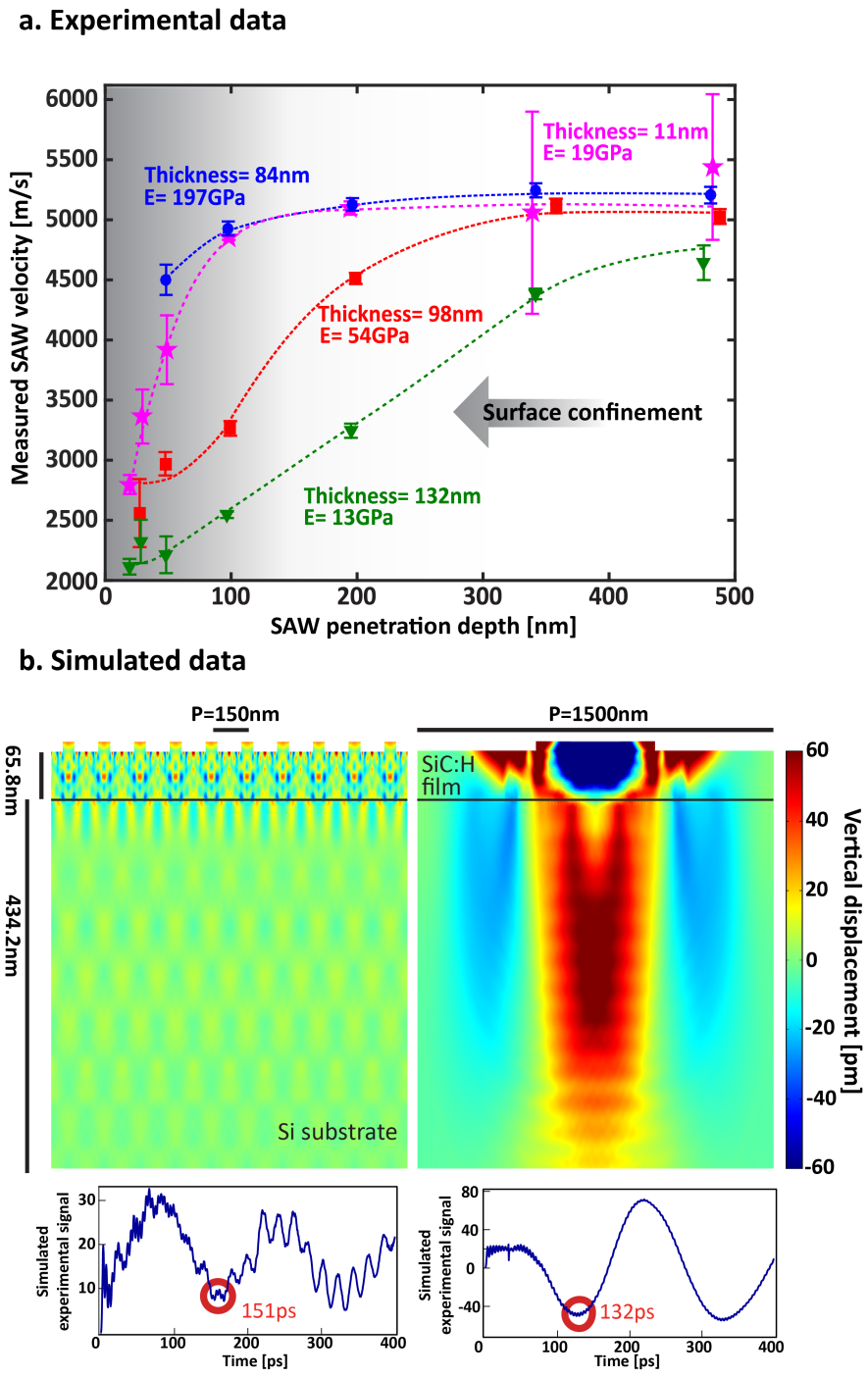

Figure 5.4: **Wavelength dependent confinement of SAWs to thin films. a** Measured SAW velocity for four different thin film samples and different SAW penetration depths set by grating periodicity. Large penetration SAWs are mostly sensitive to the material properties of the substrate, and are comparable for different samples. Small SAW penetration depths confine the SAW to the film and are predominantly sensitive to the thin film properties. SAW velocities are also lower for softer films (green triangles, red squares and pink stars) than for stiffer ones (blue dots), as expected. Dashed lines are guides to the eye. **b** Simulated displacement field from an FEA simulation for a 65.8nm thin film. SAWs generated for a 150nm periodicity grating are fully confined in the thin film material (left), whereas SAWs generated from a 1500nm periodicity grating penetrate the substrate material (right). Both simulated data sets correspond to the first SAW minimum for that grating, as shown on the simulated experimental signal below for reference.| Figure adapted from[7].

$$\delta f = \sqrt{(\sum_i (\frac{\delta f(x_i)}{\delta x_i})^2 (\delta x_i)^2} \tag{5.6}$$

Where δf is the error on $f(x_i)$, a function of uncorrelated, independent variables x_i, each with uncertainty δx_i.

To calculate the error on $\mathbf{c}_{44}$ (and thus Youngs modulus and Poissons ratio), the error on density, thickness, and $\mathbf{c}_{11}$ must be propagated through the simulation procedure, and the error on the measured SAW frequency must be taken into account. To propagate error through the numerical procedure, we first simulate the value of $\mathbf{c}_{44}$ that matches the observed frequency, assuming no values have any error. This step yields the data point of Youngs modulus and Poissons ratio. Next, we alter the values of density, thickness, and $\mathbf{c}_{11}$ to the extreme ends of their error bars. We find the combination that achieves the lowest possible SAW frequency for that value of $\mathbf{c}_{44}$. We then account for the error on the measured SAW frequency by increasing the $\mathbf{c}_{44}$ value until the simulated SAW frequency matches the extreme upper end of the error bar for the observed experimental SAW frequency. With this procedure, we obtain one end of the error bar for our Youngs modulus and Poissons ratio that we quote in the paper. We do a similar process to calculate the other end of the error bar quoted in the paper, using the parameter values that give the highest possible SAW frequency, and lowering $\mathbf{c}_{44}$ to match the lowest end of the experimental SAW frequency error bar. In other words, our error bars on Youngs modulus and Poissons ratio include the most extreme values one could get by choosing any value of an input parameter within the error bars of the measurement. Since the probability is very low that the true value of all of our input values lies at the extreme ends of their error bars, the error bars on our final results are very conservative. Even with these very conservative error bars, we were still able to see a very stark trend in the extracted elastic properties. Lastly, it is good to note that the most dominant error came from the error in the measured SAW frequency and LAW echo times.

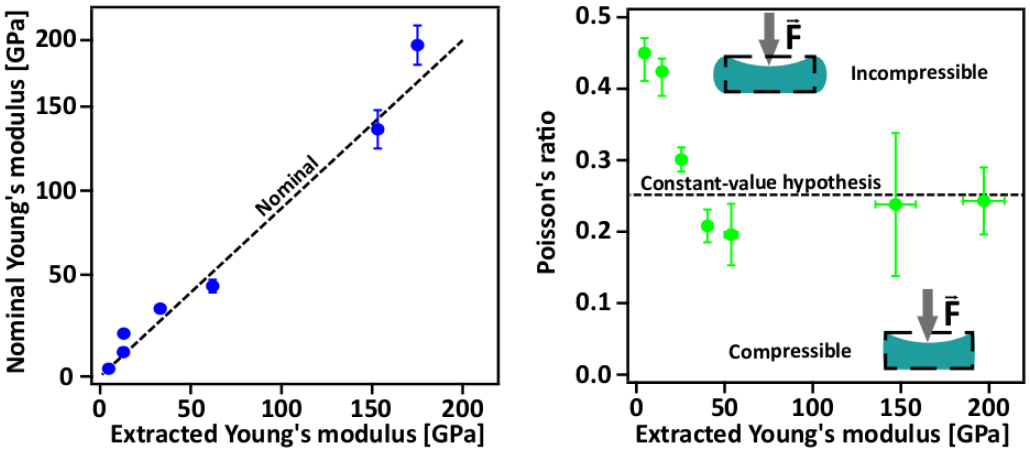

Figure 5.5: **Values of Young's modulus and Poisson's ratio are extracted simultanously for a series of low-k dielectric thin films.** The extracted Youngs modulus (blue) shows good agreement with nominal values, comparable with the results from King et al. [140]. This is the first time that the Poissons ratio (green) for a sub-$100nm$ isotropic thin film series has been characterized. While the extracted values are consistent with a constant-value hypothesis for films with Youngs modulus $> 40GPa$, for films with lower Youngs modulus, the Poissons ratio increases significantly. A Poissons ratio of 0 corresponds to a compressible material, while a Poissons ratio of 0.5 corresponds to an incompressible material, shown schematically on the right.| Figure adapted from [7]

5.3.4 Full characterization of the mechanical properties of 11-50nm ultrathin films

Using this method, we simultaneously extract the Youngs modulus and Poissons ratio of a series of 66-132nm isotropic low-k dielectric thin films, as shown in Fig. 5.5. Our extracted Youngs modulus agrees well with previous measurements on the same films using state of the art nano-indentation[140].However, we observe a previously unknown trend in the Poissons ratio of these materials with decreasing Youngs modulus. In contrast to previous studies, where Poissons ratio was thought to be constant in this type of material,[140] we find that this assumption is not correct for soft films with Youngs modulus lower than $30GPa$. Interestingly, although the nano-indentation measurements assume a constant Poissons ratio, our extracted Youngs modulus values agree well across the whole range. This demonstrates that nano-indentation is inherently insensitive to the Poissons ratio of the material.

Physically, the Poissons ratio of these materials is related to the average network connectivity, as are other thermal and elastic parameters [140]. This result can be understood within the framework of topological constraint theory developed by Phillips and Thorpe [145] and presented by Mauro [146]. In this model, the flexibility and stress of the material can be understood by how constrained the atoms are in the network. The average number of atomic constraints n in a material has to be 3 for a material to be rigid and < 3 for it to be flexible. The average number of atomic constraints is related to the average network connectivity (or average coordination of atoms) r by the relation:

$$n = r/2 + (2r - 3). \tag{5.7}$$

Using this relationship and setting $n = 3$, the critical value at zero-temperature of the network connectivity is found to be $r = 2.4$. This critical value where the material transitions from rigid to flexible is referred to as the rigidity percolation threshold. The average network connectivity for these samples was extracted from nuclear reaction analysis and Rutherford backscattering measurements detailed in [139, 140]. From these measurements, the value of r was obtained by adding up the measured mole fractions of each element to its typical coordination number (i.e.

$rSI = 4, rC = 4, rO = 2, rH = 1$). With this information, King et al.[140] observed large changes in several elastic and thermal properties of isotropic SiC:H films below a rigidity percolation threshold of 2.5.

The increase in Poisson's ratio we observe is also a direct consequence of reducing r below the rigidity percolation threshold, which for these films was due to the hydrogenation of the material that was required to tailor the dielectric constant. Films that have undergone extensive hydrogenation will have more broken bonds, which decreases the network connectivity in the material. With enough hydrogenation, the average network connectivity will eventually land below the rigidity percolation threshold of ≈ 2.5.

We observe that the Poisson's ratio increases to values as high as 0.455, causing the film to behave like an incompressible material, similar to a polymer or water, as shown in Fig. 5.6. This is consistent with observations from Matsuda et al. [147] of an increase of the flexibility of similar materials below the critical value of network connectivity of 2.44. Moreover, using the model presented by Cao and Li [148] to classify metallic glass materials in ductile and brittle categories we see that this series of isotropic SiC:H films go through a transition from brittle to ductile as the average network connectivity is reduced past the critical value.

In addition to studying a series of hydrogenated SiC:H thin films of varying hardness, we also extracted the Youngs modulus and Poissons ratio of a $10.9nm$ SiOC:H isotropic thin film deposited on a silicon substrate. Its nominal Youngs modulus value of $19GPa$ was obtained at Intel Corp. through nano-indentation measurements of a $500nm$ thick film of the same material. We performed this new measurement to explore the limits of EUV acoustic metrology, using gratings with periods as small as 60nm to launch SAWs that were mostly confined to the thin film material (i.e. where the first-order SAW penetration depth was $\approx 19nm$). By applying our analysis procedure, assuming a smooth, ideal interface, we were able to successfully reproduce the experimentally observed acoustic dynamics in our simulations and extract values for both Poissons ratio and Youngs modulus. Although uncertainty due to the incomplete confinement of the first order SAW in the thin film contributes to larger error bars on our data, when combined with precise finite element simula-

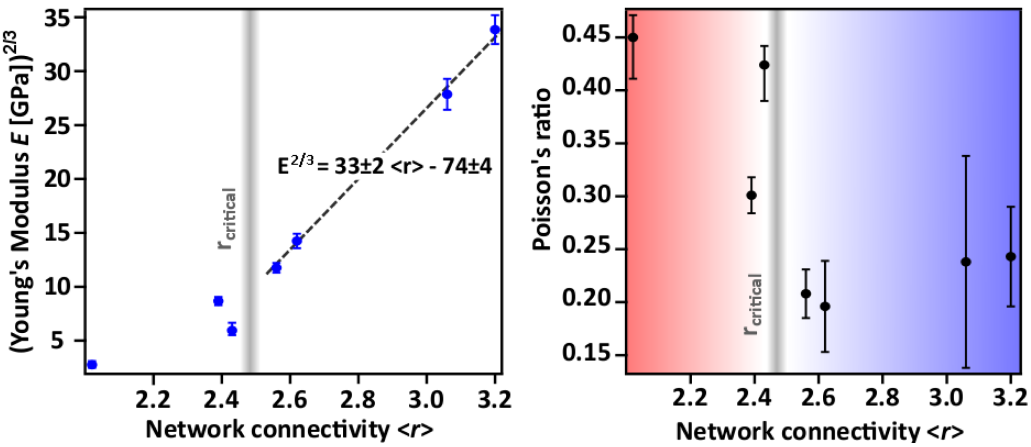

Figure 5.6: Measured Young's modulus, E, values (blue, left) and Poisson's ratio values (black, right) for the film series as a function of the average network connectivity, $< r >$. The extracted Young's modulus values yield the same average network connectivity dependence as King et al. [140] for $< r >$ values above a critical value of ≈ 2.5. This same critical value marks the deviation of Poissons ratio from the assumed constant value. | Figure adapted from [7]

tions, we can still extract reliable measurements for Youngs modulus and a reasonable estimate for Poissons ratio. The extracted value for the Youngs modulus is $35GPa$, with error bars extending from $26GPa$ to $54GPa$. This is slightly larger than the $19GPa$ value measured on a thick film of the same material, which could be due to thickness-dependent changes in the elastic properties of the material when deposited at this extremely small thickness[8]. The extracted Poissons ratio has an exact fit to experimental measurements at 0.393, but has a large allowed range (0-0.450) within experimental uncertainty. This large uncertainty in the Poissons ratio stems from the fact that the return time of the LAWs reflected from the film-substrate interface is very short ($3.11ps$) compared with our experimental error on its measurement, mostly due to LAW pulse duration ($\pm 500fs$). Future upgrades to our system will allow us to overcome this limitation by enhancing signal to noise, and enable the probing of thickness-dependent mechanical properties in ultrathin films.

We also considered the potential impact on our measurement of a thin layer of SiO2 at the film-substrate interface, potentially introduced during the fabrication process and undetected by the sample characterization procedures. We found that accounting for a $1nm$-$2nm$ thick oxide layer in our data analysis procedures results in a shift in the extracted Youngs modulus range to higher values by less than 5%-13%, respectively. Therefore, the existence of this oxide would not explain the discrepancy between the ultrathin film Youngs modulus and the $500nm$ thin film nano-indentation measurement. The impact from uncertainty in the thickness of the film and of the oxide layer could be significantly reduced in the future with the development of coherent EUV reflectometry to characterize our samples. Our measurement represents a full characterization of the elastic properties of the thinnest film to date, including metallic films. Moreover, our approach is not yet limited by the probe light source, but rather by the nano-fabrication that dictates the SAW wavelength. In the future, by using physical gratings with even smaller period and EUV transient grating excitation, it will be possible to fully characterize sub-10nm films, and combined with the use of periodic nanocubes it will be possible to explore size-dependent anisotropies, and asymmetries in the elastic tensor [149].

5.4 Partial characterization of sub-$10nm$ metallic bilayers

Using the same theoretical framework, we can also focus on the resonant mode of the metallic nanostructures, shown in orange in Fig. 2.10 to study how elastic properties evolve when the geometries are less than $10nm$. We studied a series of samples consisting of periodic arrays of bilayer Ni/Ta nanolines on top of a SiO2/silicon substrate. But in this case the linewidth of the nanolines is constant, but the height is changed from one array to the next by adding some Ta thickness to the top layer. In this this work we show that the elastic properties of ultra-thin metallic layers differ significantly from their bulk counterpart, and that the system has to be treated as a whole, rather than the sum of the properties of the two layers present. I actively participated in this work, in particular the data analysis and lead the simulation work. This work was published in [8], and details are also available in Hoogeboom-Pot thesis [22].

5.5 Conclusion

In conclusion, we demonstrate that coherent EUV nanometrology can simultaneously characterize the Youngs modulus and Poissons ratio of isotropic sub-100nm thin films on substrates, as well as partially characterize metallic ultra-thin films ($< 10nminthickness$). This technique allows selective depth sensitivity by tailoring the geometry of a nano-patterned transducer on the film surface. We used the exquisite sensitivity and stability of short-wavelength coherent EUV high harmonic beams to characterize the full elastic tensor of isotropic low-k dielectric films down to 11nm in thickness for the first time. We simultaneously extract the Youngs modulus and Poissons ratio of low-k a-SiC:H dielectric films on silicon substrates with varying degrees of hardness in a single measurement, with Youngs modulus ranging from $5GPa$ to $197GPa$ and average network connectivity from 2.1 to 3.2. The measured Youngs modulus values are in excellent agreement with measurements using alternate techniques on the same materials[150]. However, contrary to past assumptions, the Poissons ratio of such films is not constant, but rather increases significantly from 0.25 to 0.45 for films with Youngs modulus in the range of 5-30GPa. These deviant films have

an average network connectivity below a value of 2.5, showing for the first time that the network connectivity can significantly affect the Poissons ratio in these materials as shown in Fig. 5.7. This new understanding of ultrathin films demonstrates that coherent EUV beams present a new nanometrology capability that can probe a wide range of novel complex materials not accessible using traditional approaches.

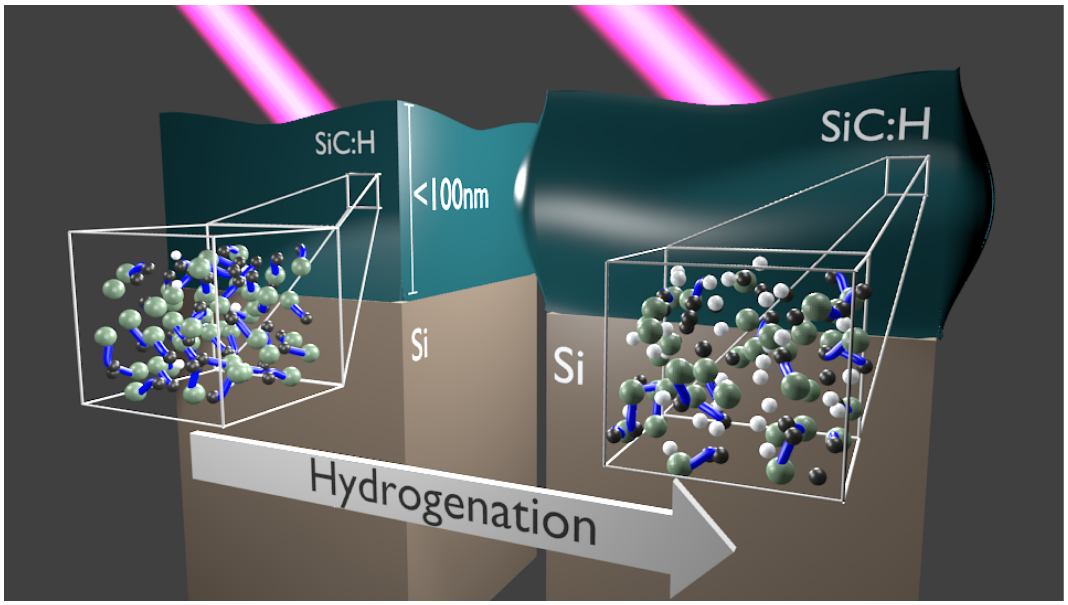

Figure 5.7: **Illustration of the influence of the network connectivity in a material on its elastic properties.** An artistic illustration of the relationship between a material's network connectivity, and compressibility that is uncovered by coherent EUV nanometrology | Figure adapted from [7]

Chapter 6

Science and Technology policy implications

Science is a social and political activity; scientists are humans and citizens. Thus, whether we acknowledge it or not, scientific research is strongly linked to public policies. When thinking about the scientific endeavor, it is not enough to think only about the scientific method. Instead, we must also think about the potential application and impact of our work on public policy. Science and Technology Policy Studies (STP) aims to accomplish this task, and during my time at CU Boulder I have taken part in STP classes, activities, workshops, as well as engaged in lobbying and activism. In this chapter, I share my work around two topics of special interest to me: modeling the scientific endeavor (scientific "progress") and measuring the success of public funding for science and technology. In this chapter I first present a model that describes the temporal evolution of scientific progress and discuss how it relates to my own experience. I then analyze the mechanisms used to measure the performance and impact in two case studies: 1) the energy innovation HUBs started by the Department of Energy (DOE) in 2010[1] , and 2) the American Recovery and Reinvestment Act (ARRA) of 2009.

6.1 Modeling scientific "progress"

There is a public perception that science and technology can be modeled as a linear system, in which basic science produces knowledge that is then transformed into technology, resulting in the creation of companies, jobs and wealth [151]. This linear model provides an oversimplified version

[1] This work is based on the work I performed assisting Prof. Debbie Jin in 2013 as a member of a DOE taskforce that produced a report on the progress of several DOE funding mechanism.

of science and technology development that may have justified public funding for the sciences many years ago, but has today created misconceptions about science and technology for the general public. Much of today's academic activism and public outreach aims to provide a more accurate vision of the scientific endeavor both to other scientists, and to the general public. The first step to achieve this goal is to articulate a new (non-linear) model of the scientific endeavor. In this section, I will present my thoughts and experiences as a scientist in relation to the Kuhnian model of scientific revolution developed in the 1960s [152].

The Kuhnian model of scientific revolution as described in [152] is an attempt to describe the structure of human scientific endeavors historically. As the model is based on historic trends in research, it does not claim to represent present or future situations. Nevertheless, as with all models, we are tempted to do so (and therefore can run into possible induction problems [153]). The Kuhnian model can be summarized in a flow diagram as shown in Fig. 6.1.

The main concept in this model is the concept of paradigm, which is the set of theories and norms that are accepted and taught in the scientific society of a field. There is a paradigm at all times, and the usual and most common situation for a particular scientific field is to perform "normal science" within the constraints of the current paradigm. Normal science experiments are aimed at confirming current theory predictions and increasing the current precision of measurements. However, these experimental measurements will sometimes detect anomalies, placing a particular scientific group or community in an "anomaly state". The "anomaly state" is in general short lived, and most of the time the anomalies will not be seen as questioning the current paradigm, but rather as questioning the experiment itself. This allows that group of scientists to return to the normal science state quickly. However, if enough anomalies are accumulated, and start spreading within the scientific field more widely, then the scientific field will enter a state of crisis. The state of "crisis" usually coexists with normal science. Faced with no alternative theories to replace the current paradigm, the scientific community will continue to work based on known parameters and try to generate alternatives. However, the aim of the experiments and alternatives will usually be to return to the paradigm that is being questioned. But once a particular alternative has enough traction

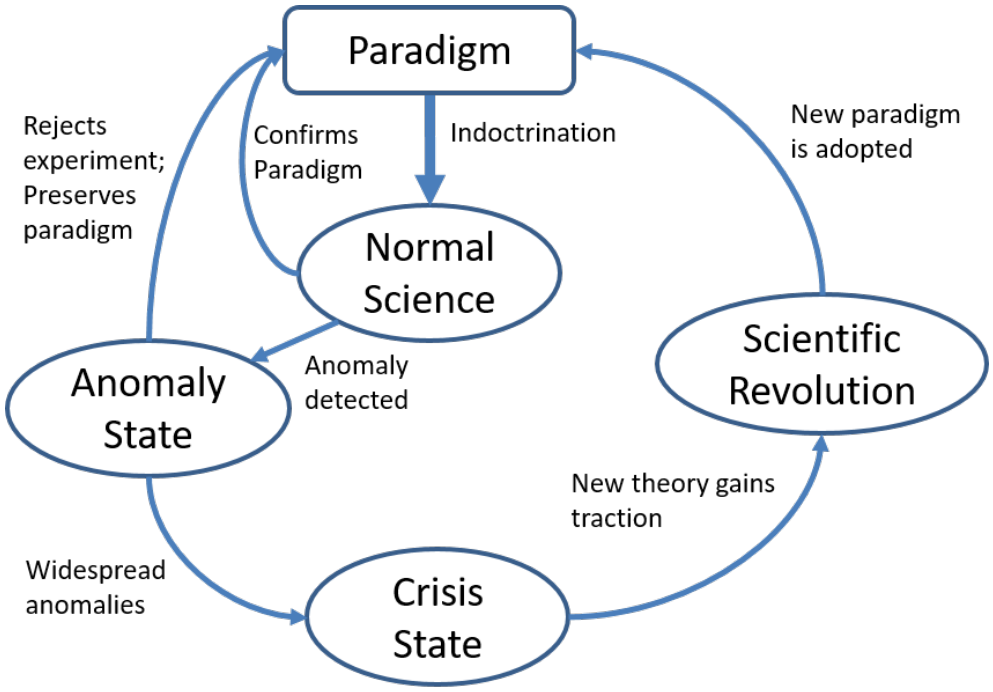

Figure 6.1: **Flow diagram of the Khunian model of scientific revolutions** Simplified flow diagram of the Kuhnian model of scientific revolutions. The status-quo of the day is a paradigm, that through indoctrination (education) creates a state of "normal science" where the goal of research is to confirm the paradigm's predictions. When anomalies are detected by an experiment, they throw the scientific field into an "anomaly state". In most cases the experiment itself is put in doubt and rejected, thereby preserving the paradigm. When enough anomalies are detected, the scientific field enters a state of "crisis, in which the current paradigm is known to be incomplete/wrong, and it is not until an alternative theory emerges that the scientific field enters the state of "scientific revolution. Once the new theory is accepted by the community, it becomes the new paradigm, and the cycle starts again.

within the community, and can explain both past observations and current anomalies (or most of them), the scientific community will move from the state of crisis to a state of scientific revolution that will culminate with the widely spread adoption of a new paradigm, and with that the closing of this circular model. The state of crisis and scientific revolution, as well as the characteristic times spent in each will correlate with the age of the main actors in the community. In other words, scientists that have lived longer within a paradigm will be less likely to be convinced that it is wrong, whereas scientists that have lived a significant portion of their career in a state of crisis will be more likely to adopt a new paradigm [153]. Within the model, Kuhn's notion of scientific progress entails the repetition of this cycle to create new paradigms that continue to provide more accurate descriptions of the natural world. Whether progress is perceived as an approximation to the truth, or just an approximation to reality is not relevant for this model.

This model can be applied to cases in history. For example, it is well suited to describe the change of paradigm from the Ptolemaic model to the Copernican/Keplerian model of planetary motion [152]. The paradigm up until the 16^{th} century was represented by the earth-centric model developed by Ptolomeo around -200B.C. and modified during the following more than 1500 years to fit experimental observations. When Copernicus presented his idea of a heliocentric model, the field of astronomy was already in a state of crisis, created by the failure of the Ptolemaic system to describe the length of a calendar year accurately and to respond satisfactorily to an increasing number of anomalies generated by more precise observations. As Kuhn puts it: "astronomy's complexity was increasing far more rapidly than its accuracy and that a discrepancy corrected in one place was likely to show up in another" [152]p80. The idea of a heliocentric calendar was not new; the idea of heliocentric model and elliptical trajectories had already been developed around 400 A.C. by Hypatia in Alexandria (another forgotten female scientist), but it was not until the field was in crisis that it was receptive to these new theories that became the new paradigm. This paradigm was itself replaced by newer paradigms, with the current paradigm supporting the Big Bang at the center of the Universe.

The Kuhnian model is a very useful tool to summarize in a concise and structured model the way that the evolution of scientific knowledge takes place. It provides a much needed model to counteract the commonly stated notion that scientific endeavor is a linear, cumulative process. Moreover, it provides the space to include the very important social dynamics of scientific activities, and the role of social norms, power structures and indoctrination. As explored in [153], social norms play a crucial role in scientific activities and dictate the flow through the Kuhnian model. For example, indoctrination through education will bias scientists against recognizing anomalies and doubting the current paradigm. Moreover, the acceptance of the new paradigm very often necessitates a reeducation of the scientists involved, which sometimes implies that a new paradigm cannot be successfully adopted until powerful resistors to the change are convinced or die. Observations alone cannot create a successful scientific revolution, and very often we see in historical paradigm changes that took more than a generation to be adopted because of social norms, even though the observations were available. For example, Albert Einstein's resistance to Quantum Mechanics delayed its acceptance as the new (and current) paradigm.

More models have built on the ideas presented by this model, but it still captures the main complexities, the non-linearity, the social norms without being exceedingly complex. It is quite impressive how it can still be applied to recent history and even current events. For example, in 1998 there was a paradigm shift in cosmology, when the supernova cosmology project and the high-z supernova search team independently published results that contradicted the paradigm that the universe was slowing down its expansion [154]. In the course of less than 10 years, the field of cosmology went through an anomaly state, crisis, scientific revolution, and a new paradigm. Now that the accelerated expansion of the universe is an accepted result of observational astronomy, and dark matter and dark energy have been detected indirectly in our universe, the current paradigm states that dark energy is causing the accelerated rate of expansion of the universe. One could say that this new paradigm created a state of crisis for high energy physics, which is looking for alternatives to the standard model that could capture dark matter and dark energy.

In my personal research, I have experienced a full cycle through this model in the community of nanoscale thermal transport. As an actor in that cycle, I was very aware of the social norms that govern "progress" in a field. I have also been aware of my own attachment to paradigms, that makes me doubt experimental results that are outliers in a field. At the same time, I have also observed that today, only surprising and anomalous results get published in high impact journals. It seems to me that this last observation should be added to the Kuhnian model. In the original model anomalous discoveries are modeled as rare and unwanted events. The reality today is completely the opposite. There is a craving for crisis and anomalies, that sometimes blurs the boundaries between the states first proposed by Kuhn.

Of course the Kuhnian model it is not able to describe all of the scientific revolutions that have happened, and certainly will fail in the future. It also doesn't address the topic of the science to technology pipeline. Nevertheless, it is a valuable approximation that could be used cautiously to analyze current states of scientific fields and I think it should be more widely used to teach young scientists and engineers at an early stage the non-linearity and complexity of the scientific endeavor. This would help dispel the linear model for science and technology while still providing a simple enough model that can help policy makers understand (of course in a superficial way) the state of a scientific field. Furthermore, this can be used to argue for investment in incremental research or for more unknown novel experiments. This raises questions about how investments in research and development should be made, and what metrics can be used to appropriately track the progress and success of this research.

6.2 Attempting to engineer innovation: the DOE innovation hubs

6.2.1 Introduction

The current global energy crisis exists at the nexus of diverse economic, political, social, and environmental challenges and interests. Social approaches to address the "energy crisis" have found that inducing behavior changes in populations and entities are very difficult and potentially

not sufficient to avoid a large-scale disaster [155]. Finding alternative approaches is necessary, but solutions may lie in technologies and knowledge that are not ready or that do not exist today. Because of this, investment in innovative research is key to solving the current energy crisis. More efficient fuels, less waste of energy and resources, and safer energy sources are just a few target goals that would provide relief to the energy crisis. But how to foster a faster development of unknown technologies is still a complex and mysterious question. Furthermore, private investment in Research & Development (R&D) in energy related areas has been in decline in the past few decades [156], forcing the public establishment to take the first steps. In this section I will focus on one of those initiatives: the US Department of Energy (DOE) HUBs of innovation.

The science of science policy is still a relatively new discipline (some would say art) [157, 151] that aims to understand how to better invest in science and technology R&D. For each unique circumstance there is no manual or past success that can completely drive action. As discussed in the previous section, the linear model of science and technology [151] has become a widespread illusion that depicts the R&D spectrum as a pipeline, going through the stages of basic science, applied research, engineering technologies, and market deployment. Although some situations can be found to agree partially with the linear model, the bridge between scientific knowledge and technology development is far from simple and linear.

Given the magnitude of the current energy crisis, the US DOE launched a new set of funding mechanisms to accelerate scientific and technological breakthroughs in energy related areas. In an effort to maximize the probabilities of success, this suite of programs attempts to cover the entire R&D spectrum with a variety of complimentary approaches. Each one of the three new modalities can be classified with respect to the type of challenge it addresses.

For known scientific challenges, identified with the help of the scientific community, a funding mechanism similar to that of the Engineering Research Centers or the National Science Foundation's Physics Frontier Centers was designed and implemented. The Energy Frontier Research Centers (EFRCs) consist of multi-PI investigator academic grants around a specific scientific problem. This funding modality, within the Kuhnian model, would correspond to a "normal science" approach to

the problem, in which scientists continue to work within known paradigms and gain incremental precision and understanding.

For the development of unknown transformational technologies that could come from academic or non-academic actors, a funding approach is employed that is modeled after the relatively successful Defense Advanced Research Projects Agency (DARPA) program [155]. A small group of people with high decision-making flexibility "hunt" and help develop new technologies that do not fall under the radar of classic incremental research mechanisms. In the Kuhnian model, these would be research projects that aim at detecting major anomalies, as well as proposing new theories for fields in "crisis state".

For the research and development of technologies around key energy topics, a new funding construct was proposed: the Energy Innovation Hub (HUB). Modeled partially on the Manhattan Project and Bell Labs structures, this model was proposed by then Secretary of Energy Steve Chu in order to accelerate the development of new solutions to the energy crisis. The HUBs are substantially different from any previous funding mechanism and recognize the non-linearity of the scientific and technological endeavor. This funding modality is not captured by the Kuhnian model, as it aims to bridge another gap: the one going from scientific progress to industrial applications.

These new efforts operate in addition to the already established funding programs and organizations within the DOE; however, the scope of these new mechanisms are different, as their goal is to solve a specific set of problems related to the energy crisis. Therefore, they do not represent permanent research constructs, but rather accelerated sprints. This situation is not unheard of, and is often compared to war-related efforts, but the specifics on how to properly manage these constructs under present circumstances is not well understood. The energy crisis is very broad and it is not defined by a finite set of problems that can support the design of a unique roadmap. This situation makes this crisis even more challenging, and if successful, this new funding construct could provide a very powerful framework for the future.

More than five years have passed since the start of these programs (2010), the Secretary of Energy has changed, the EFRCs are going through the closing of the first cycle, the Hubs are

past the midpoint of the first cycle, and ARPA-E is looking at expanding its budget. This is an interesting moment to assess the performance of these different funding mechanisms. Many questions need to be asked: are these funding mechanisms more effective than traditional ones? Do they create unnecessary bureaucracy? Do the current programs implement the new designs? Is this suite of funding mechanisms truly complementary? The remainder of this section will consider these questions as they relate to the HUBs, based on all the material available to me and Prof. Debbie Jin through [158, 159] in 2013. I will start by describing this funding mechanism in more detail, make a quick overview of the existing programs as of 2013, and then discuss the different degrees of success that have been achieved.

6.2.2 What is a HUB?

Energy innovation HUBs allow for multi-disciplinary R&D around a single identified challenge. They were proposed by former Secretary of Energy Steve Chu as a way of bridging the so-called "gap" between science and technological application. The HUB structure is modeled after the Manhattan Project and Bell Labs among a few others, wherein a competent inter-disciplinary team works together with high funding flexibility and a clear goal in mind. This is an important step taken against the linear model of scientific and technological development, as the bridge between scientific knowledge and technological application is not a well understood and clearly not simple process.

The characteristics that are proper to a HUB are:

(1) High flexibility in administering a central annual budget, providing low time response for funding new promising projects.

(2) Functioning under one location or in a highly connected environment to enhance communication between specialists from different disciplines.

(3) Highly competent multi-disciplinary team.

(4) Led by an institution with strong scientific leadership.

HUB characteristics	Associated challenge
High autonomy in internal funding allocation	-High dependence on a strong leader. -Dynamic administrative structure.
Attracting a multi-disciplinary team of highly skilled specialists	-Temporal entities, give no job stability. -If former researchers of member institutions, need to give up their former activities.
One roof physical design	-Difficulty of convincing team members to move to a single location. -No new building infrastructure can be created.
Highly connected physical design	-Communication technology does not replace physical presence.
Collaboration of several institutions	Administrative challenge.
Having a clear reachable 5 year goal	Defining both reachable and ambitious goals. is difficult

Table 6.1: **Different inherent challenges to the characteristics of a HUB funding mechanism**

(5) A strong organization, clear plans, and strong decision-making leader.

A Hub is meant to enhance the pace at which both scientific progress and technological development are achieved, by enhancing communication, providing resources, and identifying a common, pressing goal for a highly competent team. However, it is a temporal construct, as once the goal is achieved the HUB ceases to exist. Therefore, the funding cannot be used to create physical infrastructure. Table 6.1 lists a series of identified challenges that are inherent to the HUB funding mechanism.

The HUB funding mechanism is a way of taking advantage of already existing scientific facilities in the country, by "borrowing" both facilities and researchers towards a common goal with high resources and enhanced internal communication for a finite amount of time. The topics that can benefit from a HUB structure are problems that are mature enough to presume their possible application, but also challenging enough so that the large investment of resources can be justified.

6.2.3 What HUBs exist today?

Initially eight HUBs were proposed in 2009 for fiscal year 2010 by Secretary Steve Chu's team. However, only three of them were initially funded by Congress with a fixed yearly budget of 25 Million dollars per year. The three HUBs funded in the FY2010 operated with the following final simplified goals [158]:

- Fuel from Sunlight (JCAP): Produce affordable, durable, and efcient solar cell that generates hydrogen fuel from sunlight and water.
- Energy Efficient Building System Design (EEB Hub): Improve energy efficiency of buildings in the Philadelphia metropolitan area by 20%.
- Modeling and Simulation for Nuclear Reactors (CASL): Create detailed 3D simulations of existing nuclear reactors to enable utilities to improve efficiency and safety.

Subsequently two more HUBs were awarded funding for the first cycle in FY2012:

- Batteries and Energy Storage (JCESR): Develop a battery that holds five times as much energy as a standard lithium ion battery at one-fifth the cost.
- Critical Materials HUB: Head off shortages of key elements such as rare earth metals by finding replacements and better means of extraction and recycling.

The challenges addressed by these five HUBs are very different, both in their breadth as well as their location on the spectrum of research and development. Additionally, if successful, their impact is difficult to assess. The JCAP, JCESR and critical materials HUBs are working within topics where the basic science fundamentals are still yet to be uncovered, but all three have broad potential applications. CASL, on the other hand, has a very close collaboration with a particular industry and a precise goal that can be achieved with existing technologies, but the implementation of this technology is challenging. Finally, the EEB HUB is trying to prove the

feasibility and economic advantages of existing technologies. Here the challenge lies within aspects of market deployment, but not in R&D.

The existing HUBs do not follow the "under one roof" design, but are all run by a group of institutions. The composition of each group is very diverse, usually mixing academic institutions and national labs, but sometimes also industry partners. As dynamism in the project management is an inherent part of this funding mechanism, each HUB has its own self-defined milestones that allow for internal decision making but do not provide global or universal metrics.

The novelty of the organization makes it inherently difficult to measure success in the HUBs. Of course ultimate success would be to solve the assigned challenge, producing a game-changing technology solution to a particular challenge of the energy crisis. But how should we measure partial success or failure? On the basis of what information should the renewal of the 5-year grant be made?

The uncertainty about the feasibility of a deliverable or even what the deliverable is makes it inherently difficult to measure planned progress in a quantitative way. Nevertheless, the DOE monitors the progress based on several non-quantitative metrics and peer review processes within the HUBs, DOE, or even external to both.

6.2.4 Discussion and conclusions

For each of the initial three HUBs, the DOE has held two peer review processes, the most recent of which was held in 2013. These reviews produced recommendations that have to be taken into account by the HUBs leaders. In 2012 the DOE also produced a report to congress on the status of each of the initial three HUBs in order to secure funding.

In 2013-2014, the current Secretary of Energy asked for a task force consisting of non-DOE affiliated specialists to be in charge of evaluating the suite of funding mechanisms, including EFRCs, BRCs, HUBs and ARPA-E. The document produced by this task force after reviewing the existent internal reports and reviews, as well as meeting with HUB members and others, was made public in March 2014.

The 2014 task force report makes recommendations for the HUBs similar to those made in previous reviews, but it also sheds light on actions that have been taken since previous reports recommendations were communicated in 2012 and 2013. The main recommendations and comments that can be found in this report are the following:

- Some challenges might not be large enough to require a HUB construct.
- Metrics and administration of different HUBs are not always uniform across DOE.
- The HUB construct is not appropriate for pure deployment or for long time horizon projects.
- Best project management practices are not shared, and a lot of resources seem to be spent building administrative structures in each of the HUBs separately, with different degrees of success
- The choice of topics should include input from the Research and Development community.
- Multiple HUBs on a single topic might be beneficiary.
- unified HUB-HUB and HUB-DOE board is critical to avoid miscommunication and enhance best practices sharing.
- HUBs should act as centers of knowledge of their particular topic and interact more with EFRCs and ARPA-E.

These comments and the now effective "retirement of the EEB HUB is a clear sign that the HUB construct is not a universal formula that can be applied to any problem. The EEB HUB was officially defunded in 2014, but the project is still active under the administration of Rutgers University. Nonetheless, the remaining HUBs seem to be doing well and hopefully will be successful. Most of the comments have positively influenced the remaining HUBs, particularly the high level administration HUBs.

But are these comments enough to help the HUBs achieve their goal? Are they really a more efficient construct than traditional funding mechanisms? It is difficult to know before seeing

the long term results, but even then it will be difficult to assess. Still, for appropriate topics, the HUB structure can offer key advantages over the traditional funding mechanism. One of the most valuable lessons learned from this first review is that defining topics that are a good match for a HUB structure is key for its success. In particular, input from the R&D community is needed in order to identify appropriate HUB research topics. Another lesson is that the renewal process of HUBs should apply the same principles that are used in each HUB for initial funding. More resources should be allocated to potentially successful projects, and projects that are not progressing at the pace needed to be part of a HUB should be moved to another funding modality.

More specific lessons have to be learned in the years to come, but more generally, the underlying problem that the HUB construct addresses is the lack of flexibility and quick decision making of traditional funding mechanisms as well as a lack of communication across projects and agencies. This is a problem that still exists across agencies and organizations and needs to be addressed in order to improve the performance of publicly funded R&D. The internal offices in DOE need to have better communication, administrative best practices and structures need to be shared and even standardized in order to use as few resources as possible on administering the resources. Perhaps the HUB experience will serve as a first step in revising some of the more traditional forms of funding, in particular the funding for large research centers such as the DOE national labs.

6.3 Accountability and reporting of the investment in R&D in the America Recovery and Reinvestment Act of 2009

6.3.1 Introduction

As a reaction to the 2008 economic recession, the US government, supported by Congress, passed what is known as the American Recovery and Reinvestment Act of 2009 (ARRA). This bill approved an additional 787 billion dollars (later expanded to 840 billion in 2012) to be appropriated by different agencies and other recipients to help relieve the economy. In this section, I present the main characteristics of ARRA towards traditional R&D organizations, the metrics used to measure

its impact and the results of using these metrics. The level of funding from ARRA to R&D is significant. For example, the ARRA funds destined for the National Science Foundation (NSF) increased their annual budget by 30%. The goals stated in the bill are [160]:

- To preserve and create jobs and promote economic recovery.
- To assist those most impacted by the recession.
- To provide investments needed to increase economic efficiency by spurring technological advances in science and health.
- To invest in transportation, environmental protection, and other infrastructure that will provide long-term economic benefits.
- To stabilize State and local government budgets, in order to minimize and avoid reductions in essential services and counterproductive state and local tax increases.

However, the bill also states that transparency and accountability are a priority. The more general goals are more concisely stated in the official website [161]:

(1) Create new jobs and save existing ones.

(2) Spur economic activity and invest in long-term growth.

(3) Foster unprecedented levels of accountability and transparency in government spending.

This bill traverses all fields and most of the country, as the spending breakdown show in Fig. 6.2 and Fig. 6.4. The focus of this section will be on discussing the metrics used to follow the agencies that received funding directed to Research and Development (R&D). This only accounts for a little more than $14 Billion of the original $784B, but provides an exceptional opportunity to study R&D public funding accountability [157]. Through this section I will focus on reporting and accountability (the third goal of the bill) in the case of R&D funding by ARRA.

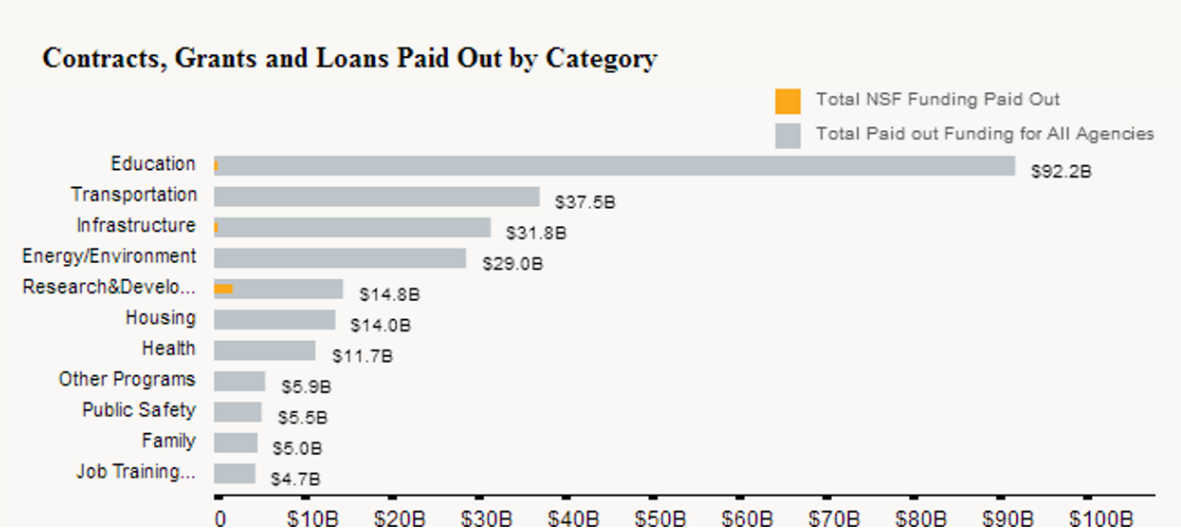

Figure 6.2: **Spectrum of investment by ARRA by areas** spectrum of investment by ARRA by areas, in yellow, the funds received by the NSF [161]

Reporting accurate and helpful metrics for public investment in R&D is an ongoing challenge around the world [162]. A metric is an indicator, that is built on top of data and that is representative of a property (desired or not). For example, in order to measure the productivity of a research institution, the number of papers published could be used as a metric. But this metric may be too coarse, and might not appropriately represent the productivity of an institution. In contrast, a metric based on the number of papers published per researcher, by areas could be more useful. The definition of metrics is a challenging task that often has large implications. In order to judge an investment in a quantitative way, metrics that measure the quality of the outcome have to be developed. Therefore, policy makers are often tempted to do the same with R&D investments even though the metrics used might not be the appropriate ones. The mandate to present accountability and transparency for ARRA created new metrics and visual analytics, which are the focus of this section. First, I will introduce the ARRA bill, its requirements for Accountability and Transparency and the metrics and visual analytics involved. Second I will present an overview of the STAR metrics project developed by the R&D community to address the ARRA mandates. Last I will discuss the results of using these metrics on R&D funding by ARRA.

6.3.2 ARRA and investment in research & development

In order to follow the initial commitment to R&D in the ARRA bill, I focused on the main recipients of this funding. As showed in Figure 2, the main recipients are NSF ($2.1B), NIH ($8.4B) and DOE ($2.6B), taking 87% of the R&D funds reported on April 2013. NIH and DOE also have a significant amount of funding directed to areas other than R&D, but that funding is out of the scope of this section.

The bill covering more than $800B in funding is quite long, but the instructions for the use of the allocated funds is segregated by agencies, making funds for R&D very easy to find. The rather general instructions for NSF and DOE include the following [160]: NSF: RESEARCH AND RELATED ACTIVITIES

For an additional amount for “Research and Related Activities”, $2,500,000,000: Provided, That

[-] Research & Development / Science	$14,841,638,405
National Science Foundation-Research and Related Activities, Recovery Act	$2,110,338,346
Department of Energy-Office of Science-Science Recovery	$1,502,082,007
HHS-National Institutes of Health-National Center for Research Resources, Recovery	$1,256,694,773
HHS-National Institutes of Health-National Cancer Institute	$1,087,898,244
HHS-National Institutes of Health-National Institute of Allergy and Infectious Diseases	$1,052,274,242
Department of Energy-Assistant Secretary for Fossil Energy-Fossil Energy Research and Development	$984,651,913
HHS-National Institutes of Health-National Heart, Lung and Blood Institute	$747,468,822
HHS-Agency for Healthcare Research and Quality-Healthcare Research and Quality, Recovery	$539,494,640
HHS-National Institutes of Health-National Institute of General Medical Sciences	$493,006,539
HHS-National Institutes of Health-National Institute of Diabetes and Digestive and Kidney Diseases	$427,919,274

Figure 6.3: **List of ARRA recipients of more than 400 Million dollars for Research and Development** [161]

$300,000,000 shall be available solely for the Major Research Instrumentation program and $200,000,000 shall be for activities authorized by title II of Public Law 100570 for academic research facilities modernization. DOE: FOSSIL ENERGY RESEARCH AND DEVELOPMENT
For an additional amount for "Fossil Energy Research and Development", $3,400,000,000.
SCIENCE
For an additional amount for "Science", $1,600,000,000.

The generality of these statements concerning science and R&D funding can be surprising at first glance. But Congress cannot micromanage every single operation that is performed with taxpayers money. Although instructions for other areas are slightly more specific, it is mainly left to the agencies (the specialists on every area) to decide how the money is spent. The ARRA operation is an enormous and nationwide operation, creating thousands of jobs and involving most of the government agencies, as illustrated in Fig. 6.4. But how can the congress ensure that the goal to "Foster unprecedented levels of accountability and transparency in government spending" will be met? That is where reporting comes into play. By demanding a periodic report on specific metrics, the government can monitor agencies performance and report it to the general public. A committee is also put in place by the bill to oversee the whole operation and the data will be available on the recovery.org site.

6.3.3 Metrics used in ARRA funding reports: the "Jobs Accountability Act"

This is described on section XV of the bill "Accountability and Transparency." Section A describes the process for recipients and the reports expected; section B puts in place the overseeing board. In section A, referred to as the "Jobs Accountability Act", the specified metrics are [160]:

(1) The total amount of recovery funds received from that agency

(2) The amount of recovery funds received that were expended or obligated to projects or activities; and a detailed list of all projects or activities for which recovery funds were expended or obligated, including

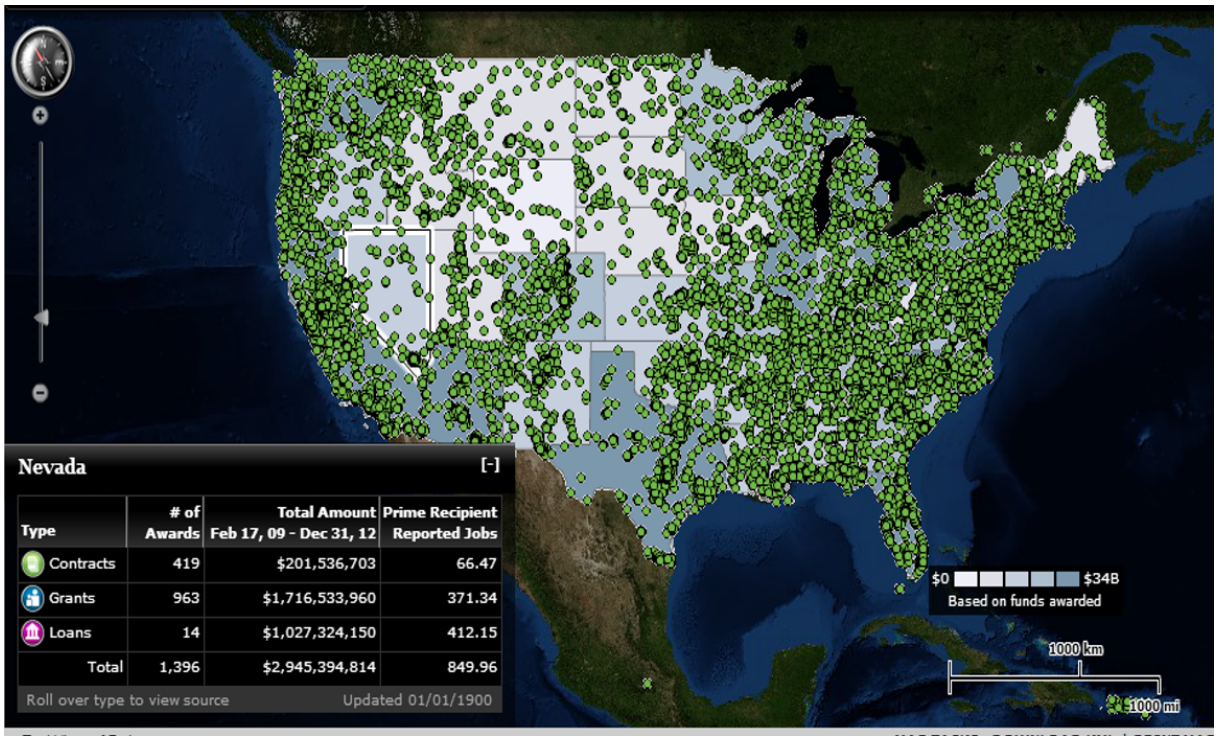

Figure 6.4: **Map of the US with the physical location of grant recipients of ARRA** smap of the US with the physical location of grant recipients of ARRA funds represented by green dots [161]

(a) the name of the project or activity;

(b) A description of the project or activity;

(c) An evaluation of the completion status of the project or activity;

(d) An estimate of the number of jobs created and the number of jobs retained by the project or activity; and

(e) For infrastructure investments made by State and local governments, the purpose, total cost, and rationale of the agency for funding the infrastructure investment with funds made available under this Act, and name of the person to contact at the agency if there are concerns with the infrastructure investment.

From this enumeration it is worth highlighting three main metrics used to evaluate recipients of funds: 1) dollars received, 2) projects completion status, and 3) jobs created. The goal is that the dollars go to the agency, are then allocated to different projects, and that the completed projects produce jobs. There are also other metrics, such as geographical metrics (where the project is located physically) to allow better visualization of the data.

These metrics seem to directly monitor the goal to "create new jobs and save existing ones." But, is the amount of jobs created or retained a good way to measure R&D investment? Based on the current work around the subject of science policy by J. Lane, J. Marburguer, R. Pielke Jr and others ([157, 163, 162, 164, 151]) this metric falls short [164]: "This approach functionally equates the impact of science to the impact of building a football stadium or an airport: the impact is derived from the demand side, and depends on the amount of spending on bricks and mortar and workers." Nonetheless, ARRA was a specific out of cycle package that aimed to minimize the damage of the economic recession and reverse it. Therefore, it could be argued that since its goals are purely economic, its metrics should be of purely economic outcomes. This is a great example of the power of metrics. By demanding that job creation is a priority, it forces agencies of different areas to focus on this aspect when designing their policies, rather than considering other potential uses of the funds. By investing in most of the government agencies, the bill also makes sure that

the money is distributed across the country without having to specifically address the geographical destination of the funding. The metrics gathered from the recipient agencies are then compiled and made available to the public through different visual analytical tools (maps, graphs, pie charts, etc) on any combination of the following variables: jobs created, money awarded, geographical location, area (Education, R&D, etc), projects name, projects completion rates(0%-50%,50%-100%,100%). These are the metrics that ARRA gathers from its recipients, and they are the metrics presented to the general public for accountability. But what properties do these "metrics" represent? Is this data enough to have a realistic estimate of the economic impact of the ARRA investments?

For the overall impact, the Council of Economic Advisers produces a report every quarter [165]. However, this report is based on other metrics (Real GDP, projections of non-ARRA scenarios) and although it does reports the number of jobs produced it does specify that:

"[] evaluating the impact of countercyclical macroeconomic policy is inherently difficult because we do not observe what would have happened to the economy in the absence of policy." And: "The Recovery Act was designed to be temporary. The amount of stimulus outlays and tax reductions has begun to decline and, as discussed in previous reports, as it does so, the impact on the level of GDP and employment will lessen over time." That shows a consensus around the fact that measuring only the job creation is not a sufficient metric to judge the effects of public investment in different areas, even only from the economic point of view. However, it is frustrating that "jobs created" became the metric that guides the policy and the agencies actions. This is probably related to the fact that it is without doubt a very powerful quantity to show to the general public. "Jobs created" is a metric that everybody can relate to; it is also a relatively fast goal to obtain. But, it may be more important to ask: Are the jobs temporary or long-term positions? How are salaries spread across the country? How many are part-time versus full-time? Those are question that cannot be answered with the current metrics, and we might never know. In this section, I will analyze the impact of using "jobs created" as the main metric for measuring ARRA funding success.

6.3.4 Quantitative metrics for R&D investment

In general, R&D in the US benefits from a positive public perception. It is a widely accepted fact in the US that the national economy (and international stature of the country) has been driven by innovation, science and technological advances. Many times, justification for investment in R&D has come from anecdotes, and post-war perception of the linear model, where investment in fundamental research will lead to technological breakthrough that will generate economic growth and societal benefits. But the scientific endeavor is neither linear nor well understood by the scientific community and the policy making community. However, there are very few quantitative long term data sets that attempt to document the return on investment in R&D. In general, advocates for R&D investment argue that economic metrics that try to simplify the investment in R&D (using the linear model for technology development for example) will bring confusion and harm, rather than guide policy. This in contrast with other policy areas, like education or labor, where quantitative metrics are a key part of the decision making and gathering metrics is built into the policies (such as student retention, standardize exam scores, etc). More recently, there have been several efforts to generate certain quantitative metrics for R&D public investment in an attempt to guide policy makers and be more transparent with the general public in a simple way. The lack of simple and direct metrics of outcomes (like full-time jobs created for labor policies, or the decrease of newborns mortality rate for health policies) makes it very hard to provide answers to policy makers that want to approach the problem of public investment from a free market perspective. The concept of public value has been proposed [166], but is not specific enough to provide value for policy makers and is not widely used. As pointed out in [167], understanding the decision making process around science policy is crucial for metric design. Thus, the formation of metrics presents an opportunity and a need for social sciences and natural sciences to work together [162].

In her article to urge the scientific community to contribute to a more systematic and scientific approach to scientific outcome metrics [162], J. Lane exposes the lack of national databases on grant

recipients and reports across all sciences. She also contrasts the US system (or lack of system) with the Brazilian Lattes Database that allows the sharing of data across Brazils 1.6 Million researchers. The lack of an infrastructure in the US to hold, gather and provide data on R&D investment makes it impossible to create more appropriate metrics that would be used by policy makers in the utopia world where policy decisions are made based on rationality and evidence. If there is no data, there is no possibility to create evidence, thus leaving policy makers no other option but to base their decisions on the metrics available: the ones created by other fields, like labor policy or construction of public infrastructure.

The identification of this necessity is the main driver of the STAR metrics project. The US is currently using 17 science agencies that have 17 different data silos, with different identifiers, and different reporting structures [164]. This is the result of having the systems built from the administrative point of view of each agency rather the nation as a whole. Thus the US R&D community needs to take the basic step of unifying its databases and standardize the data gathering, this is a need agreed by the majority of the community as was seen in a workshop designed to roll out the roadmap for federal investments where 94% of the participants were in favor of creating a unique database for federal funding [162].

This task might seem easy to define. However, decisions regarding what data should be gathered, how it should be formatted, how much time it will require from researchers and who can have access to it, are not trivial questions. With ARRA and its $14+ Billions that require "unprecedented levels of accountability and transparency", the opportunity to improve the infrastructure is clear.

6.3.5 Measuring the impact of ARRA in R&D using STAR metrics

STAR metrics is a federal and university partnership to document the outcomes of science investments to the public. It is an Office for Science and Technology Policy (OSTP) initiative partnering with NIH, NSF, DOE, and EPA that is divided into two main phases [168].

6.3.5.1 Phase I: the workforce

This phase corresponds to laying out the base for future data gathering. By taking advantage of the ARRA demands of reporting, the idea was to build a single data base for the the R&D community. During this first phase a partnership with the Federal Demonstration Partnership (FDP) was developed in a series of workshops and meetings. In this process a standard way of gathering the data electronically to measure the impact of science spending on job creation was developed. The formats are now available for the different levels of R&D structures and not only consist of gathering the data, but also allow the users to browse through the national community data. This first phase addresses ARRA demands for reporting the "jobs created" metric, and presents an incentive for researchers to participate, as it helps them support the employment calculations for ARRA [169]. It presents the individual with a structured way to calculate the direct employments generated by an ARRA award, but also employments generated by:

- Purchases made from Vendors: The vendor DUNS number is used to derive the geographic location. Economic Census data are used to generate estimates of the amount of salaries paid as a result of grant revenues earned by the Vendor. This in turn is divided by the average earnings of the workers in that industry and to produce the employment estimates.
- Sub-awards: Calculated in the same way as the previous item.
- Overhead: Estimates will be calculated using information from each research institution's indirect cost proposal.

By calculating the "jobs created" metric in this way, STAR metrics captures an improved, though still incomplete, picture of job creation in R&D investment, as shown in Fig. 6.5. But STAR metrics is more than just this. Supporting the employment calculations for reports to ARRA is just a by-product of its process. This first phase, with its ARRA-linked incentives allows the creation and consolidation of a community of R&D institutions that are now using the tool both for reporting data and for data usage. On the slides of the update on STAR Metrics on Jan. 2012 more than

85 institutions are reported to be using the tools [14] and it is considered a collective effort by six agencies participating: OSTP, NIH, NSF, EPA, DOE and USDA. As stated previously and in most references, supported jobs is not the ideal metric to measure the outcome of investment in R&D, in [163]: "[...]the appropriate outcomes of scientific investments are the creation, dissemination and adoption of knowledge." But, how do we measure the creation, dissemination and adoption of knowledge? That is the purpose of phase 2.

6.3.5.2 Phase II: lets get creative

Phase 1 of the STAR Metrics project can be seen as a consolidation phase. Only the institutions having joined phase 1 will participate in phase 2. This phase primary goal is [169]: " Developing measures of the impact of federal science investment on scientific knowledge (using metrics such as publications and citations), social outcomes (e.g. health outcomes measures and environmental impact factors), workforce outcomes (e.g. student mobility and employment), and economic growth (e.g. tracing patents, new company start-ups and other measures)." This phase is at the center of the efforts around the Science of Science Policy. It is still not in development officially, and no metrics have been released. However, it is expected to be a long process as there are many entities involved [170].

6.3.6 Summary of public results

Phase 1 of STAR Metrics has been running since 2010 and has allowed institutions to track their Research according to FTEs (full time employments) and other parameters (like geographical location). As shown in Fig. 6.5, in terms of jobs created by agency on the Oct1-Dec31 2012 quarter, DOE comes 1st, NIH comes 5th, and NSF 10th. Since DOE and NIH also have a majority of non-R&D funding this might not surprise, but NSF used more than 90% of its almost $3B (less than 0.4% of the total ARRA budget) on R&D projects. By just looking at this result, it seems that R&D is a very good investment to produce jobs! This tendency is reproduced almost every quarter of 2010 to 2013. The jobs created by NSF with less than 0.4% of the total budget represents

TOP AGENCIES, AS REPORTED BY RECIPIENTS (OCT 1 - DEC 31, 2012)

Agency Name	Jobs
Department of Energy	22,757.82
Department of Education	19,610.10
Department of Transportation	13,539.76
Department of Agriculture	11,341.64
Department of Health and Human Services	9,912.41
Department of Justice	6,815.09
General Services Administration	5,513.90
Department of Commerce	5,321.25
Department of Housing and Urban Development	5,049.65
National Science Foundation	3,344.48
Department of Homeland Security	2,259.06
Department of Defense (except military departments)	1,530.46
Department of Labor	1,461.19
Corps of Engineers	1,353.58

Figure 6.5: **Lists for the top agencies on job creation for the oct1-dec31 2012 quarter** [161]

between 0.8% (first quarter, where the Department of Education reported 300.000+ jobs created) to 5% of the total jobs every quarter of 2010 to 2013.

6.3.7 Discussion and conclusions

The ARRA bill came at a time of economic recession and growing unemployment. Its goals were very clear: create jobs, foster economic growth and be transparent. In this section, I presented an overview of the ARRA bill and the choice of metrics to measure its impact. I discussed the importance of choosing appropriate metrics for a particular policy, and how finding quantitative metrics for public R&D funding has been a challenge. I then present a recent initiative to face that challenge, STAR metrics. I briefly present the goals of the STAR metric program, and its impact on job creation calculation for reporting on ARRA funding. It was very successful in showing high return on investment for R&D agencies, but this is just an illusion. "Jobs created" is not a metric of long term economic growth and definitely not an appropriate metric to measure the success of an R&D project. But as it was chosen as the main ARRA metric, it is what motivated the actions of the fund recipients. What is transparent to the citizen is the geographical allocation of the money, but it is impossible to know how it was used.

However, the economy did recover, and nobody can dispute that the bill had an influence. Sadly the opportunity to design and test new metrics in order to learn from this crisis was lost. The R&D recipients, through the STAR Metrics project, accomplished a first step towards the generation of standardized measures of R&D investment outcomes. Nevertheless, the STAR Metrics project is not perfect, and seems to be keeping the general public in the dark. The process of creating those metrics has to include economists, social scientists and natural scientists and engineers, but it is crucial that it also includes policy makers, or at least brokers between the scientific community and the policy making world. It is definitely a project that could change the way metrics are defined and it will be vital to the successful establishment of evidence-based policy and a stronger STP field.

6.4 Conclusions and outlook

In this chapter, I have presented a non-linear model for scientific progress and two different cases of science policies and how the outcomes of these policies were measured. These are extracts from a wider body of work that I have built over the past five years, while pursuing a graduate certificate in STP. Based on this analysis, it is evident that most people, both scientists and non-scientists, have a limited understanding of scientific progress. This is compounded by the fact that measurements used to judge the outcome of scientific activities are often not connected to reality. The linear model of scientific research is just a myth built decades of years ago that makes it easy to justify funding certain areas of science, but has no basis on reality. The two examples provided here show how complex it is to design successful science policy, and how even more complicated it is to measure and track its success and consequences. My aim in this chapter is to present a simple and short picture of science and technology policy making and offer three suggestions for the future of this field: 1) Provide a simple way to recognize and visualize the non-linearity of the scientific (and technological development) endeavor, 2) Promote flexibility in the funding modalities and mechanisms (such as the HUB construct or the DARPA construct), and 3) Develop a set of quantitative and qualitative metrics that are tailored to the goals of the policy and that will be gathered and analyzed as the policy unfolds. I am aware that this is an oversimplification, but starting simple might be the key to progress.

Chapter 7

Future opportunities and conclusions

7.1 Conclusions

In this thesis, I have presented how I harnessed the many advantages of table top sources of coherent short wavelength high harmonic generation to design and implement a novel metrology technique that is sensitive to nanoscale dynamics: coherent EUV nanometrology. This tool now allows us to perform ultrafast studies of elastic and thermal transport properties of a large array of materials and nanostructured systems. Coherent EUV nanometrology is one of the only tools that can uncover complex phonon dynamics in nanostructured systems of unprecedented characteristic dimensions. The results and measurements present in my work show more than just a proof-of-principle demonstration of the technique; it shows that coherent EUV nanometrology can make robust and precise measurements of complex materials' properties that impact both fundamental and applied condensed matter physics and material science.

In chapter 2 I presented the experimental and modeling apparatus and methods that are part of coherent EUV nanometrology. In chapter 3, I presented how I used it to probe nanoscale heat dissipation away from periodic 1D-confined nanoscale heat sources of unprecedented size and spacing. This work resulted in the uncovering of a new regime of nanoscale thermal transport: the collectively diffusive regime. In this regime, 1D-confined heat sources that are spaced closer together cool down faster than if spaced farther apart. I also presented our results confirming the predictions of this regime in periodic 1D-confined nanoscale heat sources of same size but different spacing. Further, I presented the results from probing heat dissipation from 2D confined heat

sources showing the same regimes present in the 1D confined heat sources. I showed how this results can be used to develop a new kind of spectroscopy: phonon mean free path spectroscopy. By probing heat dissipation away from 1D- and 2D- confined heat sources, we probe the contributions to the thermal conductivity by different portions of the phonon spectrum of a material. By understanding how the interplay between geometry and heat dissipation efficiency works, we can then reconstruct the phonon spectrum in that material. Using this concept I presented the first proof-of-principle extraction of the phonon MFP spectrum of silicon and sapphire substrates.

In chapter 4, I discussed different modeling and theoretical approaches to nanoscale thermal transport experiments. I then showed the results of my implementation of a linear-Boltzmann Transport Equation (BTE) solver for nanoscale thermal transport in our experimental geometries using first principle calculation results as an input parameter. I showed how the linear-BTE seems to capture part of the effects observed in the experimental results, where the spacing between neighboring heat sources seems to enhance the heat dissipation efficiency. However, it does not fully explain the observed experimental results, therefore suggesting that the geometry itself might be modifying transport properties of the nanostructured system as a whole.

In chapter 5 I presented the success of using coherent EUV nanometrology to characterize the elastic properties of ultra-thin isotropic films. I showed how short wavelength surface acoustic waves that are fully confined within the thin film of interest can be launched, and how that allows for the complete characterization of sub-100nm thin films. I presented the results of the full characterization of a series of low-k thin films, including for the first time, the measurement of the material's Poisson's ratio. The access to Poisson's ratio allowed for the detection of an unexpected behavior of the film's materials, correlated with the fabrication process. By exposing the films to different degrees of hydrogenation, the dielectric constant can be changed. However, this also breaks bonds in materials, lowering the network connectivity. Our measurements show that below a critical value of network connectivity, the material undergoes a transition from brittle to ductile, and the Poisson's ratio is no longer constant but takes values closer to incompressible materials. I

also showed that even without having access to confined SAWs, sub-10nm metallic thin films can be partially characterized and shown to have different elastic properties than their bulk counterparts.

In chapter 6 I presented a non-linear model for scientific progress and two different cases of science policies and how the outcomes of these policies were measured. Based on this analysis, it is evident that most people, both scientists and non-scientists, have a limited understanding of scientific progress. This is compounded by the fact that the metrics used to judge the outcome of scientific activities are often not connected to reality. Using these case scenarios as a motivation, I presented three suggestions that could potentially help science policy making going forward.

In this final chapter, I presented a short list of very exciting new projects and directions. I am confident that as coherent EUV nanometrology is used to probe nanoscale engineered materials and exotic materials, and as it is extended deeper into the nanoscale, it will provide deep insights into fundamental condensed matter physics as well as impact a wide array of technological applications.

7.2 Ongoing and future work

Coherent EUV nanometrology is now a working and powerful technique, but much more can be done to improve the existing experimental setup and to utilize it on new exciting systems. For example, the signal to noise ratio can be further improved by having a shutter that can work at the same repetition rate as the laser system, in a synchronized way. We are currently implementing such an improvement by using a phase-locked chopper system. A further improvement is to be able to perform single shot acquisitions, especially as the brightness of the HHG sources improves. In this section, current efforts that will guide future work of using table-top HHG sources of coherent short wavelength light for uncovering new phonon dynamics are described.

7.2.1 Dynamic nanoscale imaging

In recent years, the field lens-less imaging has made enormous progress [171]. By combining ptycographic coherent diffraction imaging with HHG sources, our research group has been able to provide robust and accurate reconstructions of surfaces of nanostructured systems with $< 1nm$

vertical resolution and $< 40nm$ horizontal revolution. These resolutions are improving every day, including achieving subwavelength resolution on a periodic sample [171]. By combining this technique with our pump-probe experimental setup, we are working towards the first high resolution nanoscale movie. These techniques will offer a powerful new microscopy technique on par with atomic force microscopy in its spatial resolution and with coherent EUV nanometrology in its temporal resolution. It will also facilitate the study of localized dynamics, opening the door for a large quantity of studies and experimental projects that are currently impossible, including performing complementary studies to the results presented in this thesis, by extracting the local elastic and thermal properties of the same interesting systems. This would as well include extracting the elastic properties of highly anisotropic materials and nanostructures, the study of nanoscale thermal transport in complex non-periodic geometries, studies of defect impact on local properties and many, many more. [172].

7.2.2 Measuring complex and engineered materials

As nanofabrication capabilities continue to progress, it is now possible to engineer materials with nanoscale structures. The ability to design material's phononic properties can have potential applications in many technologies, such as high thermal conductivity nanostructures for thermal management in microelectronics, low thermal conductivity materials to both isolate memory cells in hard drives that use heat assisted magnetic recording and enhance thermoelectric efficiency and directional thermal transport for both thermal management applications and thermal logical circuits. Therefor, understanding nanoscale transport is of capital importance in emerging structures such as nanophononic meta materials (NPM) [38] like inverse opal lattices [173], and other systems as well as across interfaces [100] or periodic defects on thin membranes [67]. However, as I have discussed throughout this dissertation, measuring nanoscale thermal and elastic properties is extremely challenging using traditional methods. Now that coherent EUV nanometrology has been developed and demonstrated on relatively simple systems (crystalline substrates, isotropic thin films), it can be used to extract the properties of more complex materials. For example, we are

currently in the process of measuring a series of $100nm$ and $200nm$ thin suspended NPM samples using visible TG excitation and probing in reflection mode with our coherent EUV probe, and will soon be able to extract the lattice thermal conductivity value and compare with predictions from [62]. These measurements can also be extended to study the role of phonon dispersion in vanadium oxides, where phonons could play a key role during the phase transition.

7.2.3 Developing EUV transient grating setup

One of the main difficulties in using the current state of coherent EUV nanometrology is the need to deposit periodic arrays of nanostructures on top of the sample of interest. This is not always simple, and often expensive and time-consuming. Moreover, relying on nanostructured transducers limits the characteristic dimension of excitations we can study. Because of this, we are currently designing and will soon implement an extension of the visible TG excitation technique to the EUV. However, no optics can be used to replicate the simple and elegant $4f$ system in our current setup. Instead, two different HHG beams will be focused on the surface of a sample, and when temporal and spatial overlap is achieved, an interference pattern will be created. This interference will excite the material's surface in a periodic manner, with a spatial periodicity related to the wavelength of the light and angle of incidence of the beams. We are currently planning on using $22ev$ HHG beam driven with $390nm$ short pulses of light in a waveguide filled with Krypton gas, as shown in [174]. This will ensure a high photon flux and a spectral purity needed for a first proof of the principle experiment. Once that capability is achieved, excitation of sub-$60nm$ wavelength SAWs and sub-$30nm$ heat sources will be possible without the need of a patterned transducer, making the characterization of many novel and complex materials not only possible, but also fast. Finally, the technique developed for $22eV$ HHG light is scalable to $42eV$ and even to $98eV$ HHG light sources, making it possible to generate sub-$10nm$ wavelength SAW, which can correspond to exciting specific phonon modes in the acoustic branch of materials individually. This will be the ultimate phonon spectroscopy tool.

Bibliography

[1] "How many transistors have shipped in the world." https://www.forbes.com/sites/jimhandy/2014/05/26/how-many-transistors-have-ever-shipped/#7ea993ea4425. Accessed on May 25th 2017.

[2] M. M. Waldrop, "More than moore," Nature, vol. 530, no. 7589, p. 144, 2016.

[3] S. K. King, H. Simka, D. Herr, H. Akinaga, and M. Garner, "Research updates: The three m's (materials, metrology, and modeling) together pave the path to future nanoelectronic technologies," Applied Physics Letters Materials, vol. 1, p. 040701, 2013.

[4] "wiki commons pictures." https://commons.wikimedia.org/wiki/. Accessed on May 25th 2017.

[5] K. M. Hoogeboom-Pot, J. N. Hernandez-Charpak, X. Gu, T. D. Frazer, E. H. Anderson, W. Chao, R. W. Falcone, R. Yang, M. M. Murnane, H. C. Kapteyn, et al., "A new regime of nanoscale thermal transport: Collective diffusion increases dissipation efficiency," Proceedings of the National Academy of Sciences, vol. 112, no. 16, pp. 4846–4851, 2015.

[6] J. Hernandez-Charpak, T. Frazer, J. Knobloch, K. Hoogeboom-Pot, D. Nardi, W. Chao, L. Jiang, M. Tripp, S. King, H. Kapteyn, et al., "Reliable characterization of materials and nanostructured systems¡¡ 50nm using coherent euv beams," in SPIE Advanced Lithography, pp. 97780I–97780I, International Society for Optics and Photonics, 2016.

[7] J. N. Hernandez-Charpak, K. M. Hoogeboom-Pot, Q. Li, T. D. Frazer, J. L. Knobloch, M. Tripp, S. W. King, E. H. Anderson, W. Chao, M. M. Murnane, et al., "Full characterization of the mechanical properties of 11–50 nm ultrathin films: Influence of network connectivity on the poissons ratio," Nano Letters, 2017.

[8] K. M. Hoogeboom-Pot, E. Turgut, J. N. Hernandez-Charpak, J. M. Shaw, H. C. Kapteyn, M. M. Murnane, and D. Nardi, "Nondestructive measurement of the evolution of layer-specific mechanical properties in sub-10 nm bilayer films," Nano Lett, vol. 16, pp. 4773–4778, 2016.

[9] C. Bodelón, M. Fallah, and J. H. Reynolds, "Temporal resolution for the perception of features and conjunctions," Journal of Neuroscience, vol. 27, no. 4, pp. 725–730, 2007.

[10] T. Popmintchev, M.-C. Chen, D. Popmintchev, P. Arpin, S. Brown, S. Ališauskas, G. Andriukaitis, T. Balčiunas, O. D. Mücke, A. Pugzlys, et al., "Bright coherent ultrahigh harmonics in the kev x-ray regime from mid-infrared femtosecond lasers," Science, vol. 336, no. 6086, pp. 1287–1291, 2012.

[11] C. Chen, Attosecond Light Pulses and Attosecond Electron Dynamics Probed using Angle-Resolved Photoelectron Spectroscopy. PhD thesis, University of Colorado at Boulder, 2017.

[12] "Edgerton digital collection project." `https://github.com/jeanphilippeperaud/Phonon-Code/blob/master/README.md`. Accessed on May 25th 2017.

[13] T. Maiman, "Stimulated optical radiation in ruby," Nature, vol. 187, pp. 493–494, 1960.

[14] N. Bloembergen, "From nanosecond to femtosecond science," Reviews of Modern Physics, vol. 71, no. 2, p. S283, 1999.

[15] A. McPherson, G. Gibson, H. Jara, U. Johann, T. S. Luk, I. McIntyre, K. Boyer, and C. K. Rhodes, "Studies of multiphoton production of vacuum-ultraviolet radiation in the rare gases," JOSA B, vol. 4, no. 4, pp. 595–601, 1987.

[16] J. L. Krause, K. J. Schafer, and K. C. Kulander, "High-order harmonic generation from atoms and ions in the high intensity regime," Physical Review Letters, vol. 68, no. 24, p. 3535, 1992.

[17] P. Corkum, "Plasma perspective on strong field multiphoton ionization," Phys.Rev.Lett., vol. 71, pp. 1994–1997, 1993.

[18] M. Lewenstein, P. Balcou, M. Y. Ivanov, A. Lhuillier, and P. B. Corkum, "Theory of high-harmonic generation by low-frequency laser fields," Physical Review A, vol. 49, no. 3, p. 2117, 1994.

[19] H. C. Kapteyn, M. M. Murnane, and I. P. Christov, "Extreme nonlinear optics: coherent x rays from lasers," Physics Today, vol. 58, no. 3, pp. 39–46, 2005.

[20] A. Rundquist, C. G. Durfee, Z. Chang, C. Herne, S. Backus, M. M. Murnane, and H. C. Kapteyn, "Phase-matched generation of coherent soft x-rays," Science, vol. 280, no. 5368, pp. 1412–1415, 1998.

[21] R. Sandberg, Closing the gap to the diffraction limit: Near wavelength limited tabletop soft x-ray coherent diffractive imaging. PhD thesis, University of Colorado, 2009.

[22] K. M. Hoogeboom-Pot, Uncovering new thermal and mechanical behavior at the nanoscale using coherent extreme ultraviolet light. PhD thesis, University of Colorado at Boulder, 2015.

[23] J. A. Johnson, A. A. Maznev, M. T. Bulsara, E. A. Fitzgerald, T. Harman, S. Calawa, C. Vineis, G. Turner, and K. A. Nelson, "Phase-controlled, heterodyne laser-induced transient grating measurements of thermal transport properties in opaque material," Journal of Applied Physics, vol. 111, no. 2, p. 023503, 2012.

[24] J. A. Rogers, A. A. Maznev, M. J. Banet, and K. A. Nelson, "Optical generation and characterization of acoustic waves in thin films: Fundamentals and applications," Annual Review of Materials Science, vol. 30, no. 1, pp. 117–157, 2000.

[25] E. Hecht, "Optics, 4th," International edition, Addison-Wesley, San Francisco, vol. 3, 2002.

[26] J. Goodman, "Introduction to fourier optics 2nd," Edition (McGraw–Hill, New York, 1996).

[27] F. Banfi, F. Pressacco, B. Revaz, C. Giannetti, D. Nardi, G. Ferrini, and F. Parmigiani, "Ab initio thermodynamics calculation of all-optical time-resolved calorimetry of nanosize systems: Evidence of nanosecond decoupling of electron and phonon temperatures," Physical Review B, vol. 81, no. 15, p. 155426, 2010.

[28] S. Anisimov, B. Kapeliovich, and T. Perelman, "Electron emission from metal surfaces exposed to ultrashort laser pulses," Zh. Eksp. Teor. Fiz, vol. 66, no. 776, pp. 375–7, 1974.

[29] Z. Lin, L. V. Zhigilei, and V. Celli, "Electron-phonon coupling and electron heat capacity of metals under conditions of strong electron-phonon nonequilibrium," Physical Review B, vol. 77, no. 7, p. 075133, 2008.

[30] N. Ashcroft and N. Mermin, Solid State Physics. Cengage Learning, 2011.

[31] R. Tobey, M. Siemens, O. Cohen, M. Murnane, H. Kapteyn, and K. Nelson, "Ultrafast extreme ultraviolet holography: dynamic monitoring of surface deformation," Optics Letters, vol. 32, no. 3, pp. 286–288, 2007.

[32] A. N. Beris and A. J. Giacomin, "$\pi\acute{\alpha}\nu\tau\alpha\ \varepsilon\iota$: Everything flows,," Appl. Rheol, vol. 24, p. 52918, 2014.

[33] M. Asimov, History of Civilizations of Central Asia (vol.4,part-2). History of civilizations of Central Asia, Motilal Banarsidass, 1992.

[34] J. Fourier, Theorie analytique de la chaleur, par M. Fourier. Chez Firmin Didot, père et fils, 1822.

[35] G. Chen, "Nanoscale heat transfer and nanostructured thermoelectrics," Components and Packaging Technologies, IEEE Transactions on, vol. 29, no. 2, pp. 238–246, 2006.

[36] C. Dames and G. Chen, "Thermal conductivity of nanostructured thermoelectric materials," Thermoelectrics Handbook: macro to nano, 2006.

[37] L. Shi, "Thermal and thermoelectric transport in nanostructures and low-dimensional systems," Nanoscale and Microscale Thermophysical Engineering, vol. 16, no. 2, pp. 79–116, 2012.

[38] B. L. Davis and M. I. Hussein, "Thermal characterization of nanoscale phononic crystals using supercell lattice dynamics," AIP Advances, vol. 1, no. 4, pp. 041701–041701, 2011.

[39] P. K. Jain, X. Huang, I. H. El-Sayed, and M. A. El-Sayed, "Noble metals on the nanoscale: optical and photothermal properties and some applications in imaging, sensing, biology, and medicine," Accounts of Chemical Research, vol. 41, no. 12, pp. 1578–1586, 2008.

[40] S. Saha, X. Xiong, P. K. Chakraborty, K. Shameer, R. R. Arvizo, R. A. Kudgus, S. K. D. Dwivedi, M. N. Hossen, E. M. Gillies, J. D. Robertson, et al., "Gold nanoparticle reprograms pancreatic tumor microenvironment and inhibits tumor growth," ACS nano, 2016.

[41] D. Rourke, S. Ahn, A. M. Nardes, J. van de Lagemaat, N. Kopidakis, and W. Park, "Integrated optical and electrical modeling of plasmon-enhanced thin film photovoltaics: A case-study on organic devices," Journal of Applied Physics, vol. 116, no. 11, p. 114510, 2014.

[42] E. Pop, "Energy dissipation and transport in nanoscale devices," Nano Research, vol. 3, no. 3, pp. 147–169, 2010.

[43] A. Balandin, "Nanoscale thermal management," Potentials, IEEE, vol. 21, no. 1, pp. 11–15, 2002.

[44] M. Maldovan, "Narrow low-frequency spectrum and heat management by thermocrystals," Physical Review Letters, vol. 110, no. 2, p. 025902, 2013.

[45] M. E. Siemens, Q. Li, R. Yang, K. A. Nelson, E. H. Anderson, M. M. Murnane, and H. C. Kapteyn, "Quasi-ballistic thermal transport from nanoscale interfaces observed using ultrafast coherent soft x-ray beams," Nature materials, vol. 9, no. 1, pp. 26–30, 2009.

[46] K. T. Regner, D. P. Sellan, Z. Su, C. H. Amon, A. J. McGaughey, and J. A. Malen, "Broadband phonon mean free path contributions to thermal conductivity measured using frequency domain thermoreflectance," Nature Communications, vol. 4, p. 1640, 2013.

[47] A. Minnich, J. Johnson, A. Schmidt, K. Esfarjani, M. Dresselhaus, K. Nelson, and G. Chen, "Thermal conductivity spectroscopy technique to measure phonon mean free paths," Physical Review Letters, vol. 107, no. 9, p. 095901, 2011.

[48] Y. K. Koh and D. G. Cahill, "Frequency dependence of the thermal conductivity of semiconductor alloys," Physical Review B, vol. 76, no. 7, p. 075207, 2007.

[49] J. P. Freedman, J. H. Leach, E. A. Preble, Z. Sitar, R. F. Davis, and J. A. Malen, "Universal phonon mean free path spectra in crystalline semiconductors at high temperature," Scientific Reports, vol. 3, 2013.

[50] G. Chen, Nanoscale Energy Transport and Conversion: A Parallel Treatment of Electrons, Molecules, Phonons, and Photons. MIT-Pappalardo Series in Mechanical Engineering, Oxford University Press, 2005.

[51] P. Giannozzi, S. De Gironcoli, P. Pavone, and S. Baroni, "Ab initio calculation of phonon dispersions in semiconductors," Physical Review B, vol. 43, no. 9, p. 7231, 1991.

[52] I. Maasilta and A. Minnich, "Heat under the microscope," Physics Today, vol. 67, no. 8, p. 27, 2014.

[53] D. G. Cahill, P. V. Braun, G. Chen, D. R. Clarke, S. Fan, K. E. Goodson, P. Keblinski, W. P. King, G. D. Mahan, A. Majumdar, et al., "Nanoscale thermal transport. ii. 2003–2012," Applied Physics Reviews, vol. 1, no. 1, p. 011305, 2014.

[54] T. Luo and G. Chen, "Nanoscale heat transfer–from computation to experiment," Physical Chemistry Chemical Physics, vol. 15, no. 10, pp. 3389–3412, 2013.

[55] E. S. Toberer, L. L. Baranowski, and C. Dames, "Advances in thermal conductivity," Annual Review of Materials Research, vol. 42, pp. 179–209, 2012.

[56] A. Maznev, "Onset of size effect in lattice thermal conductivity of thin films," Journal of Applied Physics, vol. 113, no. 11, pp. 113511–113511, 2013.

[57] A. Joshi and A. Majumdar, "Transient ballistic and diffusive phonon heat transport in thin films," Journal of Applied Physics, vol. 74, no. 1, pp. 31–39, 1993.

[58] J. Cuffe, J. K. Eliason, A. A. Maznev, K. C. Collins, J. A. Johnson, A. Shchepetov, M. Prunnila, J. Ahopelto, C. M. S. Torres, G. Chen, et al., "Reconstructing phonon mean free path contributions to thermal conductivity using nanoscale membranes," arXiv preprint arXiv:1408.6747, 2014.

[59] J. A. Johnson, A. Maznev, J. Cuffe, J. K. Eliason, A. Minnich, T. Kehoe, C. M. S. Torres, G. Chen, and K. A. Nelson, "supplementary information direct measurement of room-temperature nondiffusive thermal transport over micron distances in a silicon membrane," Physical review letters, vol. 110, no. 2, p. 025901, 2013.

[60] J. Cuffe, E. Chavez, A. Shchepetov, P.-O. Chapuis, E. H. El Boudouti, F. Alzina, T. Kehoe, J. Gomis-Bresco, D. Dudek, Y. Pennec, et al., "Phonons in slow motion: dispersion relations in ultrathin si membranes," Nano Letters, vol. 12, no. 7, pp. 3569–3573, 2012.

[61] J. H. Seol, "Thermal and thermoelectric measurements of silicon nanoconstrictions, supported graphene, and indium antimonide nanowires," 2009.

[62] B. L. Davis and M. I. Hussein, "Nanophononic metamaterial: Thermal conductivity reduction by local resonance," Phys. Rev. Lett., vol. 112, p. 055505, Feb 2014.

[63] M. I. Hussein, M. J. Leamy, and M. Ruzzene, "Dynamics of phononic materials and structures: Historical origins, recent progress, and future outlook," Applied Mechanics Reviews, vol. 66, no. 4, p. 040802, 2014.

[64] A. Cleland, D. Schmidt, and C. Yung, "Thermal conductance of nanostructured phononic crystals," Physical Review B, vol. 64, no. 17, p. 172301, 2001.

[65] M. Nomura, J. Nakagawa, K. Sawano, J. Maire, and S. Volz, "Thermal conduction in si and sige phononic crystals explained by phonon mean free path spectrum," Applied Physics Letters, vol. 109, no. 17, p. 173104, 2016.

[66] J. Lim, K. Hippalgaonkar, S. Andrews, A. Majumdar, and P. Yang, "Quantifying surface roughness effects on phonon transport in silicon nanowires," Nano Letters, 2012.

[67] S. Neogi, J. S. Reparaz, L. F. C. Pereira, B. Graczykowski, M. R. Wagner, M. Sledzinska, A. Shchepetov, M. Prunnila, J. Ahopelto, C. M. Sotomayor-Torres, et al., "Tuning thermal transport in ultrathin silicon membranes by surface nanoscale engineering," ACS nano, vol. 9, no. 4, pp. 3820–3828, 2015.

[68] H. Honarvar, L. Yang, and M. I. Hussein, "Thermal transport size effects in silicon membranes featuring nanopillars as local resonators," Applied Physics Letters, vol. 108, p. 263101, 2016.

[69] P. E. Hopkins, "Thermal transport across solid interfaces with nanoscale imperfections: effects of roughness, disorder, dislocations, and bonding on thermal boundary conductance," International Scholarly Research Notices, vol. 2013, 2013.

[70] E. Lee, T. Zhang, T. Yoo, Z. Guo, and T. Luo, "Nanostructures significantly enhance thermal transport across solid interfaces," ACS Applied Materials & Interfaces, 2016.

[71] V. Bahadur, J. Xu, Y. Liu, and T. Fisher, "Thermal resistance of nanowire-plane interfaces," Journal of Heat Transfer, vol. 127, no. 6, pp. 664–668, 2005.

[72] M. D. Losego, M. E. Grady, N. R. Sottos, D. G. Cahill, and P. V. Braun, "Effects of chemical bonding on heat transport across interfaces," Nature Materials, vol. 11, no. 6, pp. 502–506, 2012.

[73] C. A. Polanco, C. B. Saltonstall, P. M. Norris, P. E. Hopkins, and A. W. Ghosh, "Impedance matching of atomic thermal interfaces using primitive block decomposition," Nanoscale and Microscale Thermophysical Engineering, vol. 17, no. 3, pp. 263–279, 2013.

[74] K. Termentzidis, P. Chantrenne, and P. Keblinski, "Nonequilibrium molecular dynamics simulation of the in-plane thermal conductivity of superlattices with rough interfaces," Physical Review B, vol. 79, no. 21, p. 214307, 2009.

[75] T. S. English, J. C. Duda, J. L. Smoyer, D. A. Jordan, P. M. Norris, and L. V. Zhigilei, "Enhancing and tuning phonon transport at vibrationally mismatched solid-solid interfaces," Physical Review B, vol. 85, no. 3, p. 035438, 2012.

[76] J. P. Feser and D. G. Cahill, "Probing anisotropic heat transport using time-domain thermoreflectance with offset laser spots," Review of Scientific Instruments, vol. 83, no. 10, pp. 104901–104901, 2012.

[77] J. Graebner, "Measurement of thermal diffusivity by optical excitation and infrared detection of a transient thermal grating," Review of scientific instruments, vol. 66, no. 7, pp. 3903–3906, 1995.

[78] O. Käding, H. Skurk, A. Maznev, and E. Matthias, "Transient thermal gratings at surfaces for thermal characterization of bulk materials and thin films," Applied Physics A, vol. 61, no. 3, pp. 253–261, 1995.

[79] A. Vega-Flick, R. A. Duncan, J. K. Eliason, J. Cuffe, J. A. Johnson, J.-P. Peraud, L. Zeng, Z. Lu, A. A. Maznev, E. N. Wang, et al., "Thermal transport in suspended silicon membranes measured by laser-induced transient gratings," AIP Advances, vol. 6, no. 12, p. 121903, 2016.

[80] J. A. Johnson, A. A. Maznev, J. K. Eliason, A. Minnich, K. Collins, G. Chen, J. Cuffe, T. Kehoe, C. M. S. Torres, and K. A. Nelson, "Experimental evidence of non-diffusive thermal transport in si and gaas," in MRS Proceedings, vol. 1347, Cambridge Univ Press, 2011.

[81] G. Chen, "Nonlocal and nonequilibrium heat conduction in the vicinity of nanoparticles," Journal of Heat Transfer, vol. 118, p. 539, 1996.

[82] K. Regner, S. Majumdar, and J. Malen, "Instrumentation of broadband frequency domain thermoreflectance for measuring thermal conductivity accumulation functions," Review of Scientific Instruments, vol. 84, no. 6, p. 064901, 2013.

[83] Y. Hu, L. Zeng, A. Minnich, M. S. Dresselhaus, and G. Chen, "Spectral mapping of thermal conductivity through nanoscale ballistic transport," Nature nanotechnology, vol. 10, no. 8, pp. 701–706, 2015.

[84] L. Zeng, K. C. Collins, Y. Hu, M. N. Luckyanova, A. A. Maznev, S. Huberman, V. Chiloyan, J. Zhou, X. Huang, K. A. Nelson, et al., "Measuring phonon mean free path distributions by probing quasiballistic phonon transport in grating nanostructures," Scientific reports, vol. 5, 2015.

[85] C. A. Paddock and G. L. Eesley, "Transient thermoreflectance from thin metal films," Journal of Applied Physics, vol. 60, no. 1, pp. 285–290, 1986.

[86] D. G. Cahill, K. Goodson, and A. Majumdar, "Thermometry and thermal transport in micro/nanoscale solid-state devices and structures," Journal of Heat Transfer, vol. 124, no. 2, pp. 223–241, 2002.

[87] M. Siemens, "Nanoscale thermal, acoustic, and magnetic dynamics probed with soft x-ray light," 2009.

[88] J. Cuffe, J. K. Eliason, A. A. Maznev, K. C. Collins, J. A. Johnson, A. Shchepetov, M. Prunnila, J. Ahopelto, C. M. S. Torres, G. Chen, et al., "Reconstructing phonon mean-free-path contributions to thermal conductivity using nanoscale membranes," Physical Review B, vol. 91, no. 24, p. 245423, 2015.

[89] K. C. Collins, A. A. Maznev, Z. Tian, K. Esfarjani, K. A. Nelson, and G. Chen, "Non-diffusive relaxation of a transient thermal grating analyzed with the boltzmann transport equation," Journal of Applied Physics, vol. 114, no. 10, p. 104302, 2013.

[90] J. M. Larkin and A. J. McGaughey, "Thermal conductivity accumulation in amorphous silica and amorphous silicon," Physical Review B, vol. 89, no. 14, p. 144303, 2014.

[91] W. Lv and A. Henry, "Examining the validity of the phonon gas model in amorphous materials," Scientific Reports, vol. 6, p. 37675, 2016.

[92] M. Park, I.-H. Lee, and Y.-S. Kim, "Lattice thermal conductivity of crystalline and amorphous silicon with and without isotopic effects from the ballistic to diffusive thermal transport regime," Journal of Applied Physics, vol. 116, no. 4, p. 043514, 2014.

[93] T. Zhan, Y. Xu, M. Goto, Y. Tanaka, R. Kato, M. Sasaki, and Y. Kagawa, "Phonons with long mean free paths in a-si and a-ge," Applied Physics Letters, vol. 104, no. 7, p. 071911, 2014.

[94] M. Siemens, Q. Li, M. Murnane, H. Kapteyn, R. Yang, E. Anderson, and K. Nelson, "High-frequency surface acoustic wave propagation in nanostructures characterized by coherent extreme ultraviolet beams," Applied Physics Letters, vol. 94, p. 093103, 2009.

[95] K. Esfarjani, G. Chen, and H. T. Stokes, "Heat transport in silicon from first-principles calculations," Physical Review B, vol. 84, no. 8, p. 085204, 2011.

[96] G. Wexler, "The size effect and the non-local boltzmann transport equation in orifice and disk geometry," Proceedings of the Physical Society, vol. 89, no. 4, pp. 927–941, 1966.

[97] R. Prasher, "Predicting the thermal resistance of nanosized constrictions," Nano Letters, vol. 5, no. 11, pp. 2155–2159, 2005.

[98] A. J. Minnich, G. Chen, S. Mansoor, and B. Yilbas, "Quasiballistic heat transfer studied using the frequency-dependent boltzmann transport equation," Physical Review B, vol. 84, no. 23, p. 235207, 2011.

[99] E. Swartz and R. Pohl, "Thermal boundary resistance," Reviews of Modern Physics, vol. 61, no. 3, p. 605, 1989.

[100] C. Monachon, L. Weber, and C. Dames, "Thermal boundary conductance: A materials science perspective," Annual Review of Materials Research, vol. 46, pp. 433–463, 2016.

[101] K. Esfarjani and H. T. Stokes, "Method to extract anharmonic force constants from first principles calculations," Physical Review B, vol. 77, no. 14, p. 144112, 2008.

[102] A. Minnich, "Determining phonon mean free paths from observations of quasiballistic thermal transport," Physical Review Letters, vol. 109, no. 20, p. 205901, 2012.

[103] K. Lejaeghere, G. Bihlmayer, T. Björkman, P. Blaha, S. Blügel, V. Blum, D. Caliste, I. E. Castelli, S. J. Clark, A. Dal Corso, et al., "Reproducibility in density functional theory calculations of solids," Science, vol. 351, no. 6280, p. aad3000, 2016.

[104] L. Zeng and G. Chen, "Disparate quasiballistic heat conduction regimes from periodic heat sources on a substrate," Journal of Applied Physics, vol. 116, no. 6, p. 064307, 2014.

[105] A. Minnich, "Multidimensional quasiballistic thermal transport in transient grating spectroscopy," Physical Review B, vol. 92, no. 8, p. 085203, 2015.

[106] H.-y. Ju, P.-k. Kuo, and S.-y. Zhang, "Transient thermal grating analyses of film/substrate structures by eigenfunction expansion method," The European Physical Journal Special Topics, vol. 153, no. 1, pp. 191–194, 2008.

[107] H. J. Eichler, P. Günter, and D. W. Pohl, Laser-induced dynamic gratings, vol. 50. Springer, 2013.

[108] L. Zeng, V. Chiloyan, S. Huberman, A. A. Maznev, J.-P. M. Peraud, N. G. Hadjiconstantinou, K. A. Nelson, and G. Chen, "Monte carlo study of non-diffusive relaxation of a transient thermal grating in thin membranes," Applied Physics Letters, vol. 108, no. 6, p. 063107, 2016.

[109] W. Li, J. Carrete, N. A. Katcho, and N. Mingo, "Shengbte: A solver of the boltzmann transport equation for phonons," Computer Physics Communications, vol. 185, no. 6, pp. 1747–1758, 2014.

[110] J.-P. M. Péraud and N. G. Hadjiconstantinou, "An alternative approach to efficient simulation of micro/nanoscale phonon transport," Applied Physics Letters, vol. 101, no. 15, p. 153114, 2012.

[111] A. Minnich, "Towards a microscopic understanding of phonon heat conduction," arXiv preprint arXiv:1405.0532, 2014.

[112] R. Wilson and D. G. Cahill, "Anisotropic failure of fourier theory in time-domain thermoreflectance experiments," Nature Communications, vol. 5, 2014.

[113] "Understanding nanoscale mechanical properties of materials using ultrafast euv photoacoustics." `http://meetings.aps.org/Meeting/MAR14/Event/217001`. Accessed on May 25th 2017.

[114] B. Vermeersch, A. M. Mohammed, G. Pernot, Y. R. Koh, and A. Shakouri, "Thermal interfacial transport in the presence of ballistic heat modes," Physical Review B, vol. 90, no. 1, p. 014306, 2014.

[115] P. Torres, A. Torelló, J. Bafaluy, J. Camacho, X. Cartoixà, and F. Alvarez, "First principles kinetic-collective thermal conductivity of semiconductors," Physical Review B, vol. 95, no. 16, p. 165407, 2017.

[116] Y. Ma, "Size-dependent thermal conductivity in nanosystems based on non-fourier heat transfer," Applied Physics Letters, vol. 101, p. 211905, 2012.

[117] "Phonon-code." `http://meetings.aps.org/Meeting/MAR14/Event/217001`. Accessed on May 25th 2017.

[118] T. Atanackovic and A. Guran, Theory of Elasticity for scientists and engineers. Birkhauser, 2000.

[119] H. Li, N. Randall, and J. Vlassak, "New methods of analyzing indentation experiments on very thin films," Journal of Materials Research, vol. 25, no. 4, p. 728, 2010.

[120] J. Hay and B. Crawford, "Measuring substrate-independent modulus of thin films," Journal of Materials Research, vol. 26, no. 06, pp. 727–738, 2011.

[121] B. Zhou and B. Prorok, "A new paradigm in thin film indentation," Journal of Materials Research, vol. 25, no. 9, p. 1671, 2010.

[122] J. P. Killgore and D. C. Hurley, "Low-force afm nanomechanics with higher-eigenmode contact resonance spectroscopy," Nanotechnology, vol. 23, no. 5, p. 055702, 2012.

[123] M. Kopycinska-Müller, R. Geiss, J. Müller, and D. Hurley, "Elastic-property measurements of ultrathin films using atomic force acoustic microscopy," Nanotechnology, vol. 16, no. 6, p. 703, 2005.

[124] S. King, G. A. Antonelli, G. Stan, R. F. Cook, and R. Sooryakumar, "Advances in metrology for the determination of young's modulus for low-k dielectric thin films," in SPIE NanoScience+ Engineering, pp. 84660A–84660A, International Society for Optics and Photonics, 2012.

[125] J. Zizka, S. King, A. Every, and R. Sooryakumar, "Mechanical properties of low-and high-k dielectric thin films: A surface brillouin light scattering study," Journal of Applied Physics, vol. 119, no. 14, p. 144102, 2016.

[126] A. Link, R. Sooryakumar, R. Bandhu, and G. Antonelli, "Brillouin light scattering studies of the mechanical properties of ultrathin low-k dielectric films," Journal of Applied Physics, vol. 100, p. 013507, 2006.

[127] C. Thomsen, H. Grahn, H. Maris, and J. Tauc, "Picosecond interferometric technique for study of phonons in the brillouin frequency range," Optics communications, vol. 60, no. 1-2, pp. 55–58, 1986.

[128] H. Grahn, H. Maris, and J. Tauc, "Picosecond ultrasonics," Quantum Electronics, IEEE Journal of, vol. 25, no. 12, pp. 2562–2569, 1989.

[129] O. Matsuda, M. C. Larciprete, R. L. Voti, and O. B. Wright, "Fundamentals of picosecond laser ultrasonics," Ultrasonics, vol. 56, pp. 3–20, 2015.

[130] H. Ogi, M. Fujii, N. Nakamura, T. Shagawa, and M. Hirao, "Resonance acoustic-phonon spectroscopy for studying elasticity of ultrathin films," Applied Physics Letters, vol. 90, no. 19, pp. 191906–191906, 2007.

[131] P. Mante, J. Robillard, and A. Devos, "Complete thin film mechanical characterization using picosecond ultrasonics and nanostructured transducers: experimental demonstration on sio," Applied Physics Letters, vol. 93, p. 071909, 2008.

[132] A. Devos, M. Foret, S. Ayrinhac, P. Emery, and B. Rufflé, "Hypersound damping in vitreous silica measured by picosecond acoustics," Physical Review B, vol. 77, no. 10, p. 100201, 2008.

[133] T. Lee, K. Ohmori, C.-S. Shin, D. G. Cahill, I. Petrov, and J. Greene, "Elastic constants of single-crystal $tin_x(001)(0.67$
$leqx$
leq 1.0) determined as a function of
textitx by picosecond ultrasonic measurements," Physical Review B, vol. 71, no. 14, p. 144106, 2005.

[134] C. Giannetti, B. Revaz, F. Banfi, M. Montagnese, G. Ferrini, F. Cilento, S. Maccalli, P. Vavassori, G. Oliviero, E. Bontempi, et al., "Thermomechanical behavior of surface acoustic waves in ordered arrays of nanodisks studied by near-infrared pump-probe diffraction experiments," Physical Review B, vol. 76, no. 12, p. 125413, 2007.

[135] P. Mante, A. Devos, and J. Robillard, "Towards thin film complete characterization using picosecond ultrasonics," in Ultrasonics Symposium, 2008. IUS 2008. IEEE, pp. 1203–1206, IEEE, 2008.

[136] D. Nardi, F. Banfi, C. Giannetti, B. Revaz, G. Ferrini, and F. Parmigiani, "Pseudosurface acoustic waves in hypersonic surface phononic crystals," Physical Review B, vol. 80, no. 10, p. 104119, 2009.

[137] S. Peli, E. Cavaliere, G. Benetti, M. Gandolfi, M. Chiodi, C. Cancellieri, C. Giannetti, G. Ferrini, L. Gavioli, and F. Banfi, "Mechanical properties of ag nanoparticle thin films synthesized by supersonic cluster beam deposition," The Journal of Physical Chemistry C, vol. 120, no. 8, pp. 4673–4681, 2016.

[138] A. Bartels, R. Cerna, C. Kistner, A. Thoma, F. Hudert, C. Janke, and T. Dekorsy, "Ultrafast time-domain spectroscopy based on high-speed asynchronous optical sampling," Review of Scientific Instruments, vol. 78, no. 3, p. 035107, 2007.

[139] W. Lanford, M. Parenti, B. Nordell, M. Paquette, A. Caruso, M. Mäntymäki, J. Hämäläinen, M. Ritala, K. Klepper, V. Miikkulainen, et al., "Nuclear reaction analysis for h, li, be, b, c, n, o and f with an rbs check," Nuclear Instruments and Methods in Physics Research Section B: Beam Interactions with Materials and Atoms, vol. 371, pp. 211–215, 2016.

[140] S. W. King, J. Bielefeld, G. Xu, W. A. Lanford, Y. Matsuda, R. H. Dauskardt, N. Kim, D. Hondongwa, L. Olasov, B. Daly, et al., "Influence of network bond percolation on the thermal, mechanical, electrical and optical properties of high and low-k a-sic: H thin films," Journal of Non-Crystalline Solids, vol. 379, pp. 67–79, 2013.

[141] Q. Li, K. Hoogeboom-Pot, D. Nardi, M. Murnane, H. Kapteyn, M. Siemens, E. Anderson, O. Hellwig, E. Dobisz, B. Gurney, et al., "Generation and control of ultrashort-wavelength two-dimensional surface acoustic waves at nanoscale interfaces," Physical Review B, vol. 85, p. 195431, 2012.

[142] R. Tobey, M. Siemens, M. Murnane, H. Kapteyn, D. Torchinsky, and K. Nelson, "Transient grating measurement of surface acoustic waves in thin metal films with extreme ultraviolet radiation," Applied Physics Letters, vol. 89, p. 091108, 2006.

[143] D. Nardi, M. Travagliati, M. E. Siemens, Q. Li, M. M. Murnane, H. C. Kapteyn, G. Ferrini, F. Parmigiani, and F. Banfi, "Probing thermomechanics at the nanoscale: Impulsively excited pseudosurface acoustic waves in hypersonic phononic crystals," Nano Letters, vol. 11, no. 10, pp. 4126–4133, 2011.

[144] L. D. Landau, E. M. Lifsic, L. Pitaevskii, and A. Kosevich, Course of Theoretical Physics: Volume 7, Theory of Elasticity. Pergamon Press, 1986.

[145] J. C. Phillips and M. Thorpe, "Constraint theory, vector percolation and glass formation," Solid State Communications, vol. 53, no. 8, pp. 699–702, 1985.

[146] J. C. Mauro, "Topological constraint theory of glass," American Ceramic Society Bulletin, vol. 90, no. 4, p. 31, 2011.

[147] Y. Matsuda, N. Kim, S. W. King, J. Bielefeld, J. F. Stebbins, and R. H. Dauskardt, "Tunable plasticity in amorphous silicon carbide films," ACS applied materials & interfaces, vol. 5, no. 16, pp. 7950–7955, 2013.

[148] J. Cao and F. Li, "Critical poissons ratio between toughness and brittleness," Philosophical Magazine Letters, vol. 96, no. 11, pp. 425–431, 2016.

[149] J. A. Burg and R. H. Dauskardt, "Elastic and thermal expansion asymmetry in dense molecular materials," Nature Materials, vol. 15, no. 9, pp. 974–980, 2016.

[150] S. W. King, L. Ross, H. Li, G. Xu, J. Bielefeld, R. E. Atkins, P. D. Henneghan, K. Davis, D. C. Johnson, and W. A. Lanford, "Influence of hydrogen content and network connectivity on the coefficient of thermal expansion and thermal stability for a-sic: H thin films," Journal of Non-Crystalline Solids, vol. 389, pp. 78–85, 2014.

[151] R. A. Pielke Jr, The honest broker: making sense of science in policy and politics. Cambridge University Press, 2007.

[152] T. S. Kuhn and D. Hawkins, "The structure of scientific revolutions," American Journal of Physics, vol. 31, no. 7, pp. 554–555, 1963.

[153] S. Sismondo, An introduction to science and technology studies. John Wiley & Sons, 2011.

[154] S. Perlmutter, "Supernovae, dark energy, and the accelerating universe," Physics today, vol. 56, no. 4, pp. 53–60, 2003.

[155] W. B. Bonvillian and R. Van Atta, "Arpa-e and darpa: Applying the darpa model to energy innovation," The Journal of Technology Transfer, vol. 36, no. 5, p. 469, 2011.

[156] C. Weiss and W. B. Bonvillian, Structuring an energy technology revolution. MIT Press, 2009.

[157] J. Lane, K. Fealing, J. Marburger III, and S. Shipp, The science of science policy: A handbook. Stanford University Press, 2011.

[158] A. Cho, "Hubs aim to reinvent doe research culture," Science, vol. 340, no. 6135, pp. 914–918, 2013.

[159] "Funding mechanisms." materials proved to SEAB task force.

[160] "American recovery and reinvestment act." `http://www.gpo.gov/fdsys/pkg/BILLS-111hr1enr/pdf/BILLS-111hr1enr.pdf`. Accessed on Apr 27th 2013.

[161] "recovery.gov." `http://www.recovery.gov`. Accessed on Apr 27th 2013.

[162] J. Lane, "Let's make science metrics more scientific," Nature, vol. 464, no. 7288, pp. 488–489, 2010.

[163] J. Lane and S. Bertuzzi, "The star metrics project: Current and future uses for s&e workforce data." `http://www.nsf.gov/sbe/sosp/workforce/lane.pdf`. Accessed on Apr 27th 2013.

[164] J. Lane, "Assessing the impact of science funding," Science, vol. 324, no. 5932, pp. 1273–1275, 2009.

[165] C. of economic advisers, "The economic impact of the american recovery and reinvestment act of 2009, eight quarterly report." `http://www.whitehouse.gov/sites/default/files/cea_8th_arra_report_final_draft.pdf`. Accessed on Apr 27th 2013.

[166] B. Bozeman and D. Sarewitz, "Public values and public failure in us science policy," Science and Public Policy, vol. 32, no. 2, pp. 119–136, 2005.

[167] L. Dilling and M. C. Lemos, "Creating usable science: Opportunities and constraints for climate knowledge use and their implications for science policy," Global environmental change, vol. 21, no. 2, pp. 680–689, 2011.

[168] S. Merrill, S. Olson, et al., Measuring the impacts of federal investments in research: A workshop summary. National Academies Press, 2011.

[169] "Star metrics participate webpage." `https://www.starmetrics.nih.gov/Star/Participate#calculatingjobs`. Accessed on Apr 27th 2013.

[170] M. A. Largent and J. I. Lane, "Star metrics and the science of science policy," Review of Policy Research, vol. 29, no. 3, pp. 431–438, 2012.

[171] D. F. Gardner, M. Tanksalvala, E. R. Shanblatt, X. Zhang, B. R. Galloway, C. L. Porter, R. Karl Jr, C. Bevis, D. E. Adams, H. C. Kapteyn, et al., "Subwavelength coherent imaging of periodic samples using a 13.5 nm tabletop high-harmonic light source," Nature Photonics, 2017.

[172] R. Karl, G. Mancini, D. Gardner, E. Shanblatt, J. Knobloch, T. Frazer, J. N. Hernandez-Charpak, B. Abad Mayor, M. Tanksalvala, C. Porter, C. Bevis, D. Adams, H. Kapteyn, and M. Murnane, "Full-field functional imaging of nanoscale dynamics using tabletop high harmonics," in CLEO, 2017.

[173] M. Maldovan, "Sound and heat revolutions in phononics," Nature, vol. 503, no. 7475, pp. 209–217, 2013.

[174] H. Wang, Y. Xu, S. Ulonska, J. S. Robinson, P. Ranitovic, and R. A. Kaindl, "Bright high-repetition-rate source of narrowband extreme-ultraviolet harmonics beyond 22 [thinsp] ev," Nature communications, vol. 6, 2015.